

International Atomic Energy Agency

INDC(NDS)-214/LJ

INDC

INTERNATIONAL NUCLEAR DATA COMMITTEE

STATUS REVIEW OF METHODS
FOR THE CALCULATION OF FAST NEUTRON NUCLEAR DATA
FOR STRUCTURAL MATERIALS OF FAST AND FUSION REACTORS

Texts of invited papers presented during the Second Research
Co-ordination Meeting, Vienna, 15-17 February 1988

Compiled by V. Goulo

January 1989

IAEA NUCLEAR DATA SECTION, WAGRAMERSTRASSE 5, A-1400 VIENNA

STATUS REVIEW OF METHODS
FOR THE CALCULATION OF FAST NEUTRON NUCLEAR DATA
FOR STRUCTURAL MATERIALS OF FAST AND FUSION REACTORS

Texts of invited papers presented during the Second Research
Co-ordination Meeting, Vienna, 15-17 February 1988

Compiled by V. Goulo

January 1989

Reproduced by the IAEA in Austria
January 1989

89-00224

Foreword

This report contains the text of invited papers delivered during the second Research Co-ordination Meeting on "Methods for the Calculations of Fast Neutron Nuclear Data for Structural Materials of Fast and Fusion Reactors". The meeting was held in Vienna during 15-17 February 1988.

Since the meeting there have been many requests from participants of the International Workshop on Applied Nuclear Physics and Nuclear Model Calculations to make available the texts of papers done under the IAEA CRP on "Methods for Neutron Nuclear Data Evaluation" in printed form as INDC(NDS) report. The texts are reproduced directly from the author's manuscripts without any editing.

Contents

Some Fundamental Aspects of the Optical Potential for the Interaction of Fast Neutrons with Cobalt By A.B. Smith, R.D. Lawson	7
Optical Model Calculations for Experimental Interpretation and Evaluation: Practical Considerations and Fundamental Implications By A.B. Smith, P.T. Guenter, R.D. Lawson	25
The Neutron Optical Model Potential By P.E. Hodgson	49
Consistent Systematics of Nuclear Level Densities for Mean and Heavy Nuclei By O.T. Grudzevich, A.V. Ignatjuk, V.I. Plyaskin	69
Effect of Realistic Partial State Densities on Pre-equilibrium Decay By M. Blann, G. Reffo	75
The MSC Calculations with use of EMPIRE By A. Marcinkowski	79
On The Two Gas Approach for Exciton Model Master Equation By G. Reffo, M. Herman, C. Costa	91
Analysis of Particles Emitted in them on Iron-Group Nuclei By V.M. Bychkov, O.T. Grudzevich, A.V. Zelenetsky, A.B. Pashchenko, V.J. Plyaskin	99
Investigation of the Angular Distribution of Secondary Energy Dependant Inelastic Neutron Cross Sections in Structural Materials Using Blann's Geometry Dependant Hybrid Model By E. Bahm, H. Jahn	111

SOME FUNDAMENTAL ASPECTS OF THE OPTICAL POTENTIAL
FOR THE INTERACTION OF FAST NEUTRONS WITH COBALT^{a,b}

A. B. Smith and R. D. Lawson
Argonne National Laboratory
Argonne, Illinois, USA

ABSTRACT

Differential elastic- and inelastic-scattering cross sections, measured from ≈ 1.5 to 10.0 MeV, are interpreted in terms of spherical-optical-statistical (OM) and coupled-channels models. A successful description of the differential elastic scattering below 10 MeV and the total cross section to 20.0 MeV is achieved using the spherical OM with energy-dependent strengths and geometries. These energy dependencies are large below ≈ 7.0 MeV, but become smaller and similar to those reported for "global" potentials at higher energies. This change in the energy dependence of the parameters probably marks the onset of the Fermi surface anomaly ≈ 19 MeV above the Fermi energy. Inelastic scattering to the levels below 1.8 MeV displays a forward peaked behavior. This non-statistical component is interpreted using the weak coupling model in which the $f_{7/2}$ proton hole is coupled to the 2^+ state in ^{60}Ni . This model provides an explanation of the unusual energy dependence and relatively small radius found for the imaginary OM potential. The coupling also contributes to the large value of this potential. The real spherical OM potential derived from the neutron-scattering results is extrapolated to bound energies using the dispersion relationship and the method of moments. The resulting real-potential strength and radius peak at ≈ -10.0 MeV, whereas the real diffuseness is at a minimum at this energy. The extrapolated potential is $\approx 8\%$ larger than that implied by reported particle-state energies, and $\approx 13\%$ smaller than indicated by hole-state energies.

I. INTRODUCTION

For many years the interaction of few-MeV neutrons with nuclei of mass $A = 50$ to 60 has been somewhat of an enigma. Spherical-optical (OM) and/or coupled-channels models, deduced from higher-energy neutron and charged-particle observations, often do not reasonably extrapolate to lower energies (2,3). Moreover, reasonable descriptions of the neutron total and scattering cross sections over the first few MeV frequently imply sharp energy dependencies of the potential that are inconsistent with those based upon higher-energy observations (4,5). OM potentials based upon low-energy neutron phenomena tend to be characterized by a small real-potential depth and large real radius, relative to those appropriate for higher-energy, and often the real radius exceeds that of the imaginary interaction by significant amounts (6,7).

Some of the above shortcomings have been attributed to fluctuations. In the few-MeV region compound-elastic scattering is generally large (8) and its reliable calculation requires knowledge of excited states; discrete states at

a. This work supported by the U. S. Department of Energy, Basic Energy Science, under Contract W-31-109-Eng-38.

b. A detailed description of this work is given in ref. 1.

low energies and then statistical level properties at higher energies. The discrete-level properties are not always well known. The statistical properties are particularly uncertain at low energies, and they may fluctuate about the average by considerable amounts. Fluctuations no less trouble experimental observations. Measured energy-averaged low-energy neutron total cross sections are often distorted toward too low values due to self-shielding effects (9). Fluctuations are also an obstacle in the measurement of neutron energy-averaged partial cross sections. The latter must be made in energy detail and then averaged over energy intervals large compared to those of the fluctuations. The energy interval required to obtain a reasonable average very often includes the opening of several prominent exit channels that qualitatively change the character of the interpretation within the averaging interval.

Nuclei in the $A = 50$ to 60 region display some collective properties. The energies, spins and parities of the first few levels are often characteristic of those predicted for vibrational nuclei, though the quadrupole moments are not zero and there are, in some cases, additional levels that are not consistent with such a concept. Failure to properly consider collective effects may be the source of some of the discrepancies between observation and calculation, noted above. It is known from low-energy neutron scattering studies that the imaginary-potential strength is mass dependent (10), and low-energy (p,n) studies suggest that the imaginary strengths are particularly large in the $A \approx 60$ region (11).

In recent publications, Mahaux and Sartor (12,13,14) have used the dispersion relationship (15), relating the real and imaginary OM potentials, together with the moments of these interactions, to predict the energy dependence of the real potential in the bound-state regime. Applied to the $A \approx 89$ and 208 regions, these concepts indicate a maximum of the real-potential strength at bound energies and also a strong energy dependence of the geometric parameters at low-positive and bound energies. In the neighborhood of the Fermi energy the resulting potential is considerably different from that obtained by extrapolating conventional "global" potentials (16), or from the general energy dependence resulting from a Hartree-Fock calculation. This behavior is known as the Fermi Surface Anomaly (17). This is consistent with the dichotomy between the energy dependencies of potentials based upon low- and high-energy neutron data (3,4,18,19). In addition, the energy dependence of the potential brings about qualitative agreement with the potential strengths implied by the observed energies of particle- and hole-states.

The present study was undertaken to cast light on the above issues. Cobalt is an odd- A nucleus with a reasonably-high level density at low energies, thus mitigating some of the problems due to fluctuations. The properties of some of the low-lying levels are well known making possible quantitative compound-nucleus calculations. There is experimental information dealing with bound particle- and hole-states allowing a test of the extrapolation of the real OM potential to negative energies. The magnitude of the Fermi energy is large ($E_f \approx -12.3$ MeV), therefore providing a quite different situation from that encountered in the previous studies of potential anomalies in the $A \approx 208$ region ($E_f \approx -6$ MeV). The region of most interest in the context of the above issues is below 10.0 MeV, and uniquely accessible to the neutron probe. This study makes extensive use of comprehensive new experimental results reported elsewhere (1).

II. MODEL DERIVATION

The interpretation was primarily based on the conventional spherical OM (20), explicitly fitting the model parameters to the differential elastic-scattering cross sections. It was assumed that the OM potential consisted of a real Woods-Saxon form, a Woods-Saxon-derivative imaginary part, and a real Thomas spin-orbit term. A possible contribution due to volume absorption was investigated at the higher energies of the present study with no identifiable contribution. All of the spherical calculations were carried out with the most recent formulation of the computer code ABAREX (21).

The OM fitting employed χ^2 minimization procedures, minimizing the quantity,

$$\chi^2 = \frac{1}{N} \sum_{i=1}^N \left[\frac{\sigma_{\text{exp}}(\theta_i) - \sigma_{\text{cal}}(\theta_i)}{\delta\sigma_{\text{exp}}(\theta_i)} \right]^2, \quad (1)$$

where $\sigma_{\text{exp}}(\theta_i)$ is the measured value at angle θ_i , $\delta\sigma_{\text{exp}}(\theta_i)$ its uncertainty, $\sigma_{\text{cal}}(\theta_i)$ the corresponding calculated value, and N is the number of data points contained in a given distribution. Up to an energy of ≈ 8.0 MeV compound-nucleus processes make a significant contribution to the elastic scattering. They were calculated using the Hauser-Feshbach formula (22), with the fluctuation and correlation corrections prescribed by Moldauer (23). The compound-nucleus calculations included discrete levels up to an excitation energy of 2.6 MeV, using the energies, spins, and parities cited in ref. 24. A statistical-level formulation given by

$$\rho(E, J) = \frac{(2J + 1)}{2\sigma^2 T} \exp((E - E_0)/T) \exp(-(J + 1/2)^2/2\sigma^2), \quad (2)$$

where J is the angular momentum of the continuum target level and E_0 , T and σ are parameters, was used to describe higher-energy excitations. Initially the parameters E_0 , T , and σ were taken from the work of Gilbert and Cameron (25).

However, with their values the inelastic cross sections corresponding to excitations of ≤ 1.8 MeV, shown in fig. 1, were underestimated by $\approx 15\%$ in the 3.0 to 4.0 MeV incident-energy range, and concurrently the minima of the differential elastic-scattering distributions were systematically smaller than observed. A better agreement between observation and calculation was obtained by increasing T by 40 keV, resulting in the statistical parameters for the subsequent calculations of $E_0 = -0.4$ MeV, $T = 1.10$ MeV, and $\sigma = 3.0$. Above

≈ 8.4 MeV there was no evidence for a compound-nucleus contribution, so the calculations considered only shape-elastic scattering. Fluctuations are evident in the neutron total and differential-elastic-scattering cross sections to more than 4.0 MeV (1), even with the relatively broad incident-energy averages. Therefore, primary emphasis was given to the energy range 4.5 to 10.0 MeV. The lower-energy data were concurrently fitted in three energy intervals having widths of ≈ 1.0 MeV. Even so, the parameters resulting from the lower-energy fitting fluctuated by considerable amounts and thus were not used in determining the general behavior of the parameters. Near zero energy the $\ell = 0$ strength function is known from resonance measurements (26). This value provides a low-energy reference point in the fitting. The energy-averaged neutron total cross section is reasonably known to at least 20.0 MeV (1,27). Considerations of the total cross section further guided the fitting beyond the primary 4.5 to 10.0 MeV range.

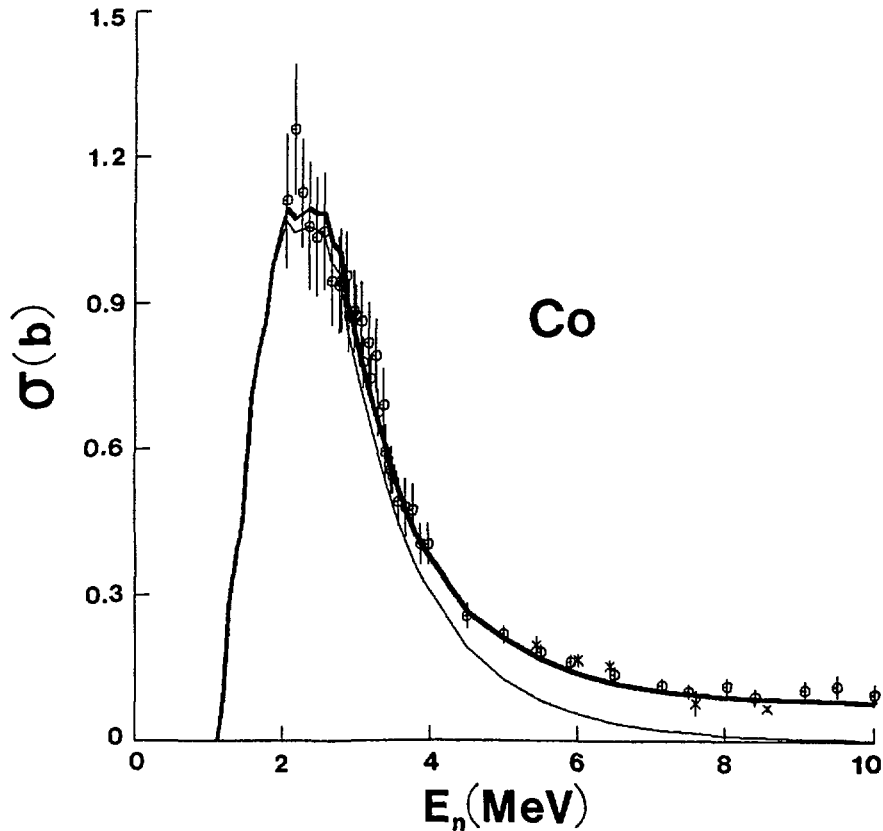


Fig. 1. Angle-integrated cross sections for the excitation of levels in the range $E_x = 1.0$ to 1.8 MeV. Symbols denote experimental results as defined in ref. 1. Results of statistical-model calculations are indicated by the light curve and those including the vibrational contribution, by the heavy curve.

The present elastic-scattering data were most sensitive to the spin-orbit potential at the higher energies. Therefore, the 9.0 to 10.0 MeV data were used to determine the spin-orbit potential. The resulting spin-orbit parameters, determined as described in ref. 1, were; V_{so} (strength) = 5.5 MeV, r_{so} (radius) = 1.005 fm, and a_{so} (diffuseness) = 0.65 fm. These values were not used to calculate polarization data since no suitable experimental information was found (28). However, the parameters of eq. (4) are reasonably consistent with those cited in global OM's (16,29).

With the above spin-orbit potential, the fitting started by varying the six parameters, real and imaginary strengths, radii and diffusenesses. The results indicated a relatively constant real diffuseness, a_v , and it was fixed to the average value. The fitting procedure was then repeated varying the remaining five parameters. Of these, the imaginary diffuseness, a_w , was the most stable and was fixed for the subsequent four parameter fitting. It was evident that a_w was energy dependent, increasing from rather small values at low energies to ≈ 7.0 MeV, and then remaining approximately constant at higher energies. The four-parameter fits resulted in reasonable definition of the real radius, r_v . As for a_w , there appeared to be a change in the energy dependence at ≈ 7.0 MeV, with a large negative slope below that energy and a small slope at higher energies. The three remaining parameters were then fitted with results indicating that the imaginary radius, r_w , was $\approx 0.96 r_v$.

The resulting geometric parameters are summarized by,

$$\begin{aligned}
 r_v &= 1.39 - 0.0168 E \quad (E \leq 7.5 \text{ MeV}) \quad \text{fm} \\
 &= 1.288 - 0.0032 E \quad (E \geq 7.5 \text{ MeV}) \quad \text{fm}, \\
 a_v &= 0.6355 \text{ fm}, \\
 r_w &= 0.96 r_v \quad \text{fm}, \\
 a_w &= 0.19 + 0.0386 E \quad (E \leq 7.5 \text{ MeV}) \quad \text{fm} \\
 &= 0.480 \quad (E \geq 7.5 \text{ MeV}) \quad \text{fm},
 \end{aligned} \tag{3}$$

where E is the energy in MeV.

With the above potential geometry, two parameter fits were made, varying the real, V_0 , and imaginary, W_0 , well depths. The results were expressed as volume-integrals-per-nucleon given by

$$J_v = \frac{4\pi}{A} \int_0^\infty V(r) r^2 dr$$

and

$$J_w = \frac{4\pi}{A} \int_0^\infty W(r) r^2 dr.$$

They are shown, together with the associated χ^2/point resulting from the individual fits, in fig. 2. Both J_v and J_w are nonlinear functions of energy, showing different slopes below and above ≈ 7.0 MeV. Combining these results with the requirement that the s-wave strength function, S_0 , be well represented and the neutron total cross section be predicted to at least 20.0 MeV, one concludes that J_v and J_w can be reasonably described by two linear segments given by

$$\begin{aligned}
 J_v &= 550.0 - 12.5 E \quad \text{MeV-fm}^3 \quad (E \leq 7.5) \\
 &= 474.0 - 2.4 E \quad \text{MeV-fm}^3 \quad (E \geq 7.5)
 \end{aligned}$$

and

$$\begin{aligned}
 J_w &= 135.0 - 6.4 E \quad \text{MeV-fm}^3 \quad (E \leq 7.5) \\
 &= 104.0 - 2.3 E \quad \text{MeV-fm}^3 \quad (E \geq 7.5).
 \end{aligned} \tag{5}$$

The higher-energy behavior is similar to that frequently reported in "global" analyses (16). The uncertainty estimates of fig. 2 are reasonably born out by the reproducibility of results obtained at different times.

Eqs. (3), (4), and (5) result in $S_0 = 3.97 \times 10^{-4}$ compared to the value $(3.9 \pm 0.5) \times 10^{-4}$ deduced from resonance data (26). The same equations give a good description of the neutron total cross sections from several-hundred keV to 20 MeV, as illustrated in fig. 3, where energy averages of the entire experimental data base (28) are compared with the calculated results. In particular, the calculations reasonably represent the observed total-cross-section minimum in the 1.0 to 3.0 MeV region, a result which is not obtained when the conventional "global" models primarily based upon high-energy observations are used (3). This is a reflection of the energy

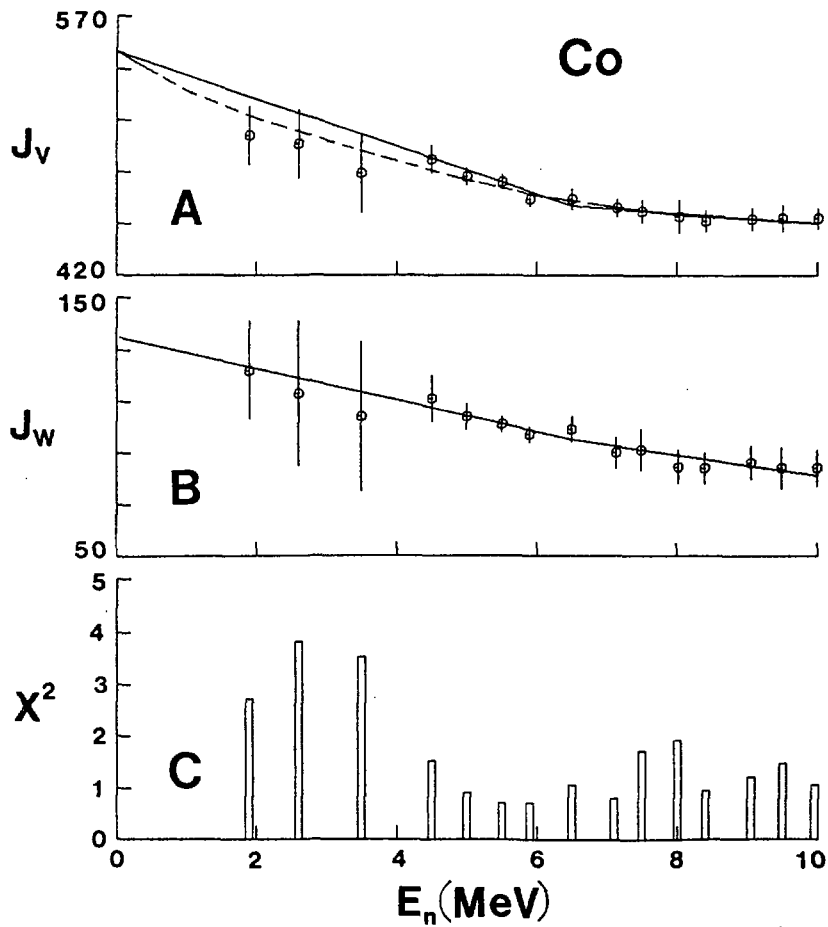


Fig. 2. Sections (A) and (B) show, respectively, the real and imaginary potential strengths, J_v and J_w , in MeV fm^3 , as a function of energy, E_n in MeV. Symbols indicated the results of fitting the experimental data and curves eq. (5) of the text. Section (C) gives χ^2/point as defined by eq. (1).

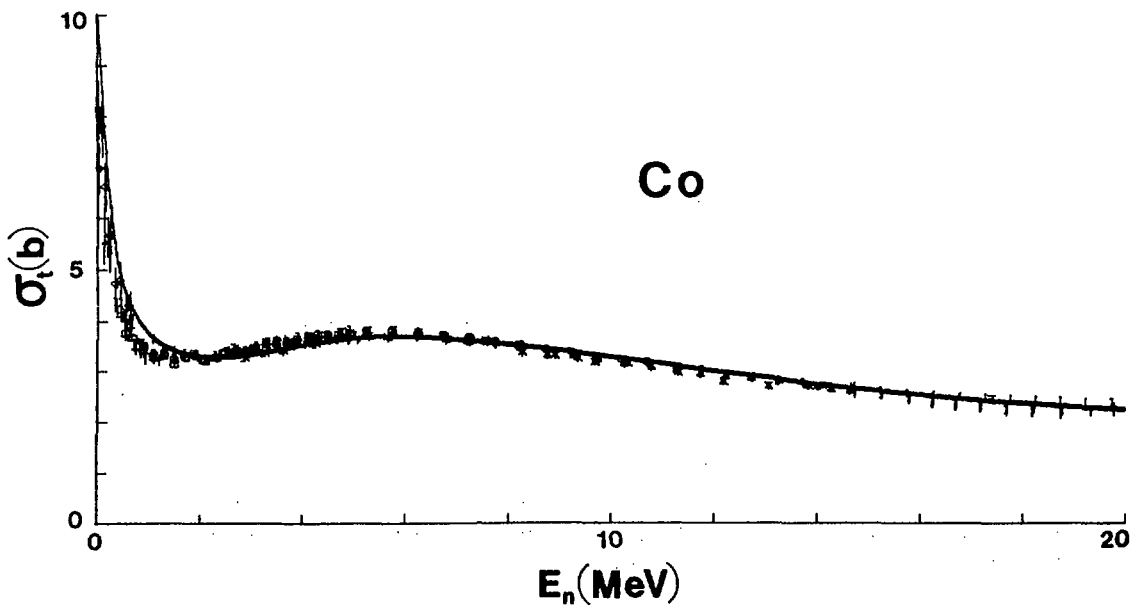


Fig. 3. Comparison of calculated (heavy curve) total cross sections and broad energy-averages of available experimental data (symbols).

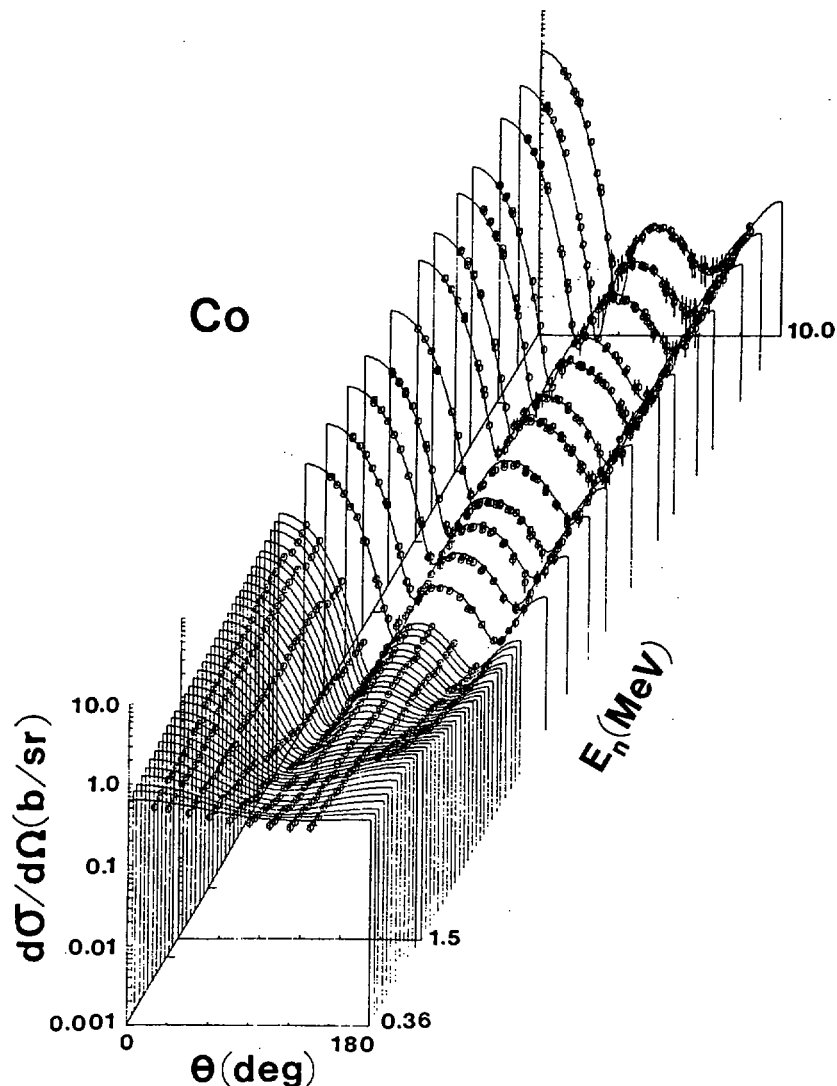


Fig. 4. Differential elastic-scattering cross sections of Cobalt. "o" indicate the experimental results of ref.1, curves the results of the OM calculations described in the text.

dependence of the potential used in the present calculations. A very good description of the observed neutron differential elastic-scattering cross sections was obtained from less than 1.0 to 10 MeV, as illustrated in fig. 4.

Using eqs. (3), (4) and (5), the Hauser-Feshbach-Moldauer model (22,23) leads to the calculated inelastic excitation functions indicated by the curves of fig. 5. Up to ≈ 4.0 MeV the calculations are in reasonable agreement with the measured values. However, there is a systematic tendency for the cross sections to the levels below ≈ 1.8 MeV to be under predicted, and increasingly so with energy.

As the energy increases it becomes clear that the simple compound-nucleus concept is deficient. In particular, neutrons resulting from the complex of levels below 1.8 MeV are no longer emitted symmetrically about 90° (see fig. 6), but rather the distributions are strongly peaked toward forward angles. The statistical calculations predict very small cross sections for the excitation of this complex of levels above ≈ 5.0 MeV incident energy, and the calculated results are an order of magnitude smaller than the observations at 8.0 to 10.0 MeV (see fig. 1). This behavior suggests a significant

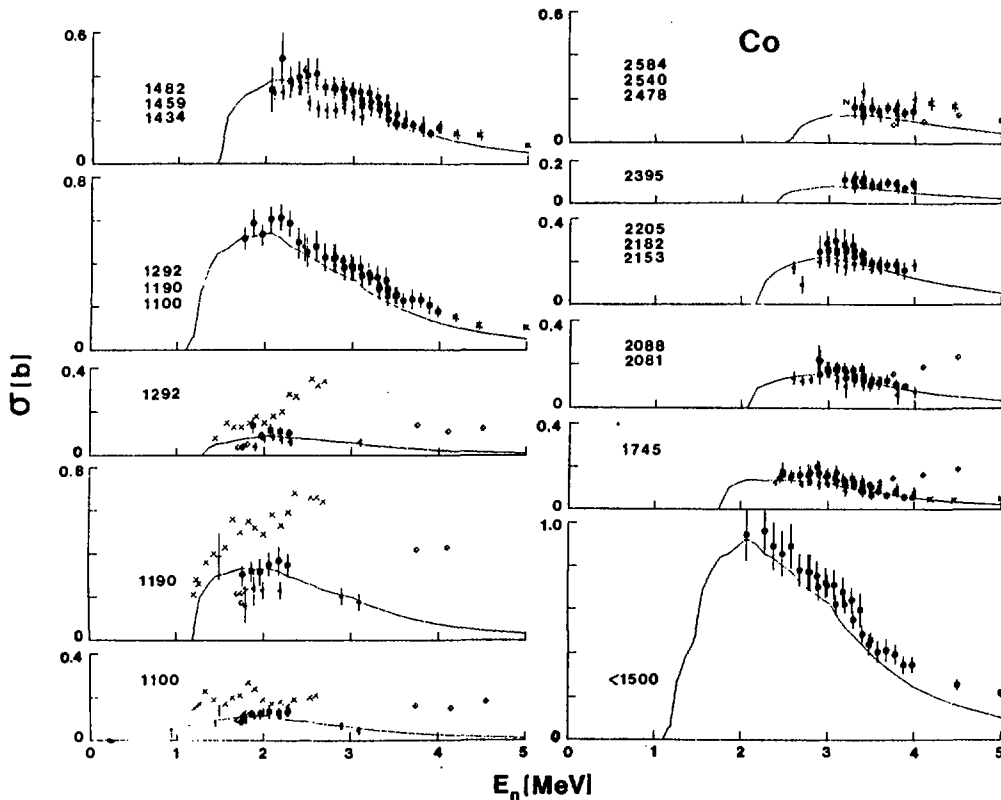


Fig. 5. Angle-integrated inelastic neutron-excitation cross sections of Cobalt. Experimental results are indicated by data symbols as defined in ref. 1. Curves indicate the results of statistical-model calculations as described in the text. Excitation energies are given in keV (24) in each section of the figure.

direct-reaction contribution, which can be estimated as follows: Below 2.0 MeV ^{59}Co has seven negative parity states, with spins $1/2$, $(3/2)^2$, $5/2$, $7/2$, $9/2$ and $11/2$. The weak-coupling model, in which an $f_{7/2}$ proton hole is coupled to the first excited 2^+ state in ^{60}Ni , accounts for five of these levels. The remaining two are attributed to the excitation of an $f_{7/2}$ proton to either the $p_{1/2}$ or $p_{3/2}$ single-particle state (24). Since the yrast 2^+ state in ^{60}Ni is collective, one would expect the majority of the direct-reaction strength in the low-lying ^{59}Co levels to come from the excitation of this state. To estimate this cross section it was assumed that ^{60}Ni is a vibrational nucleus, and a coupled-channels calculation (30) was carried out in which the one-phonon state (2^+ , 1.333 MeV) and the two-phonon states (2^+ , 0^+ and 4^+) were considered (31). Except for the radius of the imaginary interaction, which was assumed to be 6% larger than given in eq. (3), the strength and geometry of the deformed potentials were taken to be those of eqs. (3) and (5). The reason for the change in r_w will be discussed later. The spin-orbit interaction was taken to be spherical, whereas the quadrupole deformation of both the real and imaginary interactions was assumed to be described by $\beta_2 = 0.25$. The direct-reaction cross section to the 1.333 MeV state, which would be divided among the weak-coupling $3/2^-$, $5/2^-$, $7/2^-$, $9/2^-$ and $11/2^-$ levels of ^{59}Co , was calculated on the basis of this model.

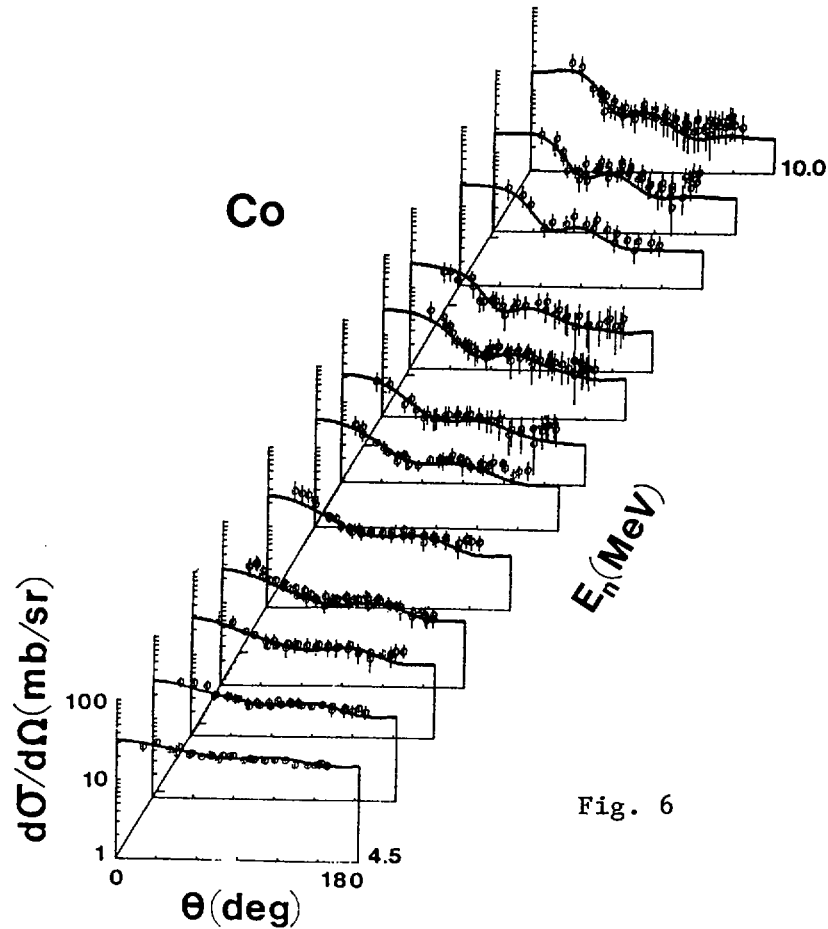


Fig. 6

Fig. 6. Differential cross sections for the excitation of the composite of levels in the range $E_x = 1.0$ to 1.8 MeV. "o" indicate experimental values from ref. 1, and curves the results of calculations as described in the text.

This was then added to the statistical contribution, derived assuming that ^{59}Co is a spherical nucleus, to obtain an estimate of the total inelastic-scattering cross section. The predicted angular distributions of scattered neutrons due to the excitation of the complex of levels below 1.8 MeV, derived in the above manner, agreed fairly well with the experimental values, as illustrated in fig. 6. Furthermore, the predicted total inelastic-scattering cross section for the same complex of levels agrees well with measured values, as shown in fig. 1.

III. DISCUSSION

The model geometries, eq. (3), resulting from the foregoing interpretation are not conventional. The real radius decreases sharply with increasing energy in the low-MeV region. Its magnitude at these energies is relatively large, similar to that often associated with potentials based upon low-energy phenomena such as the strength function (6). At higher energies the real radius approaches that commonly encountered in "global" models (16), and the E -dependence becomes small. The transition between a large and small energy dependence occurs at ≈ 7.0 MeV. The real-potential diffuseness is constant with energy and has a value similar to that reported in "global" models. In this mass region it is frequently found that the imaginary radius is smaller than the real radius (2,32). Below 10.0 MeV the present analysis

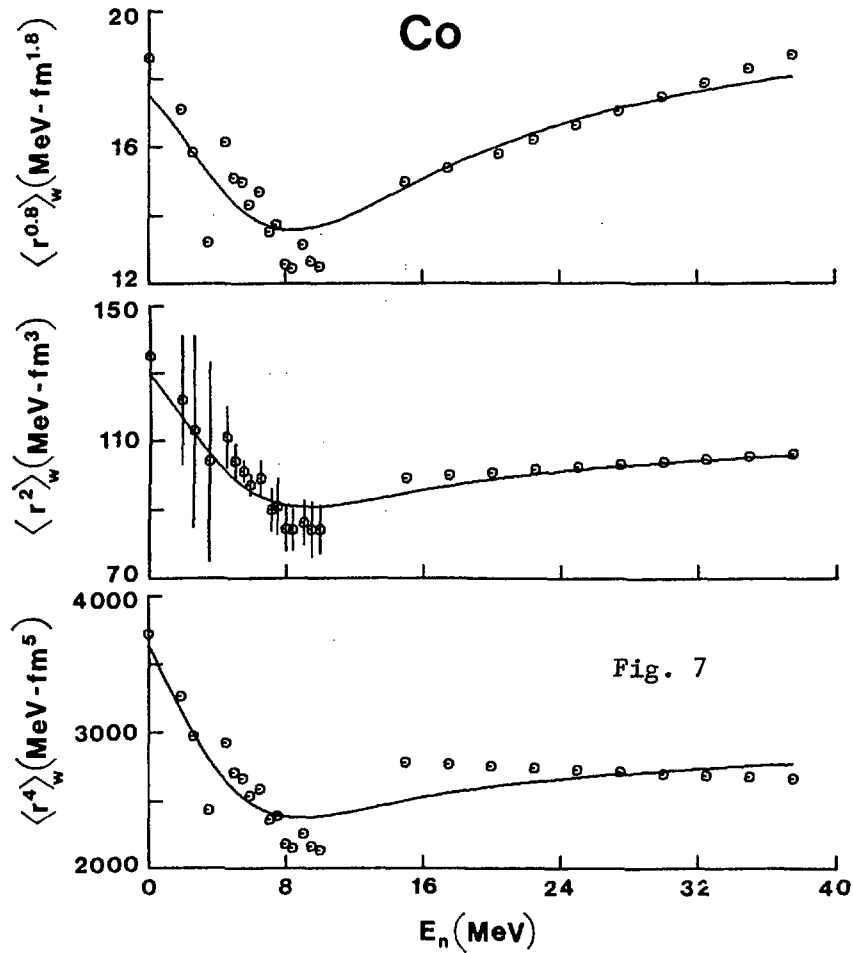


Fig. 7. Moments of the imaginary OM potential, $\langle r(E)^q \rangle_w$ (eq. (10) of the text), for $q = 0.8, 2$ and 4 . For $E < 10.0$ MeV "o" indicate values deduced from experiments of ref. 1. In the range $15.0 < E < 37.5$ MeV the "o" values were deduced from the potential of ref. 29. For $q = 2$, J_w and the uncertainty estimates for $E < 10.0$ MeV were taken from the experiments illustrated in fig. 2. Solid curves are "best fit" parameterizations of the moments obtained using eq. (14).

is consistent with this observation as r_w is $\approx 4\%$ smaller than r_v over the entire energy range of the present scattering measurements. At very low energies, the absorptive potential approaches the δ -function form. a_w rises rapidly with increasing energy, and at ≈ 7.0 MeV reaches a value similar to that reported from "global" analyses. Above ≈ 7.0 MeV, a_w can be taken independent of energy. Generally, it was found that the OM potential geometries for cobalt are only weakly dependent on energy above ≈ 7.0 MeV (i.e., ≈ 19.0 MeV above E_f , the Fermi energy), while for lower energies the energy variation of r_v , r_w and a_w is quite rapid. A similar result was found in bismuth (19), where the transition between rapid and weak energy variation occurred in the $8.0 - 10.0$ MeV region (i.e., ≈ 16.0 MeV above E_f).

For the closed-neutron-shell nuclei ^{89}Y and ^{209}Bi , the volume-integral-per-nucleon of the imaginary potential has the value 66.47 and 33.87 $\text{MeV}\cdot\text{fm}^3$, respectively, at $E = 0$ (18,19). This is to be contrasted with

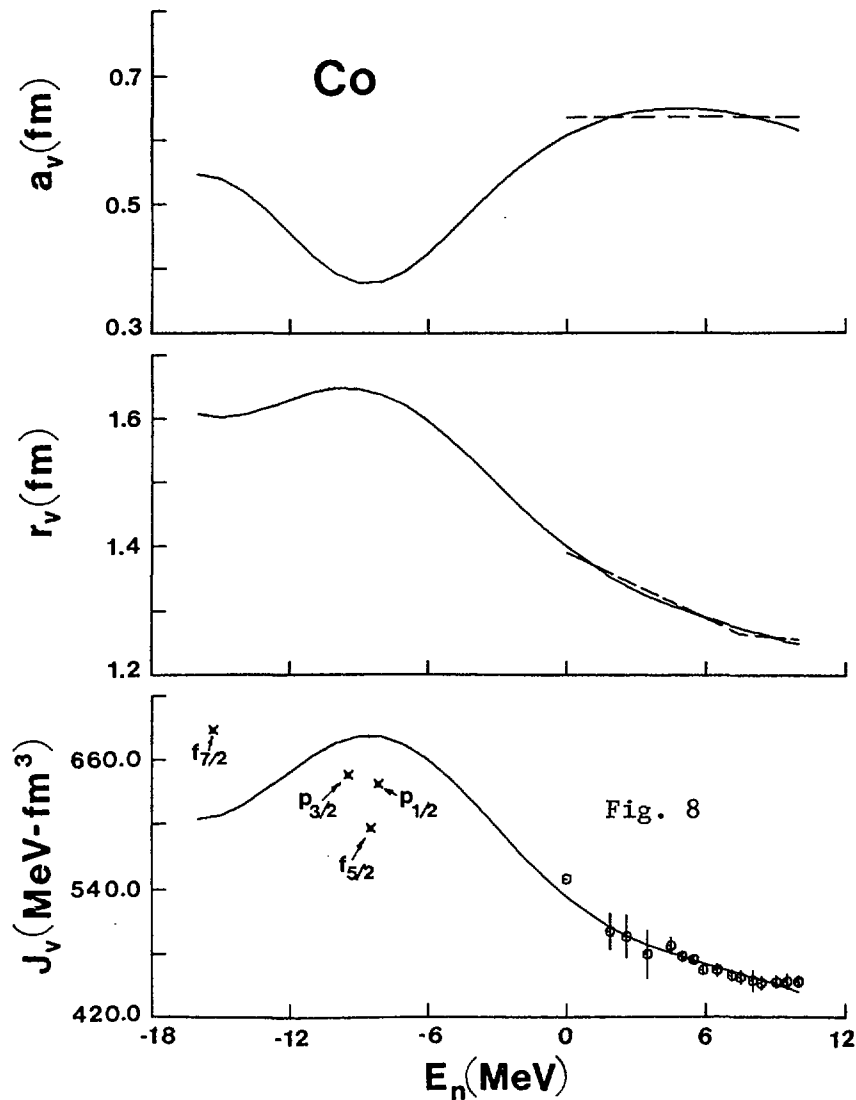


Fig. 8. Solid curves show a_v , r_v , and J_v , as a function of energy, deduced from the Woods-Saxon potential when eq. (15) is used to determine the moments of the real potential. The dashed lines correspond to the experimentally derived values of a_v and r_v for $E > 0$. The J_v values at positive energies correspond to those of fig. 2. For $E < 0$ the data symbols indicate the J_v values implied by the binding energies of particle- and hole-states when r_v and a_v have the values predicted by eq. (15) at the respective energies.

the large value given in eq. (5). Thus, as has been noted before (33), the value of J_w increases markedly as one moves away from closed shells. An additional factor contributing to the large J_w value for ^{59}Co is probably due to collective effects, as discussed below. The energy dependence of J_w , given in eq. (5), is surprising. As the incident-neutron bombarding energy increases, more channels open up and one would expect J_w to increase with increasing E at relatively low energies (34,35). Just the opposite energy trend results from the present interpretation, and has been reported elsewhere for this mass region; for example, by Wilmore and Hodgson (36). This energy dependence of J_w may be attributed to the possible vibrational character of nuclei in this mass region as follows.

It is well known that the nickel isotopes can be described by the spherical shell model (37), provided one introduces a rather large effective neutron charge to explain the observed B(E2) values. Alternatively, one can interpret the spectra of these nuclei using the anharmonic vibrational model (38). Consequently, the properties of the spherical OM were examined to assess the effects of its use in describing neutron scattering from a vibrational nucleus. For this purpose, pseudo data for neutron shape-elastic scattering were generated for ^{60}Ni using a vibrational model in which the 0^+ ground state, the 2^+ one-phonon level at 1.333 MeV, and the two-phonon triplet (31), were coupled. A potential consisting of Woods-Saxon real, derivative Woods-Saxon imaginary and Thomas spin-orbit was assumed. Pseudo data were then generated using the coupled-channels computer code ANLECIS (30), with the potential parameters

$$\begin{aligned}
 V_0(\text{real}) &= (47.0 - 0.3 E) \quad \text{MeV} \\
 r_v &= 1.28 \quad \text{fm} \\
 a_v &= 0.64 \quad \text{fm} \\
 \\
 W_0(\text{imaginary}) &= (9.7 + 0.2 E) \quad \text{MeV} \\
 r_w &= 1.25 \quad \text{fm} \\
 a_w &= 0.40 \quad \text{fm} \\
 \\
 V_{\text{so}}(\text{spin-orbit}) &= 6.0 \quad \text{MeV} \\
 r_{\text{so}} &= 1.28 \quad \text{fm} \\
 a_{\text{so}} &= 0.64 \quad \text{fm},
 \end{aligned} \tag{6}$$

and $\beta_2 = 0.25$. These elastic-scattering pseudo data were calculated at twelve incident energies between 4.5 and 10.0 MeV. The resulting cross sections were truncated to the experimentally accessible angular range. A constant error was assigned to these pseudo data, and the calculated total cross sections added, with a weight of six differential cross-section values, to form a pseudo-experimental data base for fitting with the spherical OM code (21) in a manner analogous to that employed in the above experimental interpretation. The following results were obtained (39): Although the diffusenesses had a slight energy dependence, their values were quite similar to those of eq. (6). Furthermore, the resulting real-potential radius was only 1.25% smaller than that originally assumed, and the real potential strength was only 3.7% smaller at 4.5 MeV and 4.6% smaller at 10.0 MeV. On the other hand, the imaginary-potential radius resulting from the fitting was significantly smaller, by 6.3%, than the original value of eq. (6). Moreover, the character of the imaginary strength changed completely. From eq. (6) it follows that the strength increases with increasing energy as

$$J_w = (79.94 + 1.65 E) \quad \text{MeV} \cdot \text{fm}^3, \tag{7-a}$$

whereas a best fit to the pseudo data gives a J_w that decreases with energy as

$$J_w = (121.08 - 1.41 E) \quad \text{MeV} \cdot \text{fm}^3. \tag{7-b}$$

Moreover, the zero-energy magnitude of J_w , obtained from the fit, is $\approx 50\%$ larger than the original value. Somewhat similar results have been reported

by Perey in his studies of charged-particle scattering (40). Thus, when a spherical model is used, in this mass region, to interpret pseudo data from a vibrational nucleus there are major changes in the imaginary potential. In particular: the imaginary radius is significantly smaller, and the imaginary strength at $E = 0$ obtained from fitting the pseudo data is $\approx 50\%$ stronger. Furthermore, the strength decreases with increasing energy.

Using only the 4.5 to 10.0 MeV data, a satisfactory fit to the values needed to describe the experiment is given by

$$J_v = (505.93 - 5.98 E) \text{ MeV} \cdot \text{fm}^3. \quad (8)$$

When eq. (8) for J_v is used, in conjunction with the geometric parameters of eq. (3), the predicted neutron total cross section in the 1.0 to 2.0 MeV region and S_0 are not in very good agreement with those derived from experiments. Moreover, the rapid decrease in J_v with energy leads to unsatisfactory values of the predicted total cross section at energies $> \approx 12.0$ MeV. In order to remedy both of these deficiencies, the parametrization of J_v given by eq. (5) was chosen. Thus, when data outside the 4.5 to 10.0 MeV range are included in the considerations, one is led to the conclusion that J_v exhibits a rapid decrease with increasing energy below ≈ 7.0 MeV. Above that energy the slope is smaller and is quite close to "global" values of $J_v/dE = -2.712 \text{ fm}^3$ (16) and $dJ_v/dE = -2.776 \text{ fm}^3$ (29). A similar result-- a large negative slope at low energies changing to a smaller value at ≈ 10.0 MeV-- has recently been found in an analysis of neutron scattering from ^{209}Bi (19).

In a series of recent papers, Mahaux and Sartor (12-14) have outlined a procedure for extrapolating the OM potential to the bound-state regime. There is a well known dispersion relationship linking the real and imaginary potentials (15)

$$V(r, E) = V_{\text{hf}}(r, E) + \frac{P}{\pi} \int_{-\infty}^{+\infty} \frac{W(r, E')}{E - E'} dE', \quad (9-a)$$

where P is the principal-value integral and $V_{\text{hf}}(r, E)$ is the Hartree-Fock component of the potential. This same dispersion relationship holds for the radial moments of the potential, that is

$$\langle r(E)^q \rangle_v = \langle r(E)^q \rangle_{\text{hf}} + \frac{P}{\pi} \int_{-\infty}^{+\infty} \frac{\langle r(E')^q \rangle_w}{E - E'} dE', \quad (9-b)$$

where, for example,

$$\langle r(E)^q \rangle_w = \frac{4\pi}{A} \int_0^{\infty} W(r, E) r^q dr. \quad (10)$$

Mahaux and Sartor argue that the energy dependence of the radial moments of $\langle r(E)^q \rangle_w$ can be parametrized by the form

$$\langle r(E)^q \rangle_w = \frac{C_q (E - E_f)^2}{(E - E_f)^2 + D_q^2}, \quad (11)$$

where C_q and D_q are constants to be fitted to the various moments of the imaginary potential. In addition, one expects $V_{hf}(r,E)$ to be a smooth function of energy. Hence it is reasonable to approximate its moments with

$$\langle r(E)^q \rangle_{hf} = A_q + B_q E. \quad (12)$$

When eqs. (11) and (12) are used, an analytic expression can be obtained for the various moments of the total real potential,

$$\langle r(E)^q \rangle_v = A_q + B_q E + \frac{C_q D_q (E - E_f)}{(E - E_f)^2 + D_q^2}. \quad (13)$$

For a given nucleus, values of $\langle r(E)^q \rangle_w$ can be deduced from a knowledge of the shape and strength of the imaginary potential. The values of C_q and D_q , eq. (11), are then adjusted so as to reproduce these results. Finally, A_q and B_q of eq. (13) are determined from a best fit to $\langle r(E)^q \rangle_v$ for $E > 0$. Eq. (13) is assumed to hold true for all values of E including $E < 0$. If one takes $V(r,E)$ to be a Woods-Saxon potential with a strength V_0 , radius r_v and diffuseness a_v , eq. (13) with $q = 0.8, 2$ and 4 can be used to determine these three parameters for $E < 0$. In this way Mahaux and Sartor found values of V_0 , r_v and a_v which satisfactorily reproduce the bound-state data for ^{89}Y and ^{208}Pb . Moreover, in the energy domain $E_f \leq E \leq 0$, r_v decreased with increasing binding energy.

The same analysis, outlined above, was used to determine the bound-state ^{59}Co potential using the values of $\langle r(E)^q \rangle_v$ and $\langle r(E)^q \rangle_w$ found in the preceding section. Since for incident neutron energies between 0 and 10.0 MeV, J_w , given by eq. (5), decreases in value, the simple expression, eq. (11), cannot be used to parametrize the moments of the imaginary potential. We have therefore replaced eq. (11) with

$$\langle r(E)^q \rangle_w = \alpha_q (E - E_f)^2 e^{-\beta_q (E - E_f)^2} + \frac{C_q (E - E_f)^2}{(E - E_f)^2 + D_q^2}, \quad (14)$$

where α_q and β_q are adjustable parameters and the expression is symmetric about the Fermi energy, $E_f = -12.25$ MeV. For $q = 2$, $\langle r(E)^q \rangle_w = J_w$, and the parameters of eq. (14) for $q = 2$ were adjusted to give a best fit to the sixteen values determined in the experiments of ref. 1, and the $E = 0$ value of eq. (5), plus the values of J_w determined from the Walter and Guss potential (29) evaluated at energies ranging from $E = 15.0$ to 37.5 MeV. For $q \neq 2$ the

imaginary-potential geometry given by eq. (3), together with the experimentally derived strengths, W_0 , were used to evaluate the moments for $E \leq 10.0$ MeV. These moments were combined with those evaluated from the Walter-Guss potential, again calculated from $E = 15.0$ to 37.5 MeV. The parameters of eq. (14) were then adjusted to give a best fit when $q = 0.8$ and 4 . Curves resulting from this fit are shown in fig. 7, where they are compared with the experimentally-derived values of $\langle r(E)^q \rangle_w$.

When eq. (14) is used to parametrize the moments of the imaginary potential, the moments of the real potential are given by

$$\langle r(E)^q \rangle_v = A_q + B_q E + \frac{C_q D_q (E - E_f)}{(E - E_f)^2 + D_q^2} + F_q(\alpha_q, \beta_q, (E - E_f)), \quad (15)$$

where $F_q(\alpha_q, \beta_q, (E - E_f))$ comes from the principal-value contribution of the exponential term of eq. (14). The parameters A_q and B_q of eq. (15) were then adjusted to give the best fit to the sixteen values, for each q , of $\langle r(E)^q \rangle_v$ determined from the experimental results of ref. 1. For $q = 2$, $\langle r(E)^2 \rangle_v = J_v$, and the fifteen values shown in fig. 1, together with $E = 0$ value given by eq. (5), were used. For $q = 0.8$ and 4 the values of $\langle r(E)^q \rangle_v$ to be fitted were calculated using the real-potential geometry of eq. (3).

Eq. (15) was assumed to hold for $E < 0$, and the form of the bound-state Woods-Saxon potential was determined from a knowledge of its $q = 0.8, 2$ and 4 moments. In fig. 8 the behavior of a_v , r_v and J_v is shown over the energy range $-16.0 \leq E \leq 10.0$ MeV. For $E > 0$, a_v and r_v reproduce quite well the values to which they were fitted. For $E < 0$, r_v increases with binding energy, reaching a maximum in the energy range under consideration, at approximately -10.0 MeV. This behavior is to be contrasted with that found for the doubly-closed-shell nucleus ^{208}Pb , and the closed neutron-shell nuclide ^{89}Y , where r_v decreases with increasing binding energy in the range $E_f \leq E \leq 0$ MeV (12,13,14). Of the three moments of the imaginary potential, $\langle r(E)^4 \rangle_w$ is the least well described by eq. (14), exhibiting an rms deviation which is 5.6% of its asymptotic value (in contrast to 3.9% and 4.7% for $q = 0.8$ and $q = 2$, respectively). As was done by Mahaux and Sartor (14) in their study of ^{89}Y , the values of V_0 and r_v obtained from a fit to only the $q = 0.8$ and $q = 2$ moments with a_v held fixed at 0.6355 fm were examined. Again r_v increases with increasing binding energy, reaching a maximum of 1.584 fm at -10.0 MeV, which is to be compared with the value 1.648 fm at -10.0 MeV shown in fig. 8. This increase in r_v with increasing binding energy almost certainly arises because J_w for ^{59}Co , at low energies, has an entirely different behavior than that obtained for either ^{89}Y or ^{208}Pb .

Also shown in fig. 8 is the curve representing J_v . This has the same general form as found by Mahaux and Sartor for ^{89}Y and ^{208}Pb . In addition to

the experimental values of J_v at positive energies, the values needed to reproduce the observed particle- and hole-state binding energies are shown in this figure. These experimental binding energies were determined from the mass tables (41) and the nuclear data sheets (42) for ^{57}Ni , and have incorporated into them the appropriate $(N - Z)/A$ correction, and the change in A in going from ^{57}Ni to ^{59}Co . In deducing these J_v 's, r_v and a_v were held fixed at the values predicted by eq. (15), for the observed binding energy, and V_0 was adjusted until agreement with the observed energy was obtained. The $f_{7/2}$ hole state requires a value of J_v approximately 13.5% greater than given by eq. (15), whereas, on the average, the particle states need a J_v value that is about 8.1% smaller. These discrepancies are probably due to the fact that ^{59}Co is a vibrational nucleus which has been treated in the above using a spherical OM.

IV SUMMARY

Differential elastic- and inelastic-scattering cross sections of ^{59}Co (1), together with the $\ell = 0$ strength function reported from resonance measurements (26) and the total cross sections given in ref. 27, provided the data base for spherical OM interpretations. The resulting OM potential and accompanying statistical-model calculations, provided a good description of: the $\ell = 0$ strength function, the neutron total cross section to 20 MeV, differential elastic-scattering cross sections to 10.0 MeV, and the inelastic-scattering cross sections to a few MeV. For incident-neutron energies above 3.0 MeV, both the magnitude and angular distribution of the observed inelastic scattering to the states between a 1.0 and 1.8 MeV excitation suggest a substantive direct-reaction component, and for $E > 5.0$ MeV this is the dominant excitation mechanism for these states. A quantitative description of this direct-reaction process is provided by the weak-coupling model in which the $f_{7/2}$ proton hole in ^{59}Co is coupled to the yrast 2^+ state in ^{60}Ni . Assuming that ^{60}Ni is a vibrational nucleus with $\beta_2 = 0.25$, calculations coupling the 0^+ (ground state), the 2^+ (one-phonon), and the 2^+ , 0^+ , 4^+ (two-phonon) states resulted in direct-excitation cross sections and angular distributions that, when combined with the statistical contribution, describe quite well the observed excitation of levels with $E_x \leq 1.8$ MeV.

The spherical OM parameters obtained in the present interpretation are strongly energy dependent in both strength and geometry. In particular: (i) the real radius is large at low energies and rapidly decreases with increasing energy to ≈ 7.0 MeV and then decreases much more slowly with energy in a manner consistent with "global" models (16), (ii) the real diffuseness is energy independent, (iii) the energy dependence of the imaginary radius follows that of the real radius but the magnitude is $\approx 4\%$ smaller throughout, (iv) the imaginary diffuseness approaches the δ -function value, at zero energy, rapidly increasing with energy to ≈ 7.0 MeV, and then becomes approximately constant, (v) the real potential strength decreases rapidly with increasing energy to ≈ 7.0 MeV, and then more slowly at higher energies in the manner reported for "global" models(16), and (vi) the imaginary strength is large and decreases with increasing energy.

Characteristics (i), (ii), (iv) and (v) are qualitatively similar to those recently reported in ^{209}Bi (19). The break in the energy dependence of the present ^{59}Co potential occurs approximately 19.0 MeV above the Fermi energy, whereas the similar break in the ^{209}Bi potential is approximately 16.0 MeV above the Fermi energy. The energy difference between the two break points may not be significant since the transition is relatively slow and thus the break point not well defined. This energy dependence of both geometry and strength of the OM makes possible a good description of the observables over a wide energy range, including agreement with the data at lower energies. It is tempting to associate this change in energy dependence with the onset of the Fermi surface anomaly (17). Property (vi) may be in part due to the use of the spherical OM to interpret neutron scattering from a vibrational nucleus.

The OM derived from the neutron-scattering results was extrapolated to the bound-state regime using the dispersion relation (15) and the method of moments recently outlined by Mahaux and Sartor (12,13,14). The imaginary-potential moments, defined by eq. (10), were parameterized by an expression symmetrical about the Fermi energy, eq. (14), with parameters derived by fitting the results of the present interpretation of neutron scattering from ^{59}Co , extended to approximately 40.0 MeV using the potential of ref. 29. The additional constants, A_q and B_q of eq. (15), needed to parameterize the real moments were determined by fitting to the values found in the present analysis of the 0 to 10.0 MeV ^{59}Co data. Extrapolated to bound energies, this parameterization indicates a minimum in the real diffuseness and a maximum in the real radius at approximately -10.0 MeV. The behavior of r_v , which increases with increasing binding energy, is the opposite of that found in ^{89}Y and ^{208}Pb where r_v becomes smaller as one approaches the Fermi energy (12,13,14). This difference reflects the energy dependence of the imaginary potential at low energies which is quite different from that reported for ^{89}Y and ^{208}Pb . On the other hand, J_v peaks at ≈ -10.0 MeV, in the same general manner as found by Mahaux and Sartor for ^{89}Y and ^{208}Pb (12,13,14). The average J_v implied by the ^{59}Co bound particle states is approximately 8% smaller than that obtained from the moments analysis, and that for the hole state is approximately 13% larger. For both particle- and hole-states the required strengths are much larger than would be given by linear extrapolation of the J_v values implied by the higher-energy (i.e., ≥ 7.5 MeV) Cobalt neutron-scattering data, or by global models(16,29).

REFERENCES

- 1 A. B. Smith, P. T. Guenther, J. F. Whalen and R. D. Lawson, Argonne National Laboratory report, ANL/NDM-101 (1987)
- 2 B. Holmqvist and T. Wiedling, Aktiebolaget Atomenergi report, AE-430 (1971)
- 3 D. Wilmore and P. E. Hodgson, J. Phys. G11 (1985) 1007
- 4 P. Guenther, A. Smith and J. Whalen, Nucl. Sci. and Eng. 82 (1982) 408
- 5 A. Smith, P. Guenther, D. Smith and J. Whalen, Nucl. Sci. and Eng. 72, (1979) 293
- 6 P. A. Moldauer, Nucl. Phys. 47 (1963) 65
- 7 A. Smith and P. Guenther, Proc. Conf. on Nucl. Structure Study with Neutrons, page 508, Antwerp, North-Holland Pub. Co., Amsterdam (1965)

- 8 P. A. Moldauer, Nucl. Phys. A344 (1980) 185
- 9 W. P. Poenitz, A. B. Smith and J. F. Whalen, Nucl. Sci. and Eng. 78 (1981) 333
- 10 A. B. Smith, P. T. Guenther and J. F. Whalen, Nucl. Phys. A415 (1984) 1
- 11 See e.g., C. Johnson, A. Galonsky and R. Kernell, Phys. Rev. C20 (1979) 2052
- 12 C. Mahaux and R. Sartor, Phys. Rev. Lett. 57 (1986) 3015
- 13 C. Mahaux and R. Sartor, Nucl. Phys. A468 (1987) 193
- 14 C. Mahaux and R. Sartor, Phys. Rev. C36 (1987) 1777
- 15 See e.g., G. R. Satchler, Direct nuclear reactions (Clarendon, Oxford, 1983)
- 16 J. Rapaport, Phys. Reports 87 (1982) 25
- 17 C. Mahaux and H. Ngô, Nucl. Phys. A378 (1982) 205; Phys. Lett. 100B (1981) 285
- 18 R. D. Lawson, P. T. Guenther and A. B. Smith, Phys. Rev. C34 (1986) 1599
- 19 A. B. Smith, P. T. Guenther and R. D. Lawson, Argonne National Laboratory report, ANL/NDM-100 (1987); Phys. Rev. C36 (1987) 1298
- 20 See e.g., P. E. Hodgson, Nuclear reactions and nuclear structure (Clarendon, Oxford, 1971)
- 21 ABAREX, A spherical optical-model code, P. A. Moldauer, private communication (1983), and as revised by R. D. Lawson (1986)
- 22 W. Hauser and H. Feshbach, Phys. Rev. 87 (1952) 366
- 23 P. A. Moldauer, Nucl. Phys. A344 (1980) 185
- 24 P. Anderson, L. Ekstrom and J. Lyttkens, Nucl. Data Sheets 39 (1983) 641
- 25 A. Gilbert and A. Cameron, Can. Phys. 43 (1965) 1446
- 26 S. F. Mughabghab, M. Divadeenam and N. E. Holden, Neutron cross sections, vol. 1, pt A (Academic, NY, 1981)
- 27 M. Sugimoto and A. B. Smith, to be published
- 28 National Nuclear Data Center, Brookhaven National Laboratory
- 29 R. L. Walter and P. P. Guss, Proc. Conf. on Nucl. Data for Basic and Applied Science, vol 2, p. 1079 (Gordon and Breach, NY 1986)
- 30 P. A. Moldauer, ANLECIS computer code, private communication (1983)
- 31 P. Andersson, L. P. Ekstrom and J. Lyttkens, Nucl. Data Sheets 48, (1986) 251
- 32 P. T. Guenther, D. L. Smith, A. B. Smith and J. F. Whalen, Ann. Nucl. Energy 13 (1986) 601
- 33 A. M. Lane, J. Lynn, E. Melkonian and E. Rae, Phys. Rev. Lett. 2 (1959) 424; W. Vonach, A. B. Smith and P. A. Moldauer, Phys. Lett. 11 (1964) 331; A. B. Smith, P. T. Guenther and J. F. Whalen, Nucl. Phys. A415 (1984) 1
- 34 R. W. Hasse and P. Schuck, Nucl. Phys. A438 (1985) 157
- 35 J. R. Rook, private communication (1986)
- 36 D. Wilmore and P. E. Hodgson, Nucl. Phys. 55 (1964) 673
- 37 S. Cohen, R. D. Lawson, M. H. Macfarlane, S. P. Pandya and M. Soga, Phys. Rev. 160 (1967) 903
- 38 A. K. Kerman and C. M. Shakin, Phys. Lett. 1 (1962) 151
- 39 R. D. Lawson, A. B. Smith and M. Sugimoto, Bull. Am. Phys. Soc. 32 (1987) 32
- 40 F. G. Perey, Phys. Rev. 131, (1963) 745
- 41 A. H. Wapstra and K. Bos, At Nucl. Data Tables 19 (1977) 177
- 42 T. W. Burrows and M. R. Bhat, Nucl. Data Sheets 47 (1986) 1

OPTICAL-MODEL CALCULATIONS FOR EXPERIMENTAL
INTERPRETATION AND EVALUATION:
PRACTICAL CONSIDERATIONS AND FUNDAMENTAL
IMPLICATIONS*

Alan B. Smith, Peter T. Guenther and
Robert D. Lawson
Argonne National Laboratory
Argonne, Illinois, USA

NATURE OF THE ENDEAVOR

- Coordinated Measurement, Calculation and Evaluation
 - New Physical Observables
 - Enhanced Fundamental Understanding
 - Practical Application to Applied Evaluation Problems
 - Interactive Program Elements
 - Timely Responsiveness

SCOPE

- Structural Materials
 - A \approx 50-60, 90-100 and 204-209
 - Structural Components and Associated Multipliers
 - For Fusion- and Fission-Energy Development
- Neutron-Induced Reactions Important to Neutronic Design
 - 10⁻⁵ eV to 20.0 MeV
- Final Products
 - Enhanced Fundamental Understanding
 - Applicable to Extrapolation and Interpolation of Experimental Data Base.
 - Comprehensive Neutronic Evaluations
- Applied Physics Remains an Observational Science

* This work supported by the United States Department of Energy under contract with the University of Chicago

ISSUES

- Persistent Enigmas
 - Particularly in $A \approx 50-60$ Region

- Higher-Energy Optical And Coupled-Channels Models
 - Don't Reasonably Extrapolate to Low Energies
 - Discontinuities at a Few MeV
 - Qualitatively Different Strengths and Geometries
 - Particularly the Imaginary Potential
 - Failure to Extrapolate to Bound Energies
 - Fluctuations are a Concern
 - S-Wave Strength Function can be Large
 - Large Corrections to Compound-Nucleus X-sec.
 - Uncertain Excited States
 - Discrete Levels
 - Statistical Continuum
 - Detrimental Impact on Compound-Nucleus Estimates
 - Fluctuations Distort Observables
 - Total and Partial Cross Sections
 - Broad Averages for Optical-Model Interpretation
 - Dichotomy Between Channel Competition and Averaging Increment
 - Collective Properties
 - Generally Vibrational, but Not Pure

- Fundamental Concepts and Computational Methods
 - Dispersion Relation
 - Links Real and Imaginary Potentials
 - Implies Energy-Dependent Geometries and Strengths
 - Method of Moments (Mahaux and Sartor)
 - Evaluate Potential Over Wide Energies
 - Extrapolate to Bound Regime
 - Displays Fermi-Surface-Anomaly

- Illustrate Problems and Computational Solutions With---
- A Heavy Structural Multiplier-- Bismuth
- Structural Component Materials-- Vanadium and Cobalt
- Comprehensive Draft Evaluations of Each

PROJECT STATUS

- Mass 50 - 60 Region
 - Cobalt
 - Measurements and Calculations-- Done
 - Evaluation-- Near Completion
 - Preliminary Results at last Meeting
 - Vanadium
 - Measurements-- Done
 - Calculations-- In Progress
 - Evaluation-- Near Completion
 - Nickel-58
 - Measurements and Calculations-- Well Along
 - Evaluation-- Started
 - Iron and Chromium
 - Measurements and Calculations-- In Progress

- Mass \approx 90 - 100 Region
 - Niobium and Yttrium-- Completed
 - Reported at Last Meeting
 - Evaluated Files Submitted
 - Zirconium
 - Measurements-- Well Along
 - Calculations-- Slow, Difficulties with Handling Isotopes
 - Evaluation-- Starting
 - Strontium-- Work Started

● **Mass 208 Region, Structural Blankets and
Multipliers**

- **Bismuth**

**Measurements and Calculations--
Complete**

Evaluation-- Nearing Completion

MASS 209- BISMUTH

● Massive Structural Component and Multiplier

- Fusion-Energy Systems, particularly ceramic
- Very Large (n,2n) Cross Sections

● Rigorous Experimental Interpretation

- χ^2 Fitting of Extensive Elastic-Scattering Data
 - 1.5 to 10.0 MeV
- Also Consideration of:-
 - $l = 0$ Strength Function
 - σ_t to 20.0 MeV

● Spherical Optical Model

- "Conventional"
- Surface-Peaked Real Potential
 - Inplied by Dispersion Relation

$$V(r, E) = V_{hf}(r, E) + \frac{P}{\pi} \int_{-\infty}^{+\infty} \frac{W(r, E') dE'}{(E-E')}$$

- Energy-Dependent Geometries
 - Defined by Observables

● "Conventional" Model Parameters

- Spin-Orbit

$$\begin{aligned}V_{so} &= 5.22 \text{ MeV} \\r_{so} &= 1.0 \text{ fm} \\a_{so} &= 0.65 \text{ fm}\end{aligned}$$

- Real/Imaginary Geometries

$$\begin{aligned}r_v &= (1.36 - 0.0175 \times E), \text{ fm} \\r_w &= 1.3102, \text{ fm} \\a_v &= (0.54 + 0.02 \times E), \text{ fm} \\a_w &= (0.05 + 0.055 \times E), \text{ fm}\end{aligned}$$

- Note the Strong Energy Dependences

- Real/Imaginary Strengths
(in volume-integral-per-nucleon, J)

$$\begin{aligned}J_v &= 459.8 - 9.6 \times E, \text{ MeV-fm}^3 \\J_w &= 33.9 + 1.05 \times E, \text{ MeV-fm}^3\end{aligned}$$

- "Conventional" Energy Dependences
- Some Decrease in J_v at Low Energies

Fluctuations?

No Appreciable Effect

● Surface-Peaked Real Potential; i.e. Dispersion Relation

- Iterative Interpretation
- Again, Energy-Dependent Geometries

$$r_v = 1.28 - 0.007 \times E, \text{ fm}$$

$$a_v = 0.68, \text{ fm}$$

$$r_w = 1.3022, \text{ fm}$$

$$a_w = 0.119 + 0.043 \times E, \text{ fm}$$

Note Effect of Surface Component

- Real/Imaginary Strengths

$$J_{ws} = 422.4 - 4.83 \times E, \text{ MeV-fm}^3$$

$$J_w = 31.0 + 1.41 \times E, \text{ MeV-fm}^3$$

- Consideration of Inelastic Scattering

Supports Continuum-Inelastic Representation

- Calculated and Observed Polarizations Consistent
- $l = 0$ Strength Function Sensitive to a_w

● Bound-Energy Potential

- Implied by Energies of Particle- and Hole-States
- Extrapolation is Qualitatively Consistent with Observation

Sensitive to Energy Dependence of J_{ws} at Bound Energies

Qualitatively Superior to Linear Extrapolation from Positive Energies

● Higher Energies (Above ≈ 10.0 MeV)

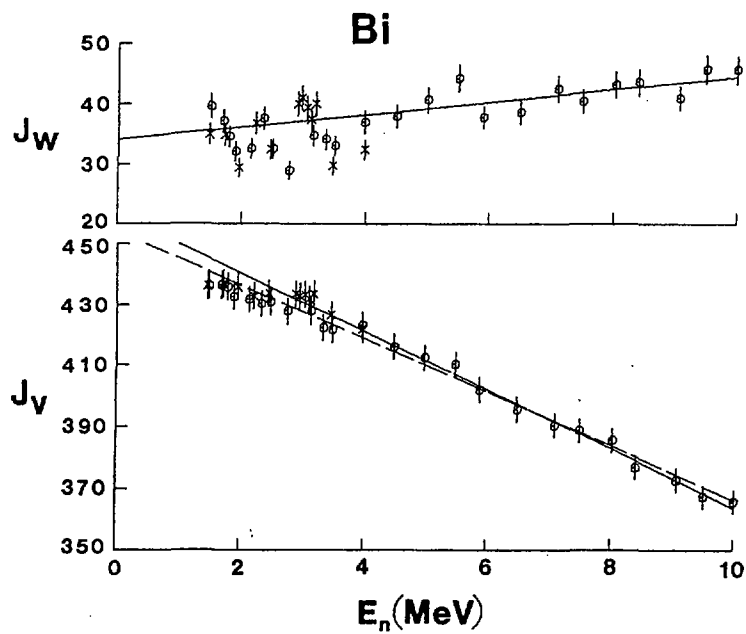
- Potential Meets High-Energy ²⁰⁸Pb Potential (Mahaux et al.)
 - Match Point ≈ 10.0 MeV
 - i.e., ≈ 16 MeV Above Fermi Energy
 - Manifestation of Onset of Fermi-Surface-Anomaly

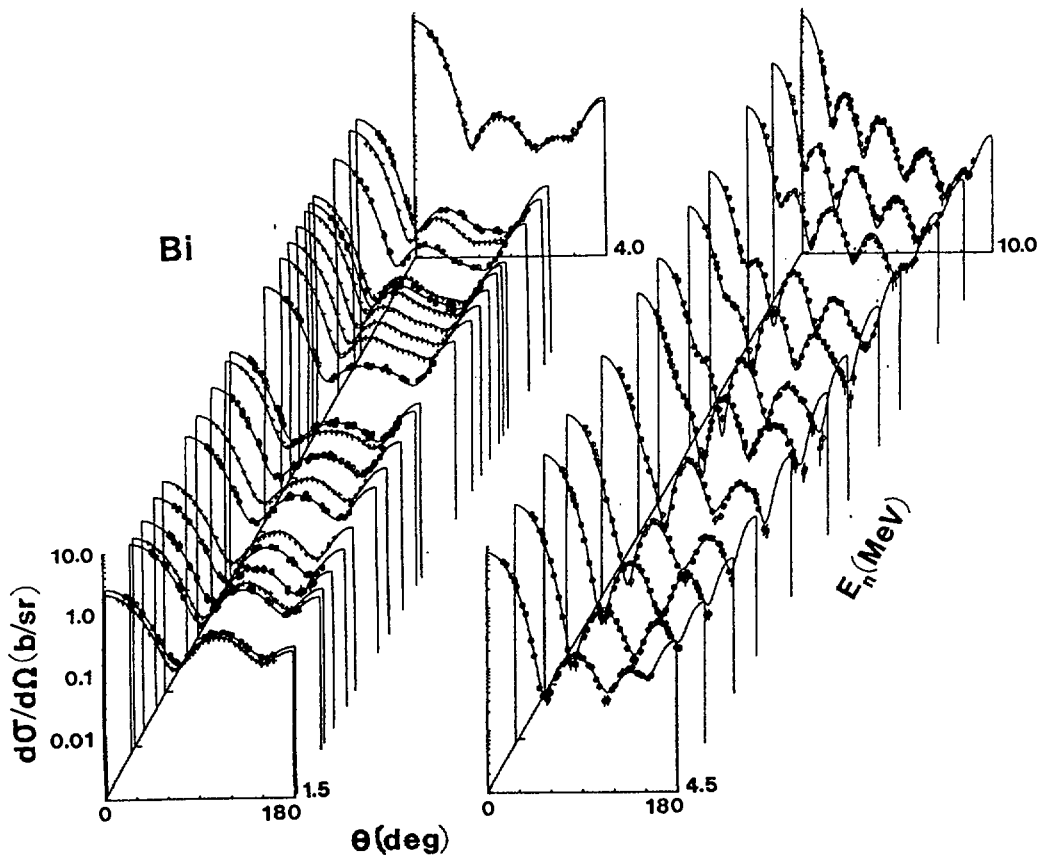
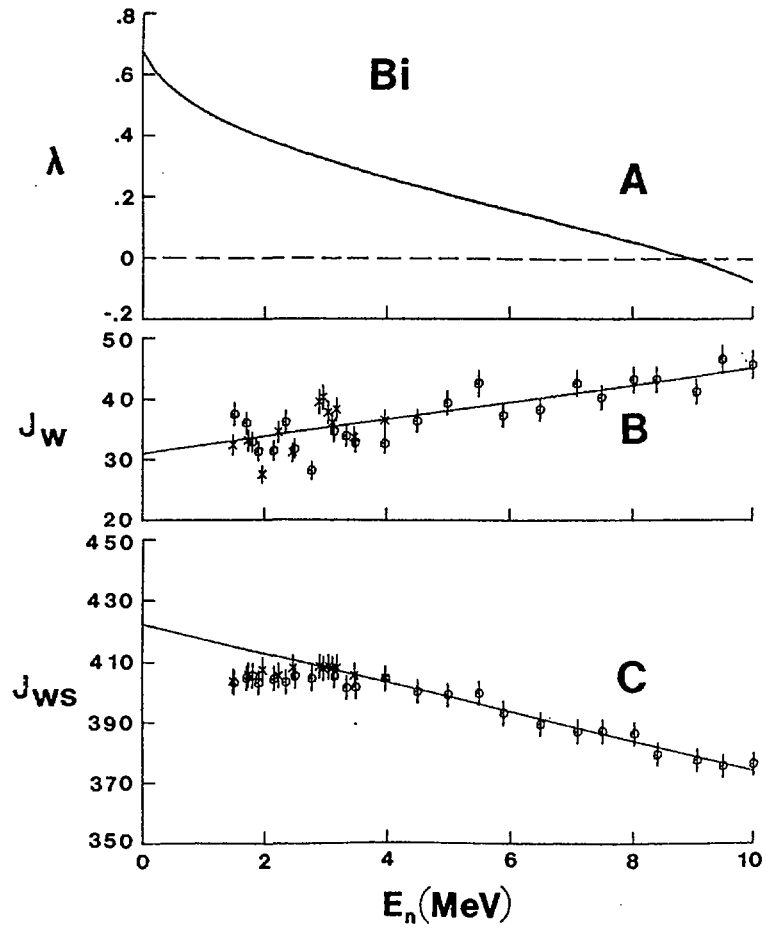
● Character of Composite Model Essential to Account for

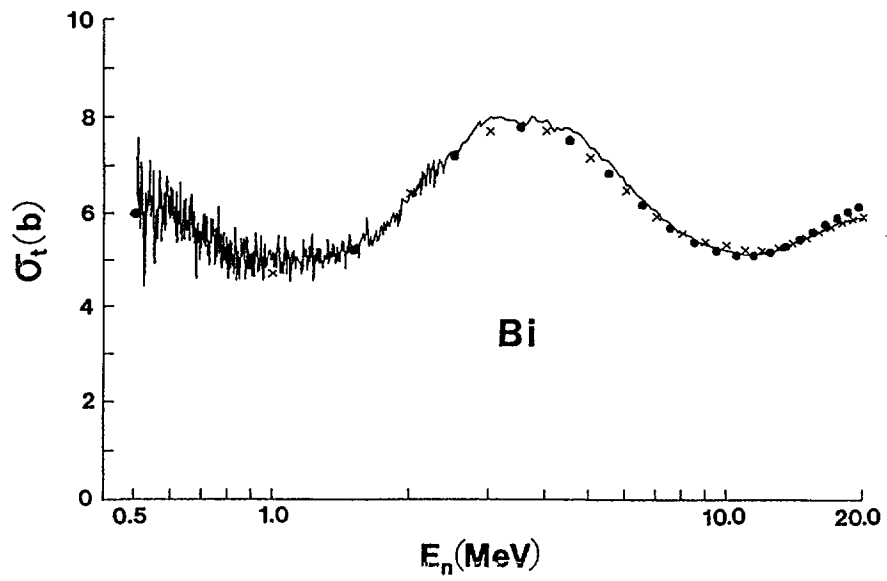
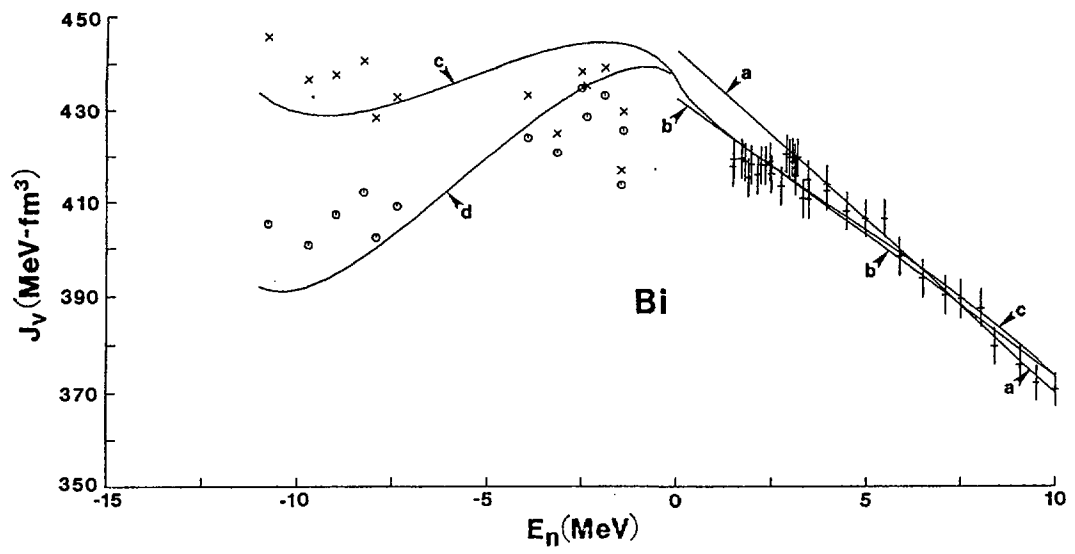
- Observables, Positive and Negative Energy
- The Fermi-Surface-Anomaly

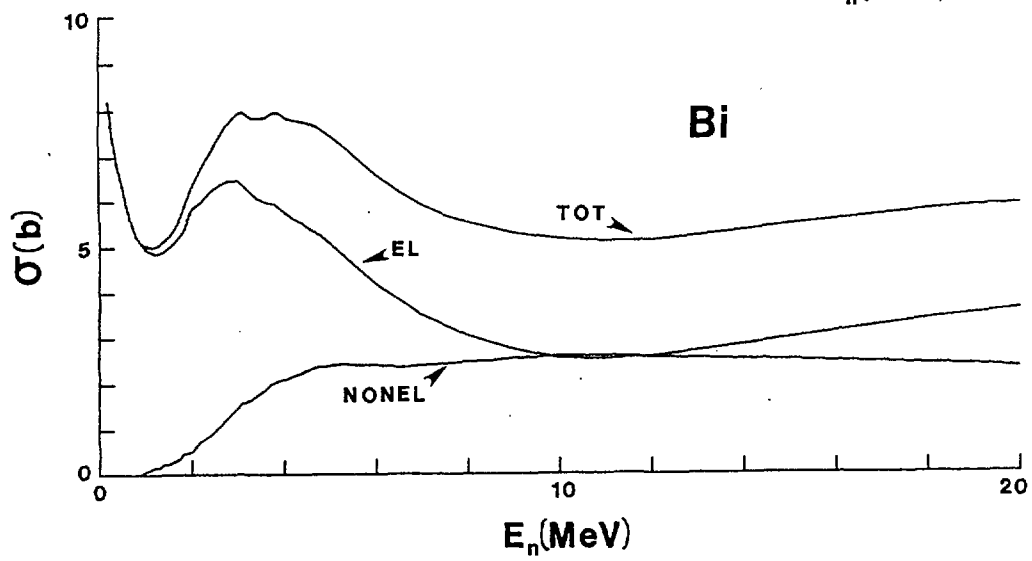
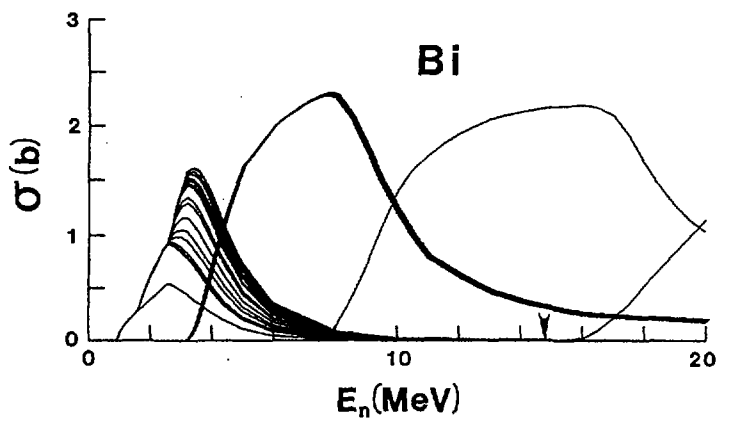
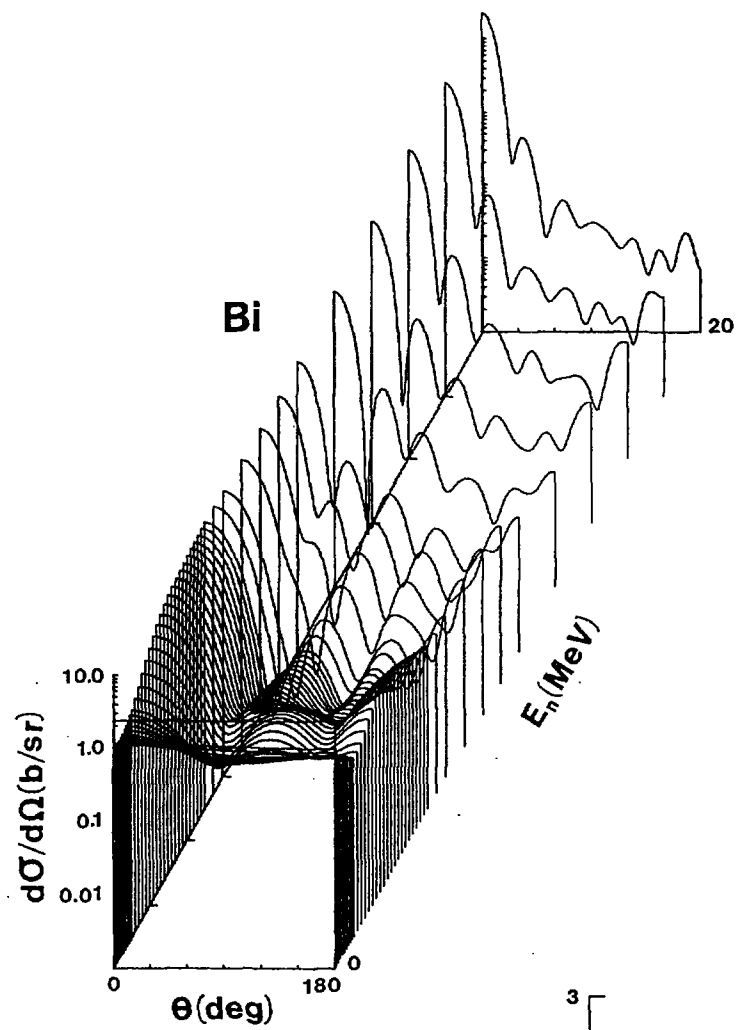
● Combined Potential Gives Excellent Result For Evaluation

- Total Cross Sections
- Partial Cross Sections
- Basis for Statistical Reaction Calculations
- Utilized in Associated Evaluation









MASS 50-60-COBALT

● Structural Material

- Fusion- and Fission-Energy Systems

● Rigorous Experimental Interpretation

- χ^2 Fitting of Extensive Elastic-Scattering Data

$\approx 1.5 - 11.0$ MeV

- Consideration of:-

σ_t to 20.0 MeV

$l = 0$ Strength Function

Inelastic-Scattering Processes

● Spherical-Optical and Coupled-Channels Models

- Energy-Dependent Geometries and Strengths
- Weak-Coupling Model
- Method of Moments (Mahaux and Sartor)
- Dispersion Relation

$$V(r,E) = V_{hf}(r,E) + \frac{P}{\pi} \int_{-\infty}^{+\infty} \frac{W(r,E') dE'}{(E-E')}$$

● Model Parameters

- Adjusted Gilbert and Cameron Level Formulation

Governed by Experimental Comparisons,
(Elastic and Inelastic Scattering)

- Spin-Orbit

$$V_{so} = 5.5, \text{ MeV}$$

$$r_{so} = 1.0, \text{ fm}$$

$$a_{so} = 0.65, \text{ fm}$$

Based Upon 9-11 MeV Data

- Real Potential

$$r_v = 1.39 - 0.0168 \times E \quad (E \leq 7.5 \text{ MeV}), \text{ fm}$$

$$= 1.288 - 0.0032 \times E \quad (E \geq 7.5 \text{ MeV}), \text{ fm}$$

$$a_v = 0.6355, \text{ fm}$$

$$J_v = 550.0 - 12.5 \times E \quad (E \leq 7.5 \text{ MeV}), \text{ MeV-fm}^3$$

$$= 474.0 - 2.4 \times E \quad (E \geq 7.5 \text{ MeV}), \text{ MeV-fm}^3$$

- Imaginary Potential

$$r_w = 0.96 \times r_v, \text{ fm}$$

$$a_w = 0.19 + 0.0386 \times E \quad (E \leq 7.5 \text{ MeV}), \text{ fm}$$

$$J_w = 135.0 - 6.4 \times E \quad (E \leq 7.5), \text{ MeV-fm}^3$$

$$= 104.0 - 2.3 \times E \quad (E \geq 7.5), \text{ MeV-fm}^3$$

Strengths Given in Volume-
Integral/Nucleon

● Note

- Energy Dependences

Changes at ≈ 7.5 MeV

≈ 19 MeV Above Fermi Energy

- Small $E = 0$ Value of a_w

- Large Value of J_w

- Anomalous Energy Dependence of J_w

- Above ≈ 7.5 MeV Similar to "Global" Models

● Excellent Description of:-

- Elastic Scattering to 11 MeV

- σ_t to 20+ MeV

Even Below ≈ 3 MeV, Not Achieved with
"Global" Models

- $l = 0$ Strength Function

● Inelastic Scattering

- Good Description at Low Energies

Statistical Processes

- Clearly Direct Processes at Higher Energies

For First Seven Levels

σ Grossly Exceeds Statistical
Calculation

Distributions Highly Anisotropic

● Assume Weak-Coupling Model

- $f_{7/2}$ Proton Hole Coupled to First 2^+ Level
in ^{60}Ni

- One- and Two-Phonon Vibrational Coupling,
 $\beta_2 = 0.25$

- Calculated Result Consistent with Observed Excitations of the First Seven Levels.
- Spherical Model of Deformed Target Implies:-
 - Negative dJ_w/dE , as observed
 - Large Values of J_w

Also Other Factors:- e.g.,
Shell Closure

● Extrapolation to Bound Energies

- Method of Moments (Mahaux and Sartor)
- Parameterize

$$\langle r(E)^q \rangle_w = \frac{4\pi}{A} \int_0^\infty W(r, E) r^q dr$$

for $q = 0.8, 2$ and 4

- Adjust to Fit 4 - 11 MeV Data

Dispersion Relation Relates Moments of
Real and Imaginary Potentials

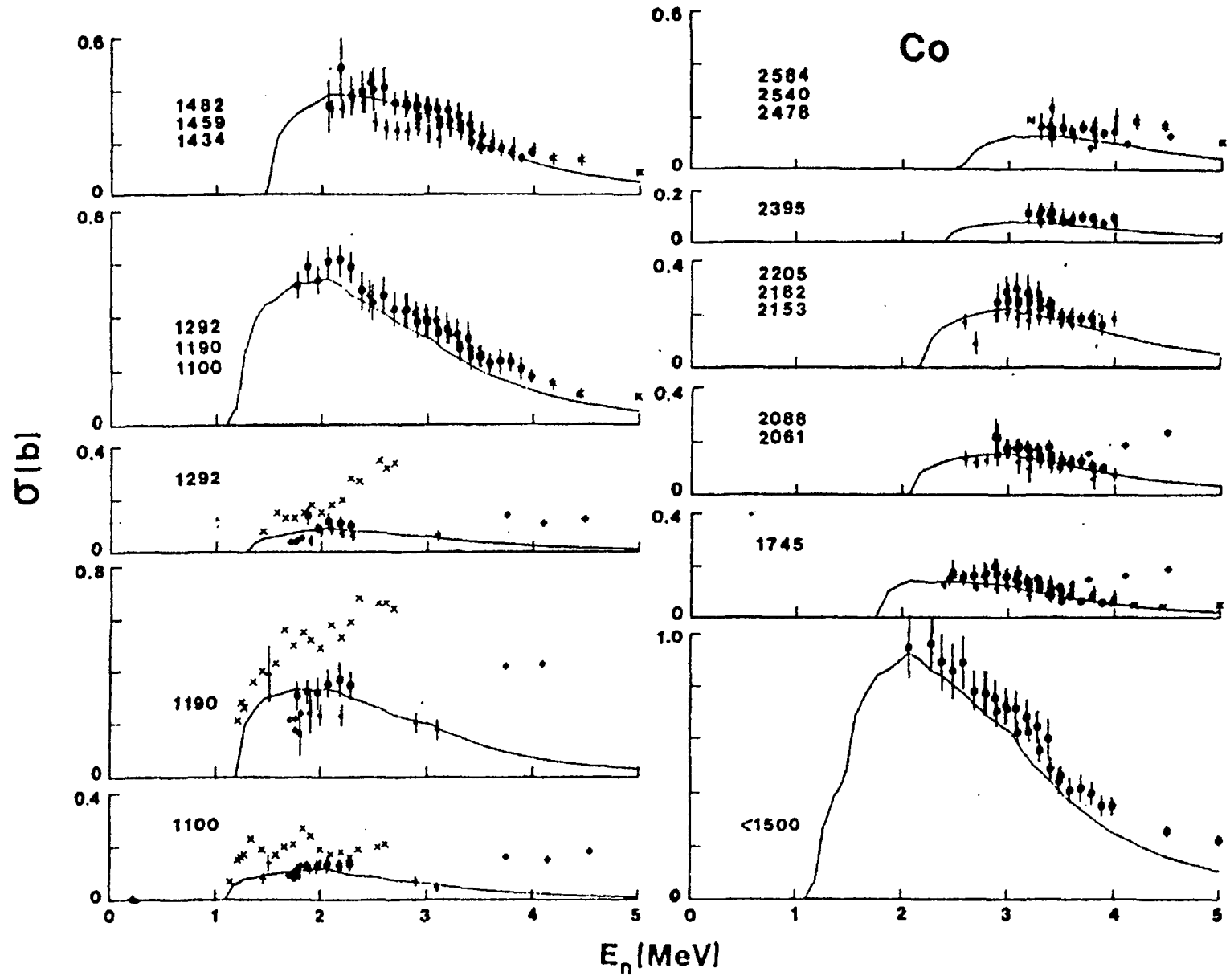
- Moments are Strongly Energy Dependent
- Imply Bound-Energy Potential Consistent with Particle- and Hole-State Energies

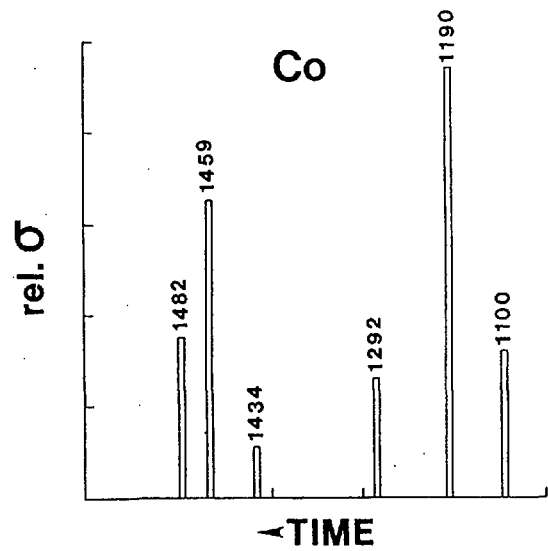
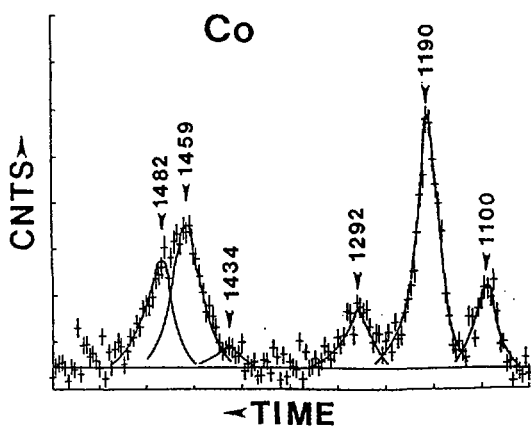
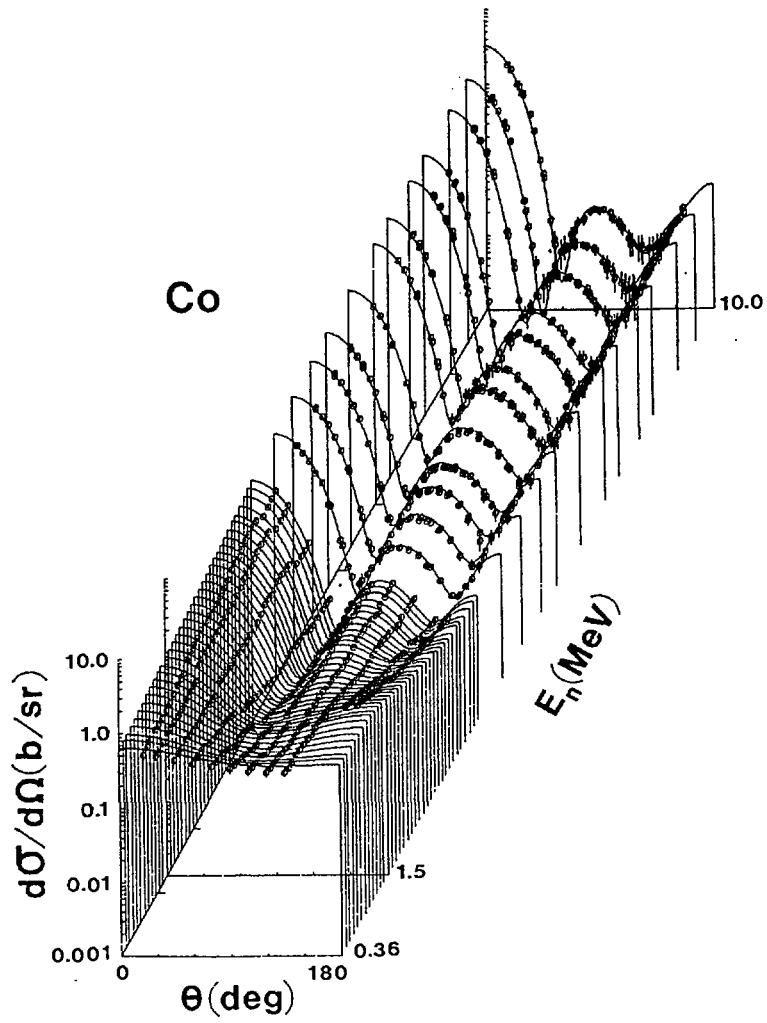
Energy Dependence is Strong

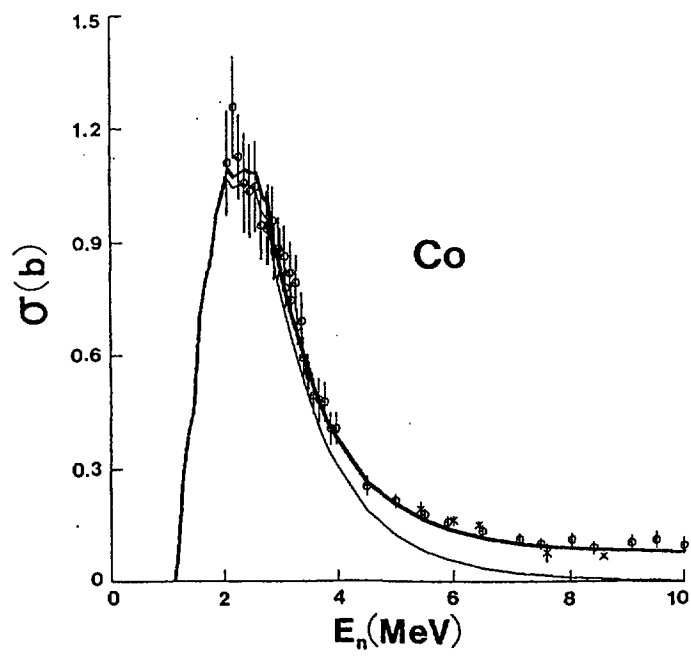
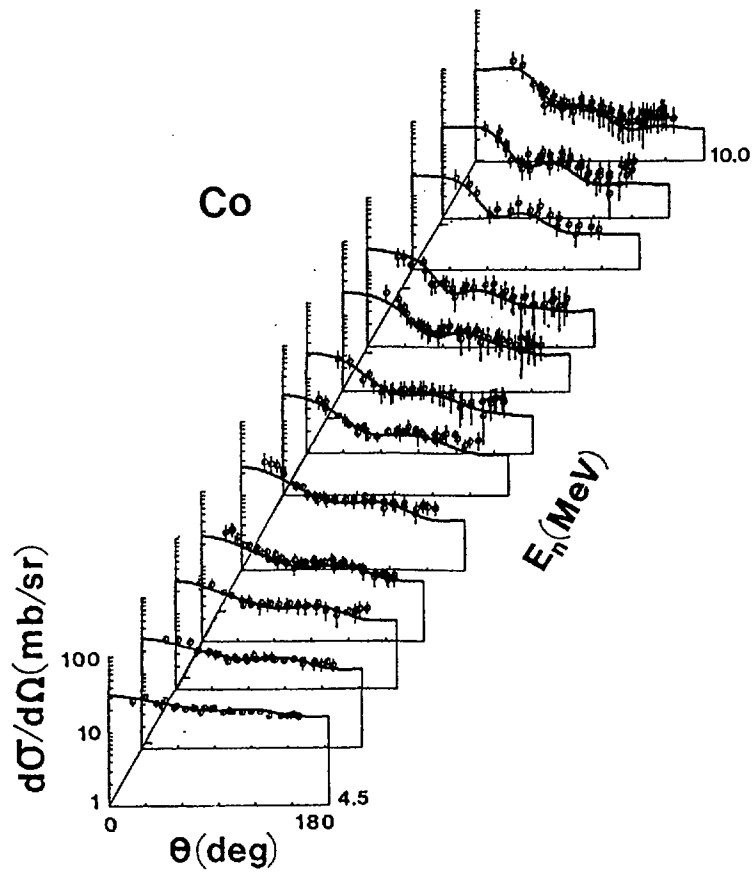
a_v Goes through a Minimum
 r_v a Maximum (influenced by negative
 dJ_w/dE at Positive Energies)
 J_v a Maximum all at ≈ -7 MeV

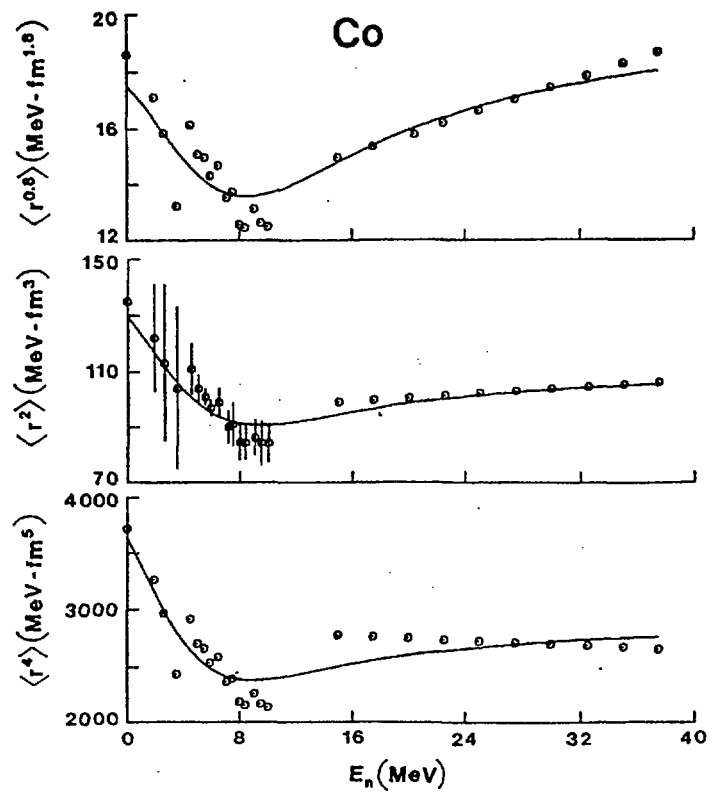
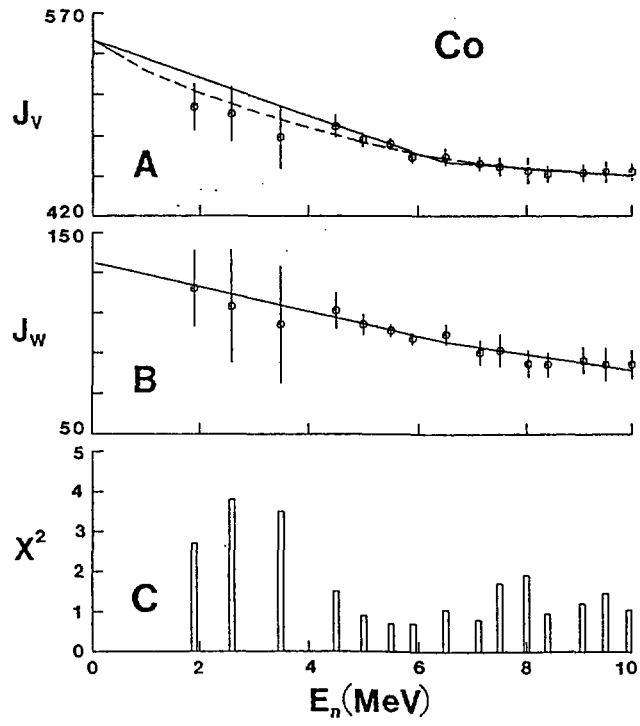
● Application to Evaluation

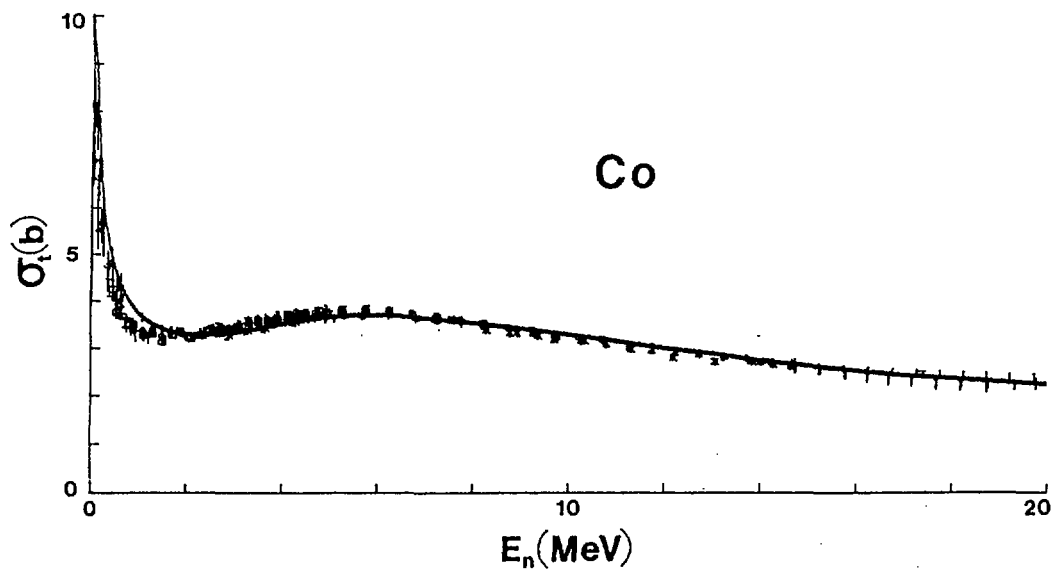
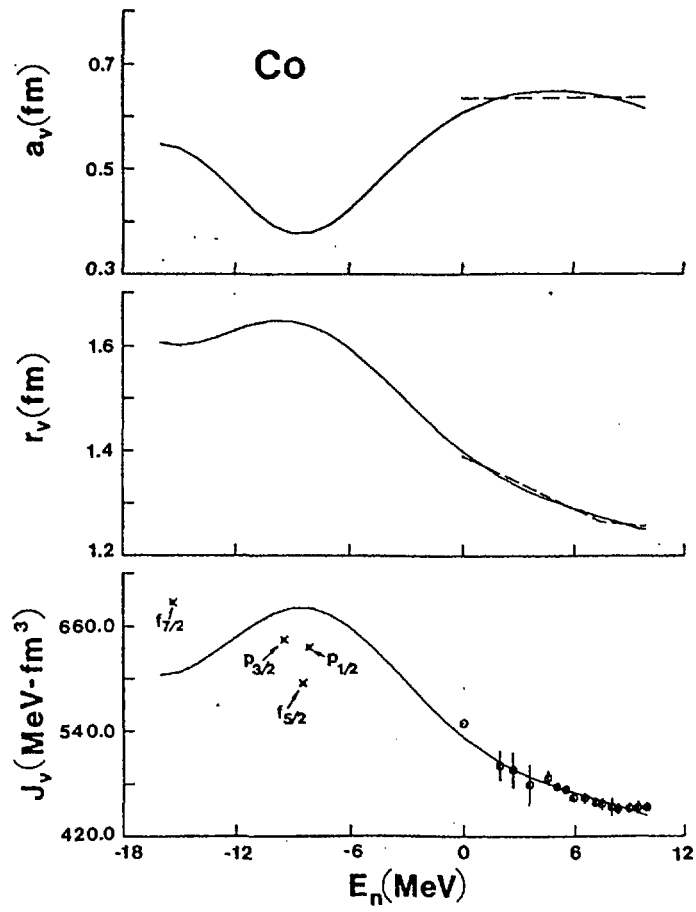
- Total Cross Section
- Elastic Scattering Cross Section
- Inelastic-Scattering Cross Section
- Basis for Statistical-Model Calculations of Other Reaction Cross Sections











MASS 50-60, VANADIUM
(A Status Comment)

● Fusion Structural Material

- High Temperature and Tritium Containment

● Experimental Measurements Completed

● Initial "Conventional" Optical-Model Interpretation

- χ^2 Fitting of Elastic Scattering
- Consideration of $l = 0$ Strength Function

● Fluctuations a Major Concern

● Energy Dependent Strengths and Geometries

$$J_v \approx 503 - 8.3 \times E \quad (E \leq 6.1 \text{ MeV}), \text{ MeV-fm}^3$$

$$\approx 470 - 2.9 \times E \quad (E \geq 6.1 \text{ MeV}), \text{ MeV-fm}^3$$

$$r_v \approx 1.34 - 0.009 \times E \quad (E \leq 10.0 \text{ MeV}), \text{ fm}$$

$$\approx 1.25 \quad (E \geq 10.0 \text{ MeV}), \text{ fm}$$

$$a_v \approx 0.574, \text{ fm}$$

$$J_w \approx 53 + 3.1 \times E, \text{ MeV-fm}^3$$

$$r_w \approx 1.025 \times r_v, \text{ fm}$$

$$a_w \approx 0.1 + 0.08 \times E \quad (E \leq 6.1 \text{ MeV}), \text{ fm}$$

$$\approx 0.92 - 0.052 \times E \quad (6.1 \leq E \leq 10.0 \text{ MeV}), \text{ fm}$$

$$\approx 0.4 \quad (E \geq 10.0 \text{ MeV}), \text{ fm}$$

- There are Uncertainties due to Fluctuations

● However, General Trends are:-

- Break in the Potential at ≈ 6 MeV: i.e., ≈ 16 MeV Above the Fermi Energy

The Fermi Surface Anomaly

$$dJ_{v(w)}/dE = -(+) \text{ in "Conventional" Manner}$$

Vanadium not deformed

- Magnitude of J_w Relatively Small

No Deformation, Closed Neutron Shell

$$r_w > r_v$$

$$a_w \rightarrow \delta\text{-function as } E \rightarrow 0$$

● Reasonably Descriptive of :-

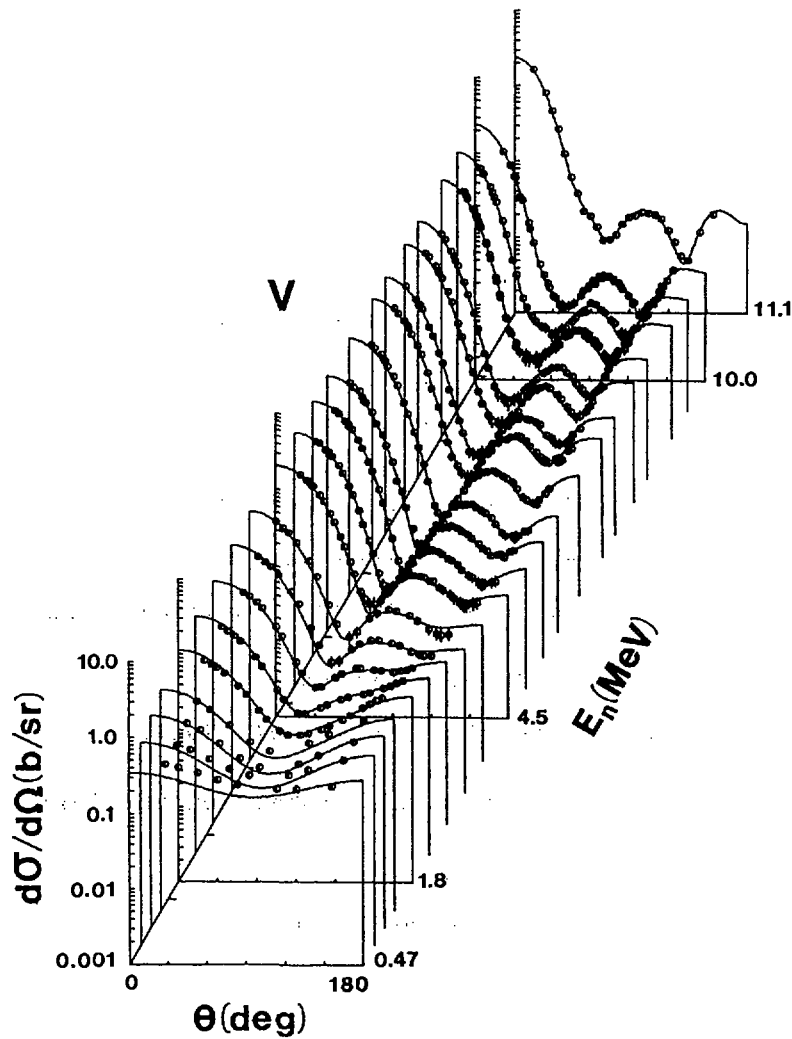
- Elastic Scattering to 11 MeV.
- Inelastic Scattering
- σ_t to 20 MeV

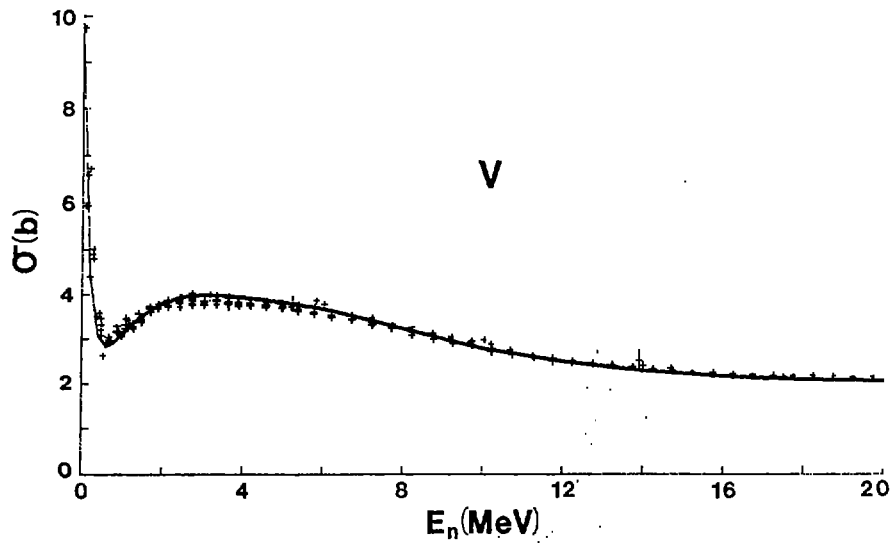
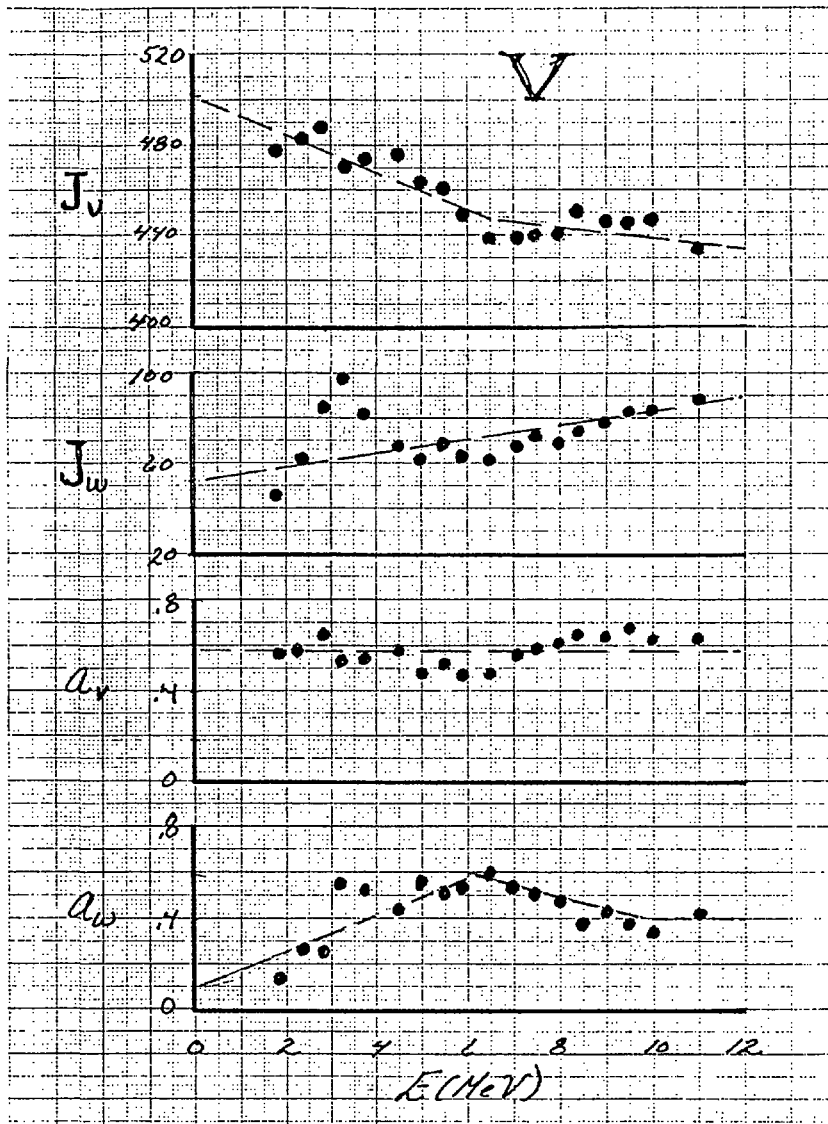
Particularly the Minimum at ≈ 1 MeV

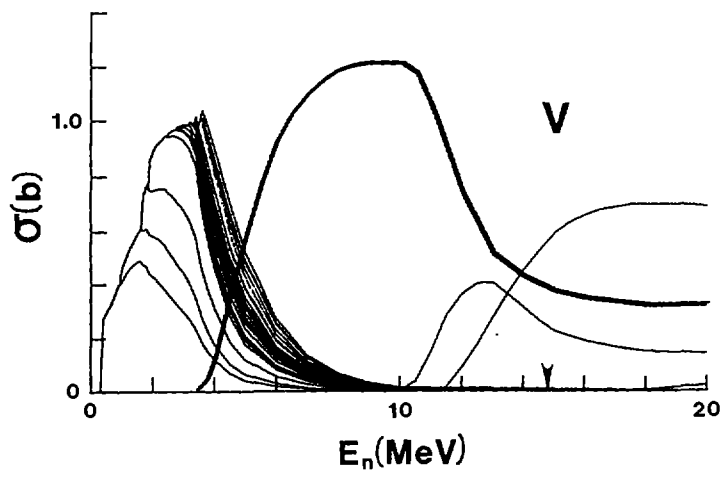
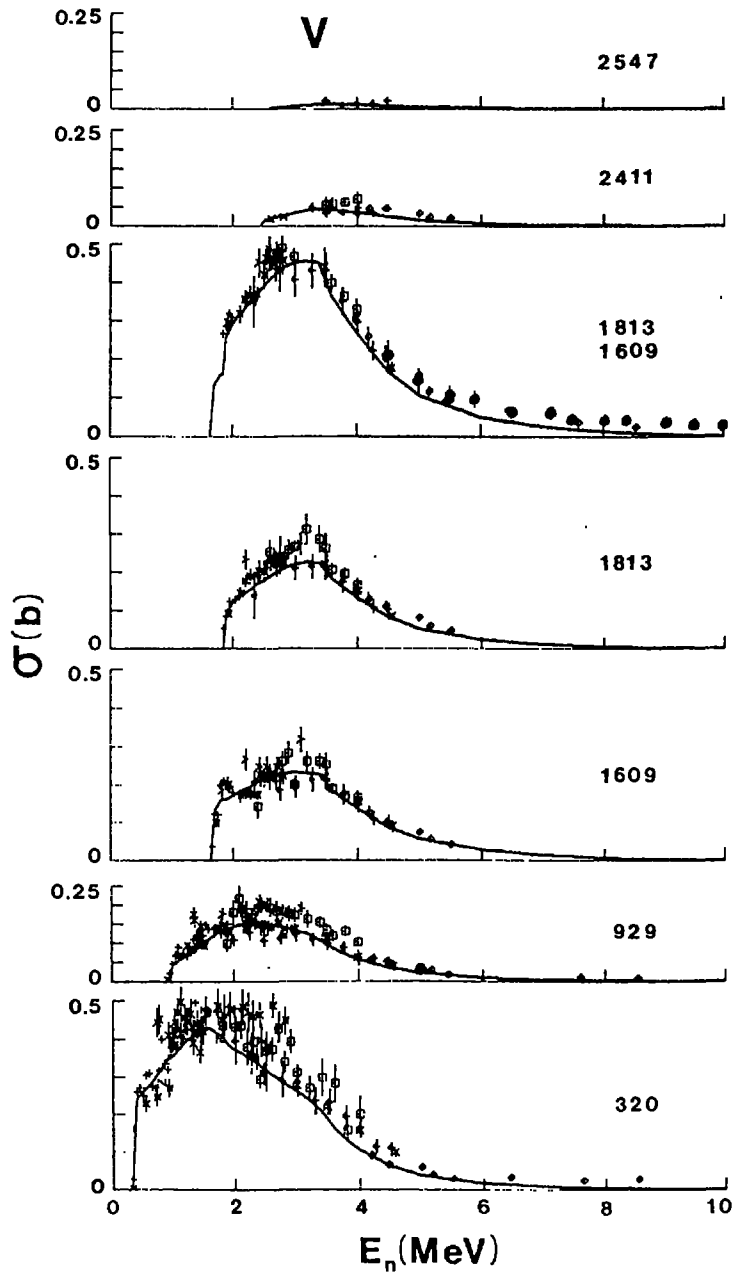
● Dispersion Relation and Method of Moments--
In Progress

- Smooth Trends in Place of Linear Segments
- Reasonably Description of Scattering
- Consistent with Bound Particle- and Hole-States

● Applied to Evaluation



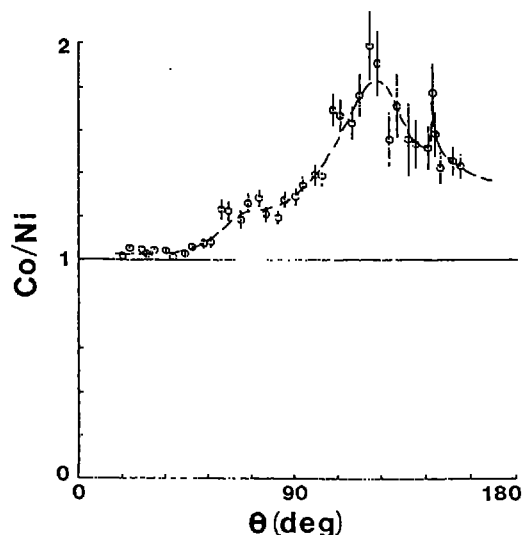




GENERALITY

- Conventional "Global" Models are only Very Qualitative
- Strengths and Geometries are Energy Dependent
 - The Behavior is complex
 - Necessary for Reliable Predictions
 - At Positive and Negative Energies
 - Apparent Onset of the Fermi-Surface-Anomaly
 - 15-18 MeV above the Fermi Energy
- Differences are only Partly Attributable to
 - Collective Effects
 - Shell Closures
- Structure is Reflected in the Imaginary Potential
 - The Strength is Strongly Mass Dependent
- Uncertain Level Densities at Low Excitations
 - A Major Concern in Important Regions
- Unexplained Observables Persist to a Remarkable Degree
- With the Present Situation

THERE IS NO SUBSTITUTE FOR EXPERIMENTAL
OBSERVABLES



P.E. Hodgson
Nuclear Physics Laboratory
Oxford, United Kingdom

Abstract:

The present status of optical model calculations of neutron scattering and interactions is reviewed, with special emphasis on more recent developments and the more promising lines of research. The use of dispersion relations to provide an extra constraint on the potential is discussed, together with their application to studies of the Fermi surface anomaly. The application of potential inversion techniques to determine the form of the potential is also considered.

1. Introduction

The neutron optical potential remains an essential tool for analyses of neutron scattering and reaction data, and continuing efforts are devoted to determining it with higher precision over a wide range of energies and nuclei. Many precise optical model analyses have been made with potentials adjusted to optimise the fits either to individual nuclei or to ranges of nuclei across the periodic table. The parameters of these potentials have been tabulated (Perey and Perey, 1974, 1976) and the results of many analyses discussed in review articles (Hodgson, 1971, 1984ab).

This work will certainly continue, and enough new analyses have been made since the last review to provide material for a new review. However it is more interesting to concentrate on work that embodies new ideas, and to try to assess their usefulness for the practical problems of understanding and describing neutron interactions.

In recent years neutron analyses have greatly increased in accuracy, and it has become clear that a simple optical model parametrisation is no longer able to give acceptable fits to the experimental data. In particular, the depth of the real potential shows a non-linear behaviour around the Fermi surface; this is often referred to as the Fermi surface anomaly. Precision analyses have also shown that it is no longer adequate to assume that the radius of the real potential is independent of neutron energy.

It is of course possible to accommodate these and other departures from the simple optical model by more complicated parametrisations, but in the absence of theoretical guidance concerning the form of the parametrisation these are inevitably arbitrary and are unlikely to be applicable outside the domain where they are fitted to experimental data. What is required is a theoretical understanding of these anomalies that gives the most appropriate form of the potential, so that when it is fitted to a restricted range of data it can be extrapolated over a wider energy range with some confidence because it has a sound physical basis.

This theoretical understanding is provided by the dispersion relations that connect the real and imaginary parts of the optical potential. These have indeed been known for some time, but it is only in recent years that the neutron data has achieved the precision that enables them to be fully exploited. Several detailed analyses have now shown that they are able to account in some detail for the apparently anomalous behaviour of some optical model parameters, and thus make possible a consistent and accurate analysis of neutron data that has a sound physical basis.

In this review we are concerned with energies up to about 50 MeV. At the higher energies in this range the analysis is straightforward since only shape elastic processes contribute. At lower energies the analysis is complicated by the presence of compound elastic processes: the cross-sections fluctuate with energy and the energy average can be calculated from statistical theory. Inevitably this reduces the accuracy attainable. At low energies rather few partial waves contribute to the scattering, and this raises the question of the adequacy of the optical model description.

A broader view of the problem of determining the low-energy neutron optical potential may be obtained by setting it within the context of the concept of the nuclear mean field that extends from negative to positive energies. This potential behaves in a continuous way over the whole energy region: the overall nearly-linear variation of the real part of the potential is the Hartree-Fock field, and its energy dependence is attributable to the use of local instead of a non-local form for the potential. At negative energies the potential is defined by the bound single-particle states. The imaginary part of the potential also varies continuously, and at negative energies is defined in terms of the energy spread of the fragmentation of the single-particle states due to the residual interactions.

The energy variation of the imaginary part of the potential is centred on the Fermi energy, and close examination of the real part shows that it departs from linearity around the Fermi energy. This is the so-called Fermi surface anomaly, which perhaps should be called the Fermi surface effect, since it is now well understood. This effect significantly alters the optical potential in the energy region about 20 MeV either side of the Fermi surface, and so is important in the energy region covered by this review.

From this broader point of view of the optical potential we can use a much wider range of data to determine the low energy neutron optical potential: not only the elastic scattering and total cross-section data in this energy region but also the data on bound single-particle states. Furthermore, the real and imaginary parts of the potential are connected by the dispersion relations, and this not only explains the Fermi surface effect but also determines the parameters of the potential with higher precision.

In Section 2 the nuclear mean field is discussed in more detail, and in the following section its detailed parametrisation is given, with particular attention to the aspects that are inconsistent with the standard parametrisation. In Section 4 the dispersion relations are described and expressed in a form suitable for the analysis of experimental data. Some results obtained by applying the dispersion relations are summarised in Section 5, and conclusions drawn concerning the form of the optical potential. In Section 6 we return to the problem of the 'fine structure' of the optical potential, and summarise the present situation. Finally in Section 7 some results obtained by applying potential inversion techniques to determine the radial form of the potential are described.

2. The Nuclear Mean Field

The one-body potential between a nucleon and a nucleus is a concept that has been extensively used to unify a wide range of phenomena in nuclear structure and nuclear reaction physics. At negative energies, the eigenvalues of the potential may be identified with the centroid energies of the bound single-particle states and at positive energies the potential gives the differential cross-sections and polarisations of nucleons scattered by nuclei.

Many studies of both bound and scattering states have enabled the parameters of the potential for a wide range of nuclei to be established with some precision. The centroid energies of the bound single-particle states can be obtained from distorted wave

analyses of the cross-sections of nucleon transfer reactions, together with the widths of the fragment distributions. These energies and widths can be described quite accurately for a range of nuclei by a real potential with parameters that depend only on the mass number and the nuclear asymmetry parameter (Millener and Hodgson, 1973; Malaguti and Hodgson, 1973). Furthermore, this potential can be used, in conjunction with single-particle occupation numbers also derived from analyses of nucleon transfer reactions, to calculate nuclear charge and matter distributions that are in good accord with the experimental data (Malaguti *et al*, 1978, 1979ab, 1982, Brown *et al* 1979, 1984; Ray and Hodgson, 1979).

This potential varies with energy in a continuous way from the negative energies appropriate to the bound states to the positive energies of the scattering states. This energy variation has been described for the real central term by Bauer *et al* (1982), and for the spin-orbit term by Cooper and Hodgson (1980). The imaginary term is included in the optical potential for scattering states in order to account for the flux removed from the elastic channel by non-elastic processes. It can also be defined for negative energies by relating it to the width of the single-particle fragment distribution.

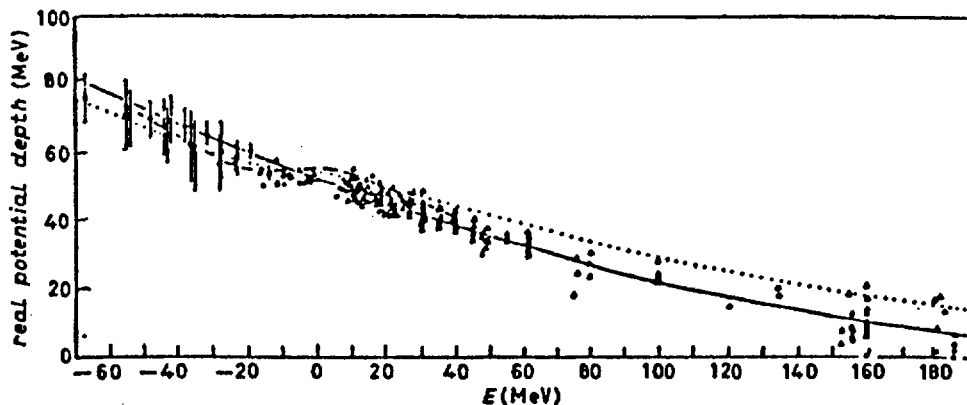
In all these analyses the real and imaginary parts of the optical potential are adjusted independently to fit the experimental data. There is however an important connection between them provided by the dispersion relations (Hodgson, 1984; Mahaux *et al* 1985), and these give an additional constraint that can be used to define the potential more precisely. It is the principal aim of this paper to describe how this can be done, and to evaluate the advantages of this method of analysis.

3. Phenomenological Characteristics of the Nucleon Optical Potential

We begin this section by summarising the overall characteristics of the nucleon optical potential, as determined by phenomenological analyses of elastic scattering and polarisations. For convenience of calculation the optical potential is written in the form

$$V(r) = V_c(r) + U f_u(r) + iW g(r) + \left(\frac{\hbar^2}{m_\pi c} \right)^2 \frac{1}{r} U_S \frac{df_s}{dr} L \cdot \sigma \quad (3.1)$$

where $V_c(r)$ is the electrostatic potential of the nucleus (included only in the proton optical potential), U , W and U_S are the real, imaginary and spin-orbit potential depths and the form factors $f_i(r) = [1 + \exp\{(r - R_i)/a_i\}]^{-1}$, $g(r) = f_W(r)$ (Saxon-Woods or volume form) or $g_s(r) = -4a_W df_W(r)/dr$ (derivative Saxon-Woods or surface form).



3.1 Depth of real central optical potential for protons as a function of proton energy, corrected for the isospin and Coulomb terms. The curves refer to the quadratic fit (full curve) and to the calculations of Brown *et al* (1979) (dotted curve) and of Mahaux and Ngô (1981) (dashed curve) (Bauer *et al*, 1982).

These form factors are no more than approximate representations of the radial variations of the potentials, and it will be shown below that there are important differences between them and the more precise forms revealed by the dispersion relations and by the potential inversion techniques.

Many analyses of experimental data have shown that the real potential depth U decreases almost linearly with nucleon energy, and in addition shows some non-linear behaviour in the region of the Fermi energy, as shown in Fig.3.1. The overall dependence can be expressed as a function of energy (Bauer *et al* 1982)

$$U = 52.4 - (0.37 \pm 0.02)E + (0.0007 \pm 0.0001)E^2 + 24\frac{N - Z}{A} + 0.4\frac{Z}{A^{1/3}}. \quad (3.2)$$

This smoothly-varying part of the potential is identified as the Hartree-Fock field, and its energy dependence is attributed to the non-locality of the potential. The anomalous behaviour in the vicinity of the Fermi surface, called the Fermi Surface Anomaly, is attributed to the effect of coupling to non-elastic channels.

The spin-orbit potential has a small energy dependence that can be represented for the whole energy range from negative to positive energies by (Cooper and Hodgson, 1980)

$$U_s = 6.5 - 0.023E \quad (3.3)$$

The energy variations of the real potential shown in Fig.3.1 can be conveniently described by an effective mass m^* defined by (Hodgson, 1983)

$$\frac{m^*}{m} = 1 + \frac{dV}{dE} \quad (3.4)$$

Since the overall energy variation (3.2) and the Fermi surface anomaly have distinct physical origins it is useful to describe them by separate effective masses \tilde{m} and \bar{m} defined respectively by

$$\frac{\tilde{m}}{m} = \left(1 - \frac{m}{k} \frac{\partial V}{\partial k}\right)^{-1} \quad \text{and} \quad \frac{\bar{m}}{m} = 1 + \frac{\partial V}{\partial E}. \quad (3.5)$$

The overall energy variation then gives

$$\frac{\tilde{m}}{m} = 0.73 + 0.0007E \quad (3.6)$$

The Fermi surface anomaly is described by an effective mass that peaks at the Fermi energy and Brown, Dehesa and Speth (1979) have proposed for the total effective mass the expression

$$\frac{m^*}{m} = 0.64 + \frac{0.36}{[1 + |E - E_F|/2\hbar\omega_0]^2} \quad (3.7)$$

where $\hbar\omega_0 = 41A^{1/3}$. The energy variation corresponding to this expression is included in Fig.3.1.

The energy dependence of the imaginary potential is more difficult to determine because the form factor has predominantly the surface form at low energies, changing continuously to the volume form at higher energies. Furthermore, the experimental data do not fix the strength of the imaginary potential as accurately as that of the real part. At low energies the energy variation of the imaginary potential determined from analyses assuming only a volume form is approximately (see Fig.5.2)

$$W = W_0(E - E_F)^2 \quad (3.8)$$

More precise optical model analyses have provided evidence that the parametrisation (3.1) is inadequate. In particular, there is evidence that the radial dependence is not adequately represented by the Saxon-Woods form (Hodgson 1984) and that if nevertheless it is constrained to have the Saxon-Woods form then the radius and diffuseness parameters vary with energy.

As an example of such work, analyses of experimental data on the elastic scattering of 30, 40 and 61.4 MeV protons by ^{208}Pb and several other nuclei by Sinha and Edwards (1970, 1971) showed that an improved fit to the differential cross-section is obtained by adding a surface-peaked potential of the Saxon-Woods derivative form to the usual Saxon-Woods potential. Initially they interpreted this additional potential as an isospin term, but this possibility was later excluded when it was found that the improvement persists in nuclei like ^{40}Ca , for which the isospin term must be zero.

Another example is provided by the work of Finlay *et al* (1985) on the scattering of 7 and 22 MeV neutrons by ^{208}Pb . Optical model analyses of the differential cross-sections gave significantly different values of the geometrical parameters at the two energies: $r_R = 1.254$, $r_I = 1.31$ fm at 7 MeV and $r_R = 1.18$, $r_I = 1.26$ fm at 22 MeV. It was found possible to fit these and other data from 0 to 24 MeV with potentials having energy-dependent geometrical parameters $r_R = 1.302 - 0.0055E$, $r_I = 1.363 - 0.0042E$, $a_I = 0.7$ and $a_R = 0.162 + 0.019$ fm. If the data are analysed with energy-independent form factor parameters the overall fits are significantly poorer, and the optimum real potential depth departs from the linear dependence at low energies. The volume integral of the real potential shows an anomalous departure from linearity with energy in the region of the Fermi Surface.

Subsequently, detailed optical model analyses of the elastic scattering of neutrons by yttrium and bismuth have also provided evidence for energy-dependent form factor parameters (Lawson, Guenther and Smith 1986, 1987).

4. The Dispersion Relations

Theoretical studies of the optical potential show that it is complex and also non-local both in space and in time. The spatial non-locality is equivalent to a momentum dependence and the temporal non-locality to an energy dependence and so we write it as $V(k, E)$. It is an analytic function of the energy and therefore satisfies the dispersion relation

$$V(k, E) = \frac{1}{2\pi i} \int_c \frac{V(k, E')}{E' - E} dE' \quad (4.1)$$

Since the potential is complex it may be separated into real and imaginary parts

$$V(k, E) = V(k, E) + iW(k, E) \quad (4.2)$$

Substituting into (4.1) and separating into real and imaginary parts gives

$$V(k, E) = \frac{1}{\pi} \int_{-\infty}^{\infty} \frac{W(k, E')}{E' - E} dE' \quad (4.3)$$

$$W(k, E) = \frac{1}{\pi} \int_{-\infty}^{\infty} \frac{V(k, E')}{E' - E} dE' \quad (4.4)$$

These dispersion relations connect the real and imaginary parts of the optical potential, and thus impose additional constraints on the phenomenological analyses.

To apply them to the analysis of experimental data, we separate the real potential into the Hartree-Fock field $V_{HF}(k)$ that depends only on the momentum and an energy-dependent part $V(E)$, giving

$$V(k, E) = V_{HF}(k) + \frac{1}{\pi} \int_{-\infty}^{\infty} \frac{W(E')}{E' - E} dE' \quad (4.5)$$

This provides the required connection between the real and imaginary parts of the phenomenological potential, and also enables us to understand the empirical energy dependence shown in Fig.3.1. The overall linear energy dependence is attributed to the Hartree-Fock field, and the 'anomalous' behaviour centred on the Fermi energy is attributed to the effect of the imaginary potential.

The practical application of the dispersion-relation (4.5) encounters the difficulty that the integral of the imaginary part of the potential extends over an infinite energy range. This may be overcome in two ways, firstly by separating the imaginary potential into two parts and secondly by using subtracted dispersion relations. These will now be discussed.

The first method depends on a separation of the imaginary potential into surface-peaked and volume components

$$W(r) = W_s(r) + W_v(r) \quad (4.6)$$

Phenomenological optical model analyses with both surface-peaked and volume imaginary potentials show that the former dominates at low energies while the latter becomes important only for energies of some tens of MeV. Each gives a contribution to the real potential of its own radial form. Since the major part of the real optical potential $V_{HF}(r)$ has the volume form $W_v(r)$ has the effect of altering its depth by a rather small amount at energies far from the Fermi energy and thus has the effect of altering the curvature of $V_{HF}(E)$.

The surface-peaked potential $W_s(r)$ however gives a small surface-peaked addition to the real potential centred at the Fermi energy, and this has the effect of increasing its radius. Since most of the phenomenological analyses are made with fixed radius R this implies a phenomenological potential of increased depth.

The second method uses subtracted dispersion relations. From (4.5) we obtain

$$V(K, E) - V(K, E_F) = \frac{(E - E_F)}{\pi i} \int_{-\infty}^{\infty} \frac{W(E')}{(E' - E)(E' - E_F)} dE' \quad (4.7)$$

This integral converges sufficiently rapidly for it to be evaluated unambiguously. It is therefore possible to use phenomenological values of $W(E)$ obtained from analyses with the volume form only. Mahaux and Ngô have divided this integral into two parts corresponding to the polarisation contributions from energies above the Fermi surface and correlation contributions from energies below the Fermi surface.

All the potentials in these dispersion relations are r -dependent, with the parametrisation described in Section 3. The phenomenological analyses however determine certain moments of the potential with greater accuracy than the individual parameters of the potential. It is thus often useful to work with dispersion relations integrated over the radial variable. Particularly useful is the volume integral per nucleon defined by

$$J_V = \frac{4\pi}{A} \int_0^{\infty} V(r)r^2 dr \quad (4.8)$$

The corresponding dispersion relation is

$$J_V(E) = J_V^{HF}(k) + \frac{1}{\pi} \int_{-\infty}^{\infty} \frac{J_W(E')}{E' - E} dE' \quad (4.9)$$

In general one can define the q^{th} moment of the potential

$$J_V^{(q)} = \frac{4\pi}{A} \int_0^{\infty} V(r)r^q dr \quad (4.10)$$

which satisfies the dispersion relation

$$J_V^{(q)}(E) = J_V^{(q)HF}(k) + \frac{1}{\pi} \int_{-\infty}^{\infty} \frac{J_W^{(q)}(E')}{E' - E} dE' \quad (4.11)$$

Subtracted dispersion relations for the integrated potentials can be defined as before.

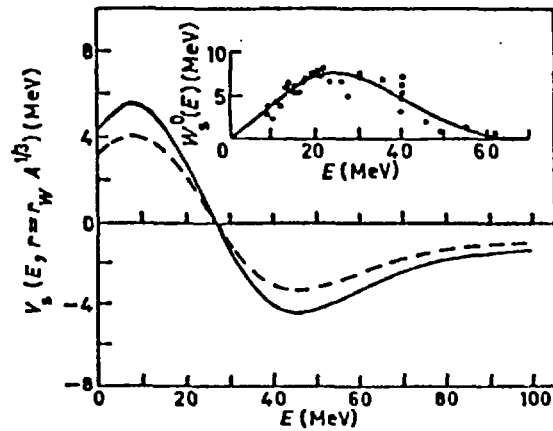
The physical reason for the Fermi potential anomaly is the coupling between the elastic and inelastic channels, which is greatest when the incident energy is comparable with the energies of the excited states. The effect of the inelastic scattering given either by the complete set of coupled equations connecting the wavefunctions in all open channels or by the imaginary potential in the simple phenomenological optical model. It is thus possible to calculate the effect on the real potential in the simple optical model of the coupling to inelastic channels by using the coupled-channels formalism to generate a differential cross-section and then fitting it with an optical potential. Several analyses made in this way have confirmed that the coupling to inelastic channels does produce changes in the real potential similar to the observed Fermi potential anomaly (Gyarmati *et al*, 1981).

5. Applications of the Dispersion Relations

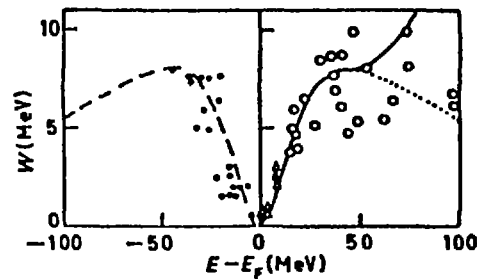
In this section we describe several applications of dispersion relations to elastic scattering data that account for the Fermi surface anomaly and also show how the optical potentials can be extrapolated from positive to negative energies.

Ahmad and Haider (1976) used the dispersion relation (4.5) to calculate the surface-peaked component of the real potential from the surface-peaked component of the imaginary potential. For this analysis, they used the potentials found by Van Oers (1971) for 10–60 MeV protons elastically scattered by ^{40}Ca . The depths of the surface-peaked potentials, together with the resulting surface-peaked real potential, is shown in Fig.5.1.

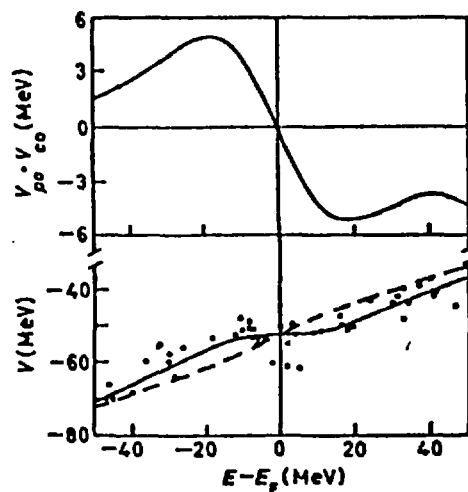
This calculation was possible because the surface-peaked imaginary potential falls to zero around 60 MeV, so that the dispersion integral converges. The analysis is however subject to the difficulty that it is not possible to separate the volume and surface-peaked components very accurately by a purely phenomenological analysis. If the imaginary potential is taken to have only the volume form, the depth may be determined more accurately, and convergence can still be obtained by using the subtracted dispersion relation (4.7). This was done by Mahaux and Ngô (1979), using the energy variation of the imaginary potential shown in Fig.5.2. The values of the strength of the imaginary potential were obtained from single-particle spreading widths for negative energies, from neutron strength functions at small positive energies and from elastic scattering data at higher energies. These data show some scatter, but at small values



5.1 The real surface-peaked component V_S of the optical potential as a function of energy for $a_w = 0.549$ (full curve) and $a_w = 0.732$ (dashed curve). The inset shows the imaginary surface-peaked potential as a function of energy obtained by Van Oers (1971) from an optical model analysis of the elastic scattering of protons by ^{40}Ca (Ahmad and Haider, 1976).



5.2 Energy dependence of the imaginary part of the optical potential for medium-light nuclei (Mahaux and Ngô, 1979).



5.3 The sum of the polarisation and correlation contributions to the real part of the optical potential, together with the total real potential as a function of energy (Mahaux and Ngô, 1979).

of $(E - E_F)$ they are consistent with the quadratic form

$$W \propto (E - E_F)^2 \quad (5.1)$$

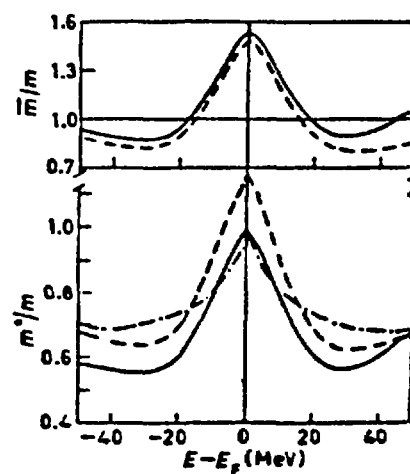
At energies more than 40 MeV above or below the Fermi surface the value of the imaginary potential is very uncertain, but use of the subtracted dispersion relation ensures that this has little effect on the calculation of the real part of the potential.

The results of this calculation are shown in Fig.5.3. In the analysis, they split the dispersion integral into two parts corresponding to the polarisation contributions from energies above the Fermi surface and the correlation contributions from energies below the Fermi surface. When these are added together it is found that the result is quite similar for energies less than 40 MeV to that obtained by Ahmad and Haider (noting the difference in sign between the definitions of the real potential). The energy variation of the effective mass corresponding to the polarisation and correlation contributions were obtained using (4.7) and are shown in Fig.5.4. Combining this with the value of \bar{m} obtained from the overall energy variation gives the results for m^* also included in this figure. Similar results for the energy variation of the effective mass have also been obtained from nuclear structure calculations (Bortignon *et al*, 1982).

This peaking of the effective mass in the region of the Fermi surface describes the Fermi surface anomaly and enables the energy variation of the real part of the potential to be calculated. The results are shown in Figs.3.1 and 5.3.

The dispersion relations can also be used to extrapolate the optical potential from positive to negative energies. Smith, Guenther and Lawson (1985) has done this for the potential describing the elastic scattering of neutrons by ^{93}Nb using the dispersion relation (4.9) for the volume integrals of the potential. Phenomenological optical model analyses of the differential cross-sections for the elastic-scattering of 2–14 MeV neutrons by ^{93}Nb gave potentials with volume integrals with the energy variations

$$\left. \begin{aligned} J_V^{(E)} &= 445 - 2.4E \\ J_W^{(E)} &= 52 + 3E \end{aligned} \right\} 0 \leq E \leq 14 \text{ MeV} \quad (5.2)$$



5.4 The energy variation of the effective masses \bar{m}/m and m^*/m around the Fermi energy obtained using the dispersion relation (3.7) from the energy-dependent imaginary potential shown in Fig.5.2 (full curve). The dashed curve corresponds to the parametrisation (2.8) (Mahaux and Ngô, 1979).

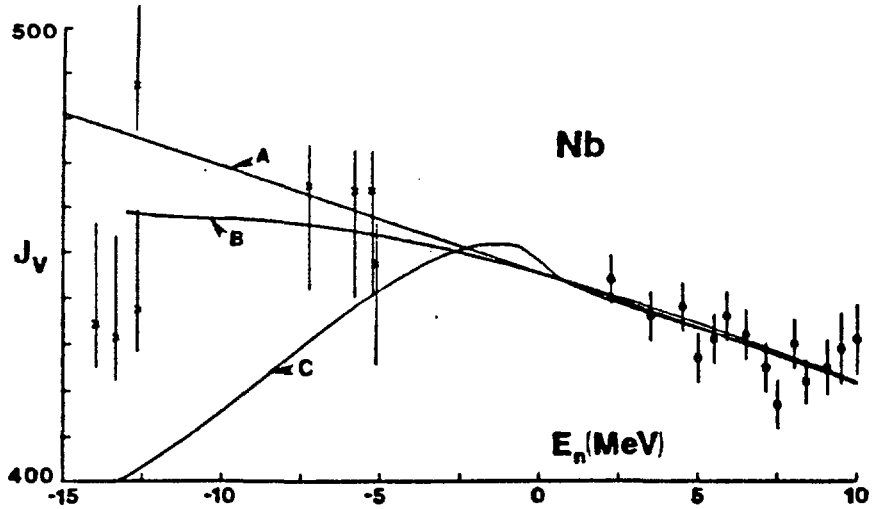
To apply the dispersion relation the energy variation of J_W outside this range was described by the expressions

$$J_W^{(E)} = 102 - 0.6E \quad \text{for } E > 14 \text{ MeV}$$

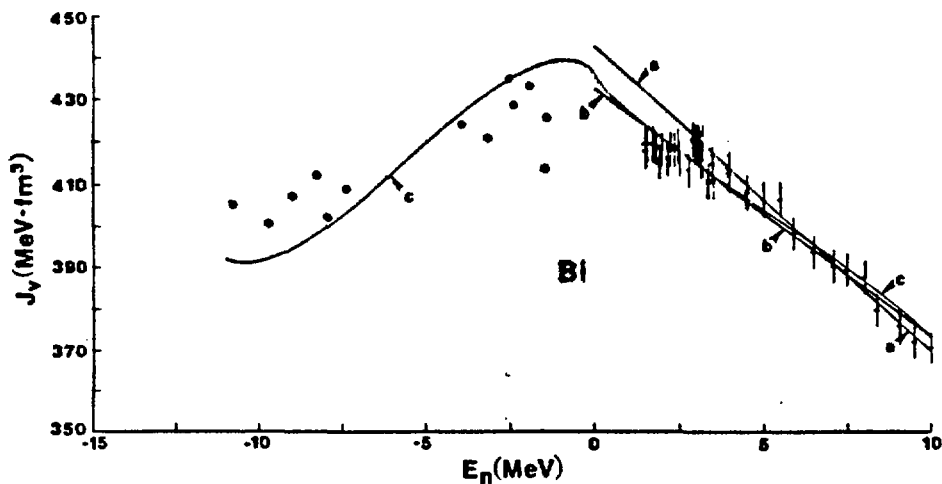
and

$$J_W^{(E)} = 0.52(E + 10)^2 \quad \text{for } -20 \leq E \leq 0 \text{ MeV}$$
(5.3)

This enabled the energy variation of $J_V(E)$ to be calculated for negative energies, and the result is shown in Fig.5.5. At negative energies it can be compared with the integrals of the potentials corresponding to discrete bound states. Subsequently similar



5.5 Volume integral per nucleon of the real neutron potential for ^{93}Nb for bound and unbound energies. The points at positive energies are obtained from optical model analyses of elastic scattering data and those at negative energies from the binding energies of particle and hole state. The curves show: A, a linear fit to the scattering data; B, the energy variation calculated from the expression of Brown *et al* and C, calculated from a dispersion relation formula (Smith, Guenther and Lawson 1985).



5.6 Volume integral per nucleon of the real neutron potential for ^{209}Bi for bound and unbound energies. The points at positive energies are obtained from optical model analyses of elastic scattering data and those at negative energies from the binding energies of particle and hole states. The curves show: a, a linear fit to the scattering data from 4.5 to 10 MeV; b, a linear fit to all scattering data; c, calculated from a dispersion relation formula (Lawson, Guenther and Smith, 1987).

analyses have been made for the potential describing the scattering of neutrons by yttrium and bismuth (Lawson *et al* 1986, 1987).

The results for bismuth are of particular interest because of the relatively large number of single-particle states that can be used to determine the potential at negative energies. As shown in Fig.5.6, the curve obtained using the dispersion relations fits the overall trend of this data quite well.

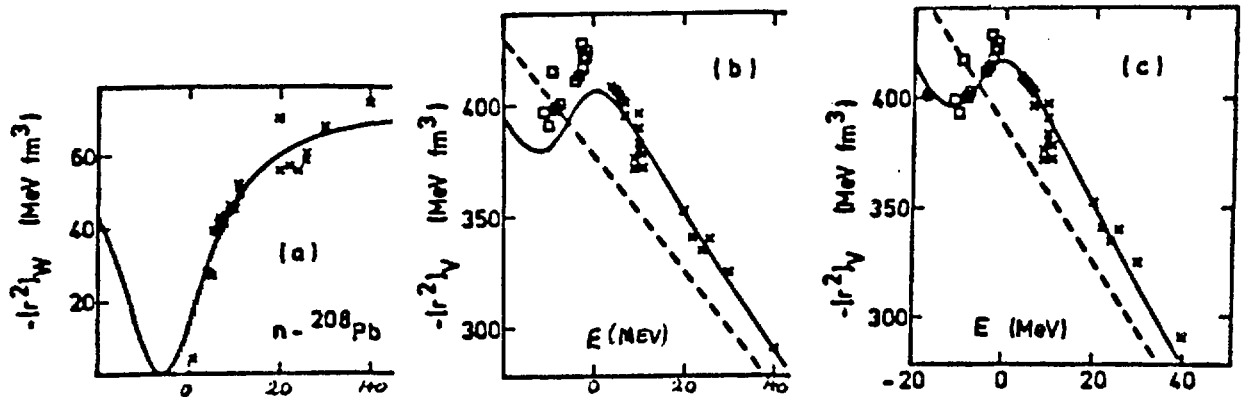
The dispersion relations (4.11) for the moments of the potential have been used by Mahaux and Sartor to extrapolate to negative energies the potential for neutrons scattered by ^{208}Pb . They calculated the moments corresponding to $q = 0.8, 2$ and 4 and noted that these moments suffice to define the three parameters U, R and a of the real part of the optical potential. To apply the dispersion relations, they represent the energy variation of the moments of the imaginary potential by the expression due to Brown and Rho (1981)

$$J_W^{(q)}(E) = -W_q \frac{(E - E_F)^2}{(E - E_F)^2 + \sigma_q^2} \quad (5.4)$$

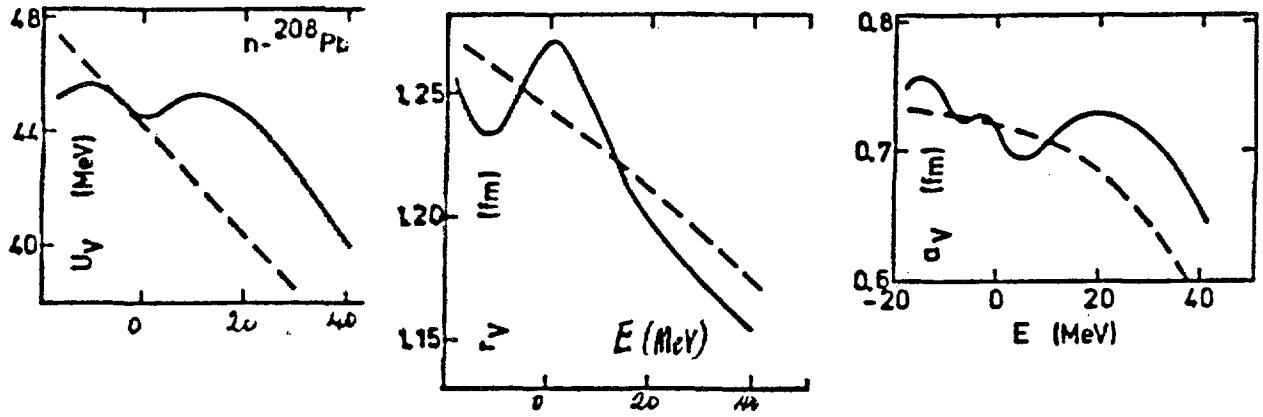
This is compared with the experimental data for $q = 2$ in Fig.5.7. They also assumed that the moments of the Hartree-Fock field have a linear energy dependence given by

$$J_V^{HF(q)}(E) = B_q + C_q E \quad (5.5)$$

These two expressions were then inserted in the dispersion relation (4.11) and the parameters B_q and C_q adjusted to optimise the fit to the data, with the result for $q = 2$ shown in Fig.5.7b. This clearly shows the anomaly in the region of the Fermi surface. The extrapolation to negative energies can be compared with the potentials



5.7 The energy dependence of the volume integrals of (a) the imaginary and (b) and (c) the real parts of the optical potential for neutrons on ^{208}Pb . The crosses are empirical values from phenomenological optical potentials. The curve in (a) is a least squares fit using the parametrisation (5.4). The curves in (b) are the calculated values of $J_V^{(2)HF} = B_2 + C_2 E$ (dashed line) and of $J_V^{(2)}$ (solid curve) obtained by determining B_2 and C_2 by a least squares fit to the scattering data (crosses). The open squares show the experimental values of $J_V^{(2)}(E_j)$ for the bound single-particle states obtained by adjusting the Saxon-Woods potential depths $U_V(E_j)$ using the shape parameters $R_V(E_j)$ and $a_V(E_j)$ obtained from the extrapolated values of $J_V^{(q)}(E_j)$ for $q = 0.8, 2$ and 4 . The curves in (c) are similar except that the open squares are included in the data set used to determine B_q and C_q . The full dot gives the result for the $h_{11/2}$ state (Mahaux and Sartor, 1986).



5.8 The energy dependence of the parameters of the real part of the Saxon-Woods optical potential. The dashed curves were obtained from the moments $J_{HF}^{(q)HF}(E)$ of the Hartree-Fock field for $q = 0.8, 2$ and 4 . The solid curves were obtained from the moments $J_V^{(q)}(E)$ of the real part of the complete potential (Mahaux and Sartor, 1986).

corresponding to the neutron bound states, and shows qualitative agreement. The fit to these states was improved by adding a spin-orbit term to the potential to allow the energies of these bound states to be calculated and then repeating the fitting procedure including both the scattering and the bound state data. This gives the result shown in Fig.5.7c, which is in excellent agreement with the data. The curve was further extrapolated to the deeply bound $1h_{11/2}$ state at -15.9 MeV and good agreement found.

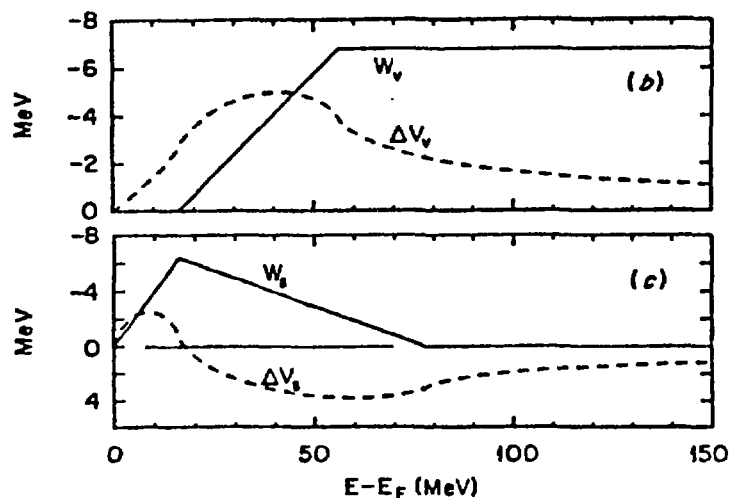
The resulting energy variations of the three moments of the potential enable the parameters of the potential to be determined as a function of energy, and these are shown in Fig.5.8. The dashed lines correspond to the Hartree-Fock potential alone and the full lines show the effect of adding the dispersive correction. This figure shows the limitations of the Saxon-Woods parametrisation of the optical potential.

A particularly detailed analysis of the interaction of neutrons with ^{208}Pb from -20 to $+165$ MeV has been carried out by Johnson, Horen and Mahaux (1987) making full use of the dispersion relations to constrain the values of the parameters of the potential. The Hartree-Fock field was described by a Saxon-Woods potential with parameters $V_H = 46.4$ MeV, $r_0 = 1.24$ fm and $a = 0.68$ fm at the Fermi energy (-6 MeV) with an energy dependence $\exp(-\alpha E)$, where $\alpha = (m/2\hbar^2)\beta^2$ and $\beta = 0.74$ fm; this gives

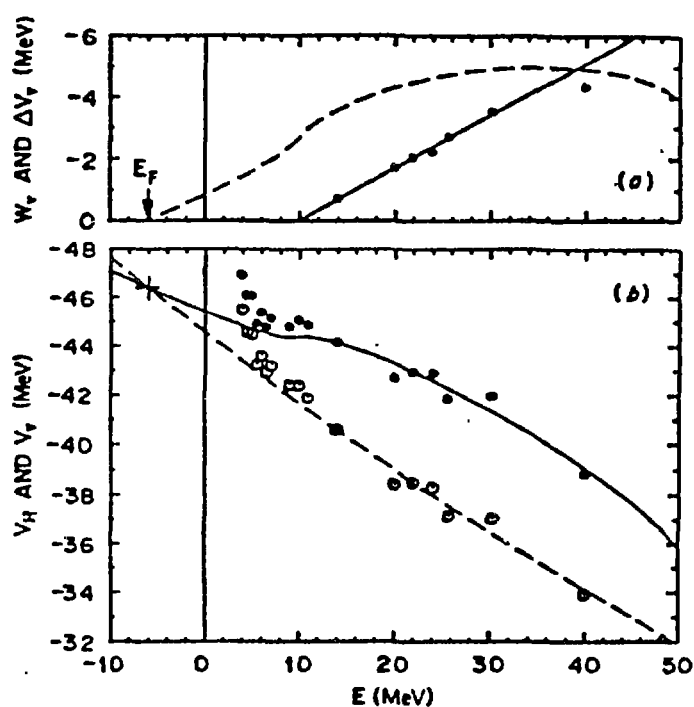
$$V_H(E) = 46.4 - 0.31(E - E_F) \quad (5.6)$$

in the vicinity of the Fermi surface.

The imaginary part of the optical potential was assumed to be symmetric about the Fermi energy and to consist of surface-peaked and volume components with depths represented by the linear segments shown in Fig.5.9. The parameters defining these segments and the associated energy-independent radius and diffuseness parameters were determined by analysis of the experimental data. The dispersive corrections to the real part of the potential obtained by inserting these surface-peaked and volume imaginary potentials in the dispersion relation (4.3) are also shown in Fig.5.9. The optimum values of the real and imaginary potential depths obtained from this parametrisation are compared with the best fit values at each energy in Figs.5.10 and 5.11. Throughout this analysis the spin-orbit potential was fixed to the values $U_s = 5.75$ MeV, $r_s = 1.105$ fm, $a_s = 0.50$ fm.

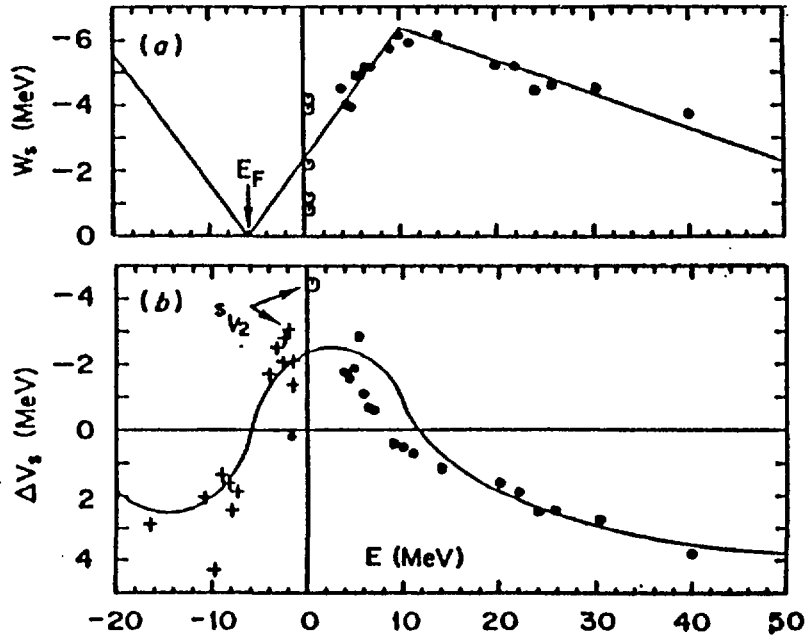


5.9 The energy dependence of the depths of the volume and surface peaked components of the imaginary optical potential (full lines) together with the corresponding corrections to the real optical potential obtained using the dispersion relations (dashed curves) (Johnson *et al* 1987).



5.10 (a) The depth of the volume imaginary potential (full line) compared with optical model analyses, together with the corresponding correction to the real potential obtained from the dispersion relation (dashed curve)
 (b) The depth of the Hartree-Fock potential (dashed curve) and the total depth obtained by adding the dispersion correction (full curve) (Johnson *et al*, 1987).

This potential gives an excellent fit to the differential and total cross-sections and analysing powers for neutron scattering by ^{208}Pb , and also to the eigenvalues of the bound single-particle states and the values of the single-particle wavefunctions at large distances as determined from sub-Coulomb pick-up experiments. Furthermore, it automatically explains the special features of the potential that were found in previous optical model analyses, in particular the near-independence of the real potential depth on energy from 4 to about 20 MeV and the decrease with energy of the radius of the



5.11 (a) The depth of the surface imaginary potential (full line) compared with the results of optical model analyses.
 (b) The depth of the dispersive correction to the real potential compared with the results of optical model analyses (solid points) and values obtained by the energies of bound single-particle states (crosses) (Johnson *et al*, 1987).

potential in the same energy region. Additional calculations showed that the fit to the data may be still further improved by allowing the potentials to depend on orbital angular momentum.

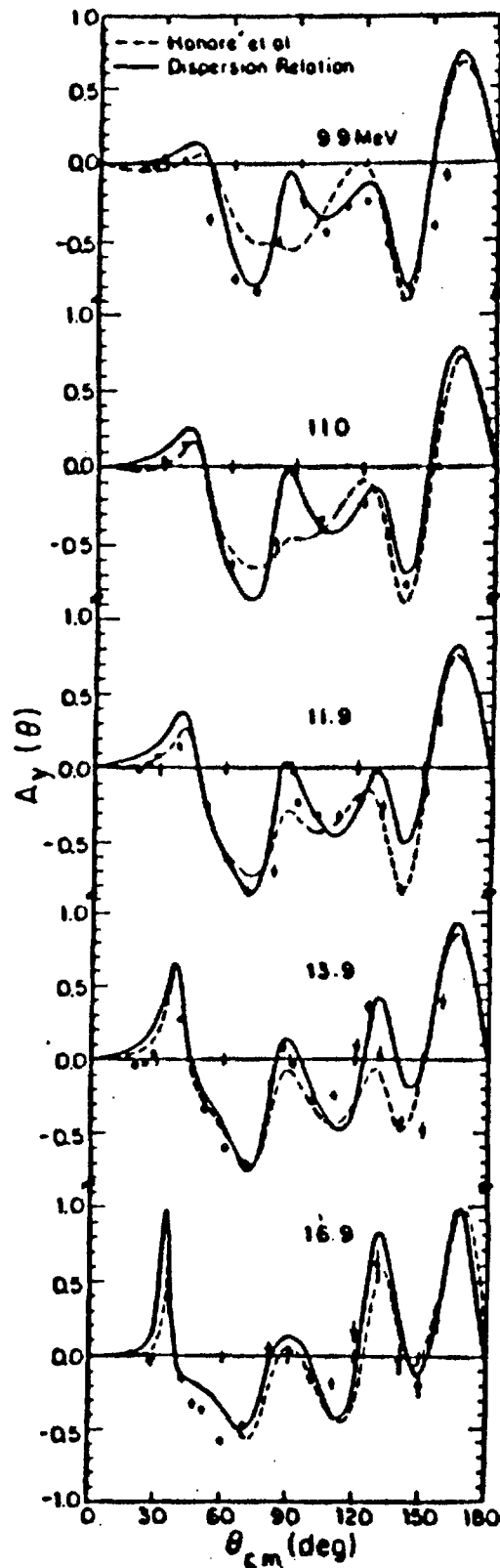
Another indication of the usefulness of the dispersion relations is provided by the analysis of the inelastic scattering of 5–11 MeV neutrons with excitation of the 3^- state in ^{208}Pb recently made by Cheema and Finlay (1987). Previous analyses gave a sharp increase of the deformation length for energies less than 11 MeV. Cheema and Finlay repeated the analysis using potentials and form factors that include the dispersion correction and found that the deformation lengths at low energies were reduced to values consistent with those obtained from data at higher energies.

Further support for the usefulness of the dispersion relations is provided by the analysis of the analysing power for the elastic scattering of 9.9 to 16.9 MeV neutrons by ^{40}Ca recently carried out by Delaroche and Tornow (1987). Previous analyses of the differential cross-sections and analysing powers required a small imaginary spin-orbit potential and even then the fits to the analysing powers were not satisfactory (Honoré *et al*, 1986). However when the analysis was repeated using potentials satisfying the dispersion relations a much improved fit to the analysing powers was obtained without an imaginary spin-orbit term, as shown in Fig.5.12.

6. The Fine Structure of the Optical Potential

Accurate optical model analyses of the differential cross-sections for the elastic scattering of protons by a series of medium weight nuclei have shown that the potential depth depends not only on the nuclear asymmetry parameter $\alpha = (N - Z)/A$ but also on the isospin $T_Z = \frac{1}{2}(N - Z)$ (Perey and Perey, 1968; Novo *et al*, 1981).

The available neutron data are not yet sufficiently accurate to show this effect but as it is very likely to be present it is appropriate to consider it here.



5.12 Analysing powers for the elastic scattering of 9.9 to 16.9 MeV neutrons by ^{46}Ca compared with optical model calculations with an imaginary spin-orbit term (dashed curves) and without an imaginary spin-orbit term but using dispersion-relation potentials (full curves) (Delaroche and Tornow 1987).

The fine structure in proton optical potentials shown by the 11 MeV data of Perey and Pery can be fitted by a variety of phenomenological expressions (Hodgson, 1970, 1985) of the form

$$V_p = V_0 - \gamma E + \beta A^\alpha + \epsilon V_1 + \gamma V_c \quad (6.1)$$

where $\epsilon = (N \sim Z)/A$ is the nuclear asymmetry parameter, V_1 is the isovector potential and γV_c the Coulomb correction term. Equally good fits to the data can be obtained with the exponent $\alpha = -\frac{1}{3}, \frac{1}{3}$ or 1, with corresponding optimised values of β . The dependence of the potential on the mass number is indeed suggested by the folding model.

A more fundamental explanation of the fine structure was provided by Yang and Rapaport (1986), who showed that it essentially disappears if the energy is measured from the Fermi surface. This gives

$$V_p = V_0 - \gamma(E - E_F) + \epsilon V_1 + \gamma V_c \quad (6.2)$$

It is notable that in their analysis they used values of $\gamma = 0.78$ at 11 MeV and $\gamma = 0.60$ at 14 MeV obtained from the analysis of Perey (1963). These are much higher than the value $\gamma = 0.3$ corresponding to the Hartree-Fock field and are a consequence of the additional term introduced by the coupling to higher states and given by the dispersion relation.

More recently, a very extensive global optical model analysis of proton and neutron elastic scattering data has been made by Varner *et al* (1987). They used a potential with a radius parameter

$$R = r_{00} + r_0 A^{1/3} \quad (6.3)$$

instead of the usual $R = r_0 A^{1/3}$. Their global potential fits the data very well, and thus accounts for the fine structure. The reason for this is probably that the more flexible parametrisation (6.3) of the radius parameter is essentially equivalent to the addition of the A-dependent term in (6.1), through the well-known VR^2 ambiguity. It may however be suggested that an equally good, and perhaps even better fit to the data would be obtained by measuring the energies from the Fermi surface and using the simpler parametrisation of the radius.

At higher energies, the 65 MeV data of Noro *et al* has been fitted by Haider *et al* (1984) using potentials obtained from Brueckner theory nuclear matter calculations. It remains to be shown that it can also be understood using the model of Yang and Rapaport, using the lower value of γ appropriate to the Hartree-Fock field.

7. Potential Inversion

The application of the dispersion relations as described in the previous sections shows how the Fermi potential anomaly can be understood as the addition of a surface-peaked imaginary term to the underlying volume term in the real part of the potential. All this work is carried out in the framework of the Saxon-Woods and derivative Saxon-Woods parametrisation of the real and imaginary parts of the potential. Since we are now looking at relatively fine details of the potential it may be asked whether this parametrisation is sufficiently accurate for the purposes. This question is given added weight by the analyses at higher energies that certainly show that the Saxon-Woods parametrisation of the real potential is inadequate.

It thus becomes important to see whether the Saxon-Woods potential is really satisfactory at low energies, and if not whether it can be improved. This can be done

if the potential could be determined from the experimental data, without the use of standard analytical form factors. This is the classical potential inversion problem, to which much attention has been devoted over the years.

Potential inversion proceeds through the intermediate stage of the phase shifts or their equivalent scattering matrix elements S_L . The differential scattering cross-sections and polarisations can be expressed by simple analytical formulae in terms of the scattering matrix elements. It is thus relatively easy to obtain the matrix elements corresponding to a particular set of experimental data, providing it is sufficiently accurate. If it is not sufficiently accurate, there may be distinct sets of matrix elements that give equally good fits to the same set of data. The meaning of 'sufficiently accurate' can only be found in each case by detailed numerical analysis. Iterative methods have been devised to obtain the matrix elements from the data, using as starting values those obtained from a phenomenological optical model analysis.

The problem is then to determine the potential from the scattering matrix elements. There are very general theorems that enable the potential to be reconstructed from a knowledge of the matrix elements at all energies. What is needed, however, is a practical method of obtaining the potential from data at a limited set of energies, subject to some restrictions concerning the form of the potential. In general, the potential is highly non-local and dependent on the orbital angular momentum, and a set of data restricted to one or a few energies is certainly insufficient to determine all these features. It is thus necessary to restrict the potential to a form that is sufficiently flexible to explore the inadequacies of the Saxon-Woods parametrisation and yet not so general that it cannot be determined with sufficient accuracy. This may be achieved by allowing a general radial dependence, but no non-locality, and in some cases by also allowing a parametrised angular momentum dependence.

A practical technique for potential inversion has been developed in recent years by Mackintosh and colleagues (Mackintosh 1979; Mackintosh and Kobos 1976, 1979; Ioannides and Mackintosh 1985, 1986, Mackintosh and Ioannides 1985). Their iterative perturbative procedure is based on the observation that the response of the scattering matrix elements S_L to perturbations in the optical potential are generally quite linear. The method begins with a reference potential $V_0(r)$ that can be the best phenomenological potential that determines a set of $S_L^{(0)}$ that are good approximations to the known accurate S_L obtained from the data. Next one selects a set of linearly independent potential perturbations $U_i(r)$ that enable the potential to be adjusted in a systematic and comprehensive way. For each of these the response $\Delta S_L^{(i)}$ of the S_L can be determined

$$S_L^{(1)} = S_L^{(0)} + \Delta S_L^{(i)} \quad (7.1)$$

Then we require that

$$S_L = S_L^{(0)} + \sum_i a_i \Delta S_L^{(i)} \quad (7.2)$$

Solution of this set of equations for the a_i gives the required potential

$$V(r) = V_0(r) + \sum_i a_i U_i(r) \quad (7.3)$$

Since the relation (7.2) is only approximately linear, the calculation must be iterated to convergence.

The practical details of this calculation, in particular the choice of basis functions, can only be studied numerically, and this gives information on the speed of convergence and the reliability of the potential obtained. Many such calculations have now been

made by Mackintosh and colleagues, and as a result the iterative-perturbative procedure has been developed so that it can give reliable information on the potential for a variety of interactions.

In the present context we are primarily interested in whether the potential inversion method has produced any results relevant to the dispersion relations analysis of elastic scattering. In a recent survey Mackintosh and Ioannides (1985) remark that one limitation of their method is that it is unreliable at low energies, that is about 25 MeV for protons. Essentially this is because the small number of partial waves at these energies implies that the system is not sufficiently determined. The choice of basis functions is then critical and makes it difficult to establish a unique potential. This is a severe limitation in the present context, as we are mainly interested in lower energies. Nevertheless, there may still be relevant results that have been obtained by the potential inversion method.

When applied to accurate nucleon elastic scattering data, phenomenological analyses give very good overall fits but there remain significant deviations that correspond to quite high values of χ^2 . These deviations certainly indicate inadequacies in the form of the potential used. Studies using the potential inversion method have now shown that precise fits to the data can be obtained by using either a L -dependent potential or one that oscillates radially (Kobos and Mackintosh, 1979). This has been done by inverting the S_L obtained from L -dependent potentials. Inversion of the S_L obtained from a L -dependent potential of the Majorana form $V(r)(1 + C(-)^L)$ gave potentials with the same volume integral as $V(r)$. Thus knowledge of the volume integral gives no information about possible L -dependence of the potential.

More relevant to the dispersion relations are the results of applying potential inversion to elastic and inelastic scattering simultaneously. As has been remarked already the physical origin of the Fermi surface anomaly is the coupling to inelastic channels; this coupling increases the imaginary part of the potential and thus affects the real part in a way that can be calculated using the dispersion relations. The coupled-channels formalism enables this to be studied explicitly. These coupled equations contain the so-called 'bare' potential and the equations themselves contain the coupling terms. If this is replaced by the single equation for the elastic channel alone, the optical potential now has to include implicitly the effects of the coupling. The relation between the 'bare' and 'dressed' potentials can be studied by finding the potentials in the two cases that give the same scattering matrix elements, and this can be done by the potential inversion method.

These calculations have been done both for inelastic scattering and for transfer reaction channels. As an example, Ioannides and Mackintosh have analysed the elastic and inelastic scattering of 104 MeV alpha-particles by ^{20}Ne , taking into account the coupling to the 2^+ and 4^+ excited states. They found that the volume integral of the real potential is $J_R = 367.5 \text{ MeV fm}^3$ for the bare potential and 346.2 MeV fm^3 when the coupling to the excited states is included. This is just the enhancement of the potential that has been found phenomenologically and accounted for by the dispersion relation analysis. Subsequent calculations showed similar effects on proton potentials due to the coupling to pickup channels.

Acknowledgments

This review was finalised following discussions with Professors R.L. Walter and W. Tornow (Duke University), W.J. Thompson (University of North Carolina), B.A. Brown (Michigan State University) and R.W. Finlay (Ohio University) and I am grateful to them all for providing me with the opportunity to visit their universities, for their detailed comments and for kindly permitting me to quote the results of their unpublished work. I also acknowledge gratefully the receipt of unpublished work by C.H. Johnson, D.J. Horen and C. Mahaux, and by R.D. Lawson, P.T. Guenther and A.B. Smith.

References

- Ahmad I and Haider W, 1976 *J. Phys.* **G2** L157
- Bauer M, Hernandez-Saldana E, Hodgson P E and Quintanilla J, 1982 *J. Phys.* **G3** 525
- Bortignon P F, Broglia R A, Dasso C H and Fu D-J, 1982 *Phys. Lett.* **B108** 247
- Brown B A, Bronk C R and Hodgson P E, 1984 *J. Phys.* **G10** 1683
- Brown B A, Massen S E and Hodgson P E, 1979 *Phys. Lett.* **85B** 167
- Brown G E, Dehesa J S and Speth J, 1979 *Nucl. Phys.* **A330** 290
- Brown G E and Rho M, 1981 *Nucl. Phys.* **A372** 397
- Cheema T S and Finlay R W, 1987 Proceedings of the Kiev Conference
- Cooper S G and Hodgson P E, 1980 *J. Phys.* **G6** L21
- Delaroche J P and Tornow W, 1987 *Phys. Lett.* (In press)
- Finlay R W, Annand J R M, Petler J R and Dietrich F S, 1985 *Phys. Lett.* **155B** 313; 1987 Private communication
- Finlay R W, 1987 Proceedings of the Kiev Conference
- Gyarmati B, Lovas R G, Vertse T and Hodgson P E, 1981 *J. Phys.* **G7** L209
- Haider W, Kobos A M, Rook J R and Pal K F, 1984 *Nucl. Phys.* **A419** 521
- Hodgson P E, 1970 *Nucl. Phys.* **A150** 1; 1983 *Contemp. Phys.* **24** 491; 1984a *Nuovo Cim.* **81A** 250; 1984b *Rep. Prog. Phys.* **47** 613; 1985 Neutron-nucleus Collisions. Ed. J.Rapaport, R.W.Finlay, S.M.Grimes and F.S.Dietrich. *AIP Conf. Proc.* No.124 (New York) 1
- Honoré G M, Tornow W, Howell C R, Pedroni R S, Byrd R C, Walter R L and Delaroche J P, 1986 *Phys. Rev.* **C33** 1129
- Ioannides A A and Mackintosh R S, 1985 *Phys. Lett.* **161B** 43; 1985 *Nucl. Phys.* **A438** 354; 1986 *Phys. Lett.* **169B** 113
- Johnson C H, Horen D J and Mahaux C, 1987 *Phys. Rev.* **C36** 2252
- Kobos A M and Mackintosh R S, 1979 *Ann. Phys. (NY)* **123** 359
- Lawson R D, Guenther P T and Smith A B, 1986 *Phys. Rev.* **C34** 1599; 1987 *Phys. Rev.* (In Press)
- Mackintosh R S, 1979 *J. Phys.* **G5** 1587
- Mackintosh R S and Ioannides A A, 1985 International Workshop on Advanced Methods in the Analysis of Nuclear Scattering Data, Berlin June 18-20
- Mackintosh R S, Ioannides A A and Thompson I J, 1986 *Phys. Lett.* **B178** 1
- Mackintosh R S and Kobos A M, 1976 *Phys. Lett.* **B62** 127; 1979 *J. Phys.* **G5** 359

- Mahaux C, Bortignon P F, Broglia R A and Dasso C H, 1985 *Phys. Rep.* **120** 1
- Mahaux C and Ngô H, 1979 *Phys. Lett.* **B100** 285
- Mahaux C, Ngô H and Satchler G R, 1987 *Nucl. Phys.* **A**
- Mahaux C and Sartor R, 1986 *Phys. Rev. Lett.* **57** 3013
- Malaguti F and Hodgson P E, 1973 *Nucl. Phys.* **A215** 243
- Malaguti F, Uguzzoni A, Verondini E and Hodgson P E, 1978 *Nucl. Phys.* **A297** 287;
1979a *Nuovo Cim.* **49A** 412; 1979b *Nuovo Cim.* **53A** 1; 1982 *Revista Nuovo Cim.* **5** 1
- Millener J and Hodgson P E, 1973 *Nucl. Phys.* **A209** 59
- Noro T, Sakaguchi H, Nakamura M, Hatamaka K, Ohtani F, Sakamoto H and Kobayashi S, 1981 *Nucl. Phys.* **A366** 189
- Perey C M and Perey F G, 1986 *Phys. Lett.* **26B** 123; 1974 *Atom. Data Nucl. Data Tables* **13** 293; 1976 *Ibid* **17** 1
- Ray L and Hodgson P E, 1979 *Phys. Rev.* **C20** 2403
- Sinha B C and Edwards V R W, 1970 *Phys. Lett.* **B31** 273; 1971 *Ibid* **B5** 391
- Smith A B, Guenther P T and Lawson R D 1985, *ANL/NOM-91*
- Van Oers W T H, 1971 *Phys. Rev.* **C3** 1550
- Varner R L, Clegg T B, McAbee T L and Thompson W J, 1987 *Phys. Lett* **185** 6
- Yang Y and Rapaport J, 1986 *Nucl. Phys.* **A454** 359

CONSISTENT SYSTEMATICS OF NUCLEAR LEVEL DENSITIES
FOR MEAN AND HEAVY NUCLEI

O.T. Grudzevich, A.V. Ignatyuk, V.I. Plyaskin
Institute of Physics and Power Engineering, Obninsk, USSR

Abstract: The systematics of the experimental data on the density of neutron resonances and low-lying levels is considered taking into account of the vibrational increase of the level density together with the shell and superconductive effects.

The density of excited level is the most important characteristic of the statistical description of different processes related to decay of a compound nucleus. The widely used Fermi gas model /1,2/ does not allow to describe consistently the existed experimental data on the statistical properties of nuclei because its relations do not take into account ^{the} significant shell inhomogeneities in the spectrum of single-particle levels, the correlation effects of the superconducting type and the coherent effects of a collective nature. The rigorous microscopic methods of analysis of these effects ^{are} prove to be very timeconsuming and that strongly restricts their practical application/3,4/. It is therefore important to look for a description of the level density which will take into account to the necessary extent the main ideas of the theory about the structure of highly excited nuclei, while remaining sufficiently simple and convenient for practical usage. For heavy nuclei with $A \geq 150$ where the rotational effects play essential role, the consistent phenomenological description of the nuclear level densities was considered in Ref./5/. In present work we want to expand this approach on more light nuclei in which the collective increase of level density is associated with the vibrational excitations.

Let us discuss shortly the main components of the consistent description of the nuclear level density. The influence of the pairing effects of the superconducting type on the nuclear properties can be characterised by the correlation function Δ_0 which directly defines the even-odd difference of nuclear masses and the gap $2\Delta_0$ in the spectrum of quasi-particle excitation of even-even nuclei. The correlation function is connected ^{with} the critical temperature $t_{cr} = 0,567 \Delta_0$ of the phase transition from the superconducting state to the normal state and

with the critical excitation energy

$$U_{cr} = 0,472 a_{cr} \Delta_0^2 - n \Delta_0, \quad (1)$$

where $n = 0, 1$ and 2 for even-even, odd and odd-odd nuclei. Above U_{cr} the level density and other statistical characteristics of a nucleus can be described by the relations of the Fermi-gas model with the effective excitation energy

$$U^* = U - 0,152 a_{cr} \Delta_0^2 + n \Delta_0. \quad (2)$$

Below the phase transition point the relations for the thermodynamical functions are more complicated, but the simple parametrisation of these functions suitable for the practical calculations is given in Ref. /5,6/. In these works there are also the discussions of the differences of the level densities in superfluid nuclear model and the Fermi gas model.

The shell inhomogeneities in the single-particle spectrum lead to a certain dependence of the level density parameter $a(U)$ on the excitation energy. However the shell effects become weaker with the increase of the excitation energy and at high energies the level density parameter will be defined by the asymptotic value

$$\tilde{a} = \alpha A + \beta A^{2/3}. \quad (3)$$

For phenomenological description of the energy dependence of this parameter we can use the relation

$$a(U, Z, A) = \begin{cases} \tilde{a} \{1 + \delta \tilde{z}_0(Z, A) f(U^*/U^*)\} & \text{for } U \geq U_{cr} \\ a_{cr}(U_{cr}, Z, A) & \text{for } U < U_{cr}, \end{cases} \quad (4)$$

where $\delta \tilde{z}_0$ is the shell correction in the nuclear binding energies /7/ and $f(U) = 1 - \exp(-\gamma U)$ is a "universal" function defining the energy behaviour of the shell effects. We used the same values of parameters as in Ref. /5/ (in units of MeV^{-1}): $\alpha = .0730$, $\beta = .1147$ and $\gamma = .40 / A^{1/3}$.

When the collective effects are taken into account the level density of quase-particle excitations must be multiplied by the coefficient of the vibrational increase of the level density

$$K_{\text{vibr}} = \exp(\delta S - \delta U/t), \quad (5)$$

where δS and δU are changes of the entropy and the excitation energy arising as the result of addition of the collective modes in the heated nucleus with the temperature t .

These functions are defined by the relations:

$$\delta S = \sum_i (2\lambda_i + 1) [(1 + \bar{n}_i) \ln(1 + \bar{n}_i) - \bar{n}_i \ln \bar{n}_i], \quad \delta U = \sum_i (2\lambda_i + 1) \omega_i \bar{n}_i, \quad (6)$$

where ω_i are energies of the vibrational excitations,

λ_i are degrees of degeneracy of them and \bar{n}_i are mean occupation numbers. If we use the relations of an ideal Bose-

gas for occupation numbers then Exp. (5) has a meaning of the adiabatic addition of the vibrational excitations to all possible quasi-particle excitations of the nucleus / 9 /.

For nonideal Bose-excitations the occupation numbers can be defined as following

$$\bar{n}_i = (2\pi)^{-1} \int_{-\infty}^{\infty} d\omega \gamma_i(\omega) (e^{\omega/t} - 1)^{-1} \{ [\omega_i + \delta_i - \omega]^2 + \gamma_i^2(\omega)/4 \}^{-1/2} \quad (7)$$

where δ_i is energy shift and γ_i is damping width of the vibrational excitations. These values depend both on the energy ω_i and the integrate variable ω , so for the definition of them it is necessary to solve correctly the complicated many body task of interacting Bose and Fermi-excitations. We did not analyse such task but only took the simplest approximation for the occupation numbers

$$\bar{n}_i = e^{-\gamma_i/2\omega_i} (e^{\omega_i/t} - 1)^{-1} \quad (8)$$

This approximation gives the relations of an ideal Bose-gas for $\gamma_i \rightarrow 0$ and provides necessary decrease of the coefficient K_{vibr} for increasing γ_i .

We can expect that the damping of the vibrational excitations in nuclei is similar to the damping of the zero-sound in the Fermi-liquid theory which is described by the relation

$$\gamma_i = c (\omega_i^2 + 4\pi^2 t^2) \quad (9)$$

From the observed spreading widths of the giant isoscalar quadrupole resonance it is possible to obtain the rough estimation of the constant $C = 0.05 A^{1/3} \text{ MeV}^{-1}$. The temperature dependence both of the occupation numbers and the coefficients which obtained from the considered relations (5-8) are shown on the Fig.1. The behaviour of the same functions in the adiabatic limit is shown also.

In calculations of the level densities we used the experimental values of the energies ω_{2+} of the first 2^+ - levels of even-even nuclei / 11 / and the simple interpolations of these energies for nearest odd and odd-odd nuclei. For the octupole excitations, which are influenced on the level densities essentially weaker than the quadrupoles, we used the averaged description of the observed energies $\omega_{3-} = 50 A^{-1/3} \text{ MeV}$. The experimental values of the shell corrections $\delta \epsilon_0$ were taken from Ref. / 7 / and the correlation functions were accepted as $\Delta_0 = 12 A^{-1/2} \text{ MeV}$. From optimal description of the experimental data on the neutron resonance densities / 12 / the value of coefficient $C = 0.075 A^{1/3} \text{ MeV}^{-1}$ was obtained which characterized phenomenologically the effective decrease of the vibrational enhancement of the level density at highly excited nuclei.

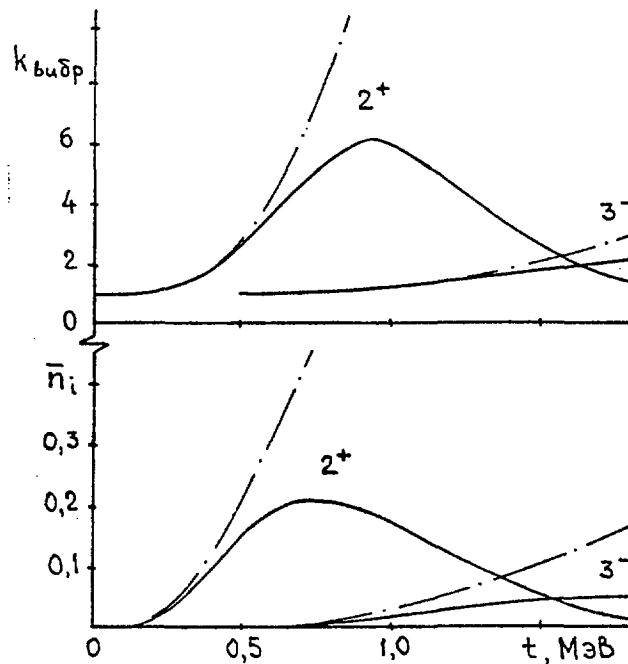


Fig. 1. The temperature dependence of the occupation numbers and the coefficients of vibrational increase of the level density of the nucleus ^{52}Cr under adiabatical approximation (desh-dot curves) and taking into account the damping of vibrational excitations (solid curves).

The optimal parameters do not guarantee of course an exact agreement with the experimental data for any nucleus. However such coincidence is needed often for the calculations of the neutron spectra and the excitation functions of different nuclear reactions. In the framework of described approach we determined also the set of individual parameters $\tilde{\alpha}$ and δ_{eff} which provides the description of the neutron resonance density /12/ and the number of low-lying levels /11/ for each nucleus. These parameters are shown on Fig.2. The individual parameters display the fluctuations which are correlated with the shell structure of nuclei. These fluctuations reflect first and foremost the simplifications connected with the replacement of the realistic correlation functions for protons and neutrons by the averaged value Δ_0 . For the magic numbers of protons or neutrons the values of the correlation functions must be essentially smaller than for the nonmagic numbers and just this effect is displayed in the fluctuations of individual parameters on Fig.2.

At first glance it might seem that the systematics of the level density parameters are not distinguished strongly from the systematics based on the relations of the back-shift Fermi gas model /2/. But it is not correct conclusion. The Fer-

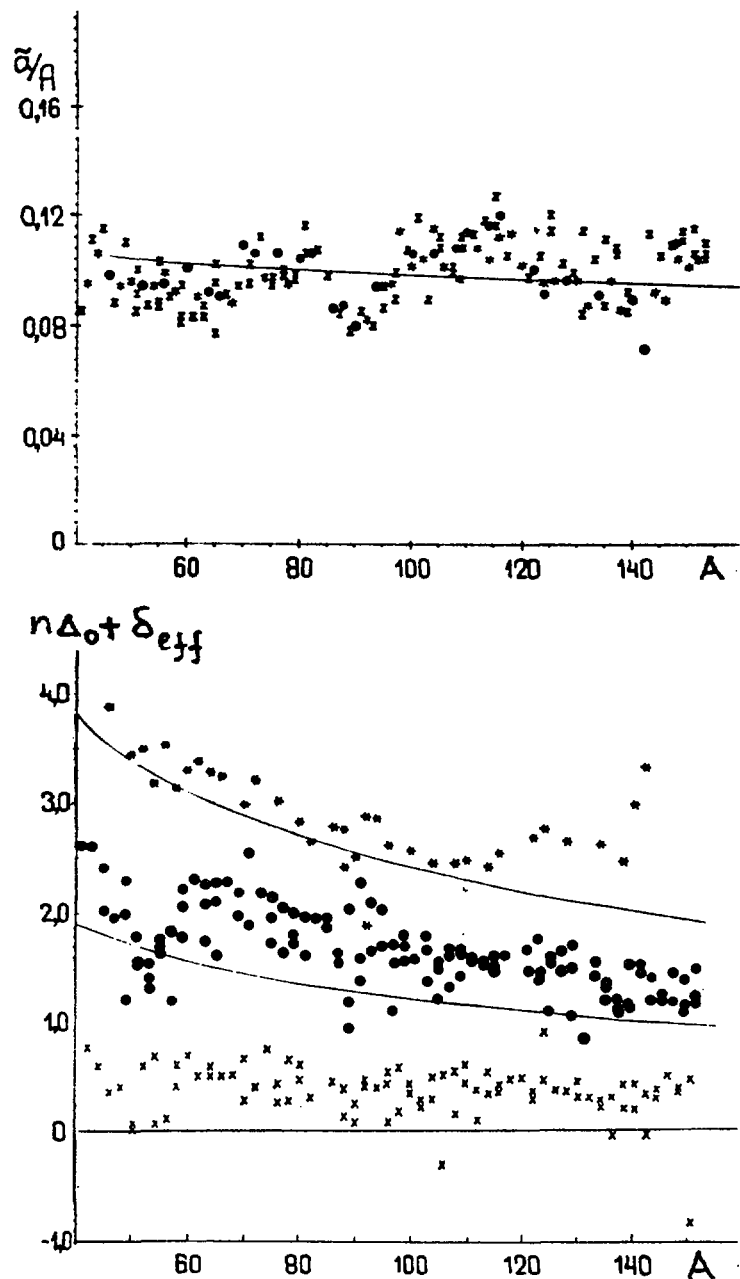


Fig. 2. The effective shifts of excitation energies $n\Delta_0 + \delta_{eff}$ and the asymptotical values of the level density parameters \tilde{a}/A for the even-even (x), odd (●) and odd-odd (*) nuclei. Solid curves are the averaged values parameter \tilde{a}/A and $n\Delta_0 = 12n/\sqrt{A}$ MeV.

mi gas model parameters can be considerably distorted by the shell, superconductive and collective effects. In our approach the obtained parameters have the strict physical meaning and they are in good agreement with the results of pure theoretical calculations of the statistical characteristics of excited nuclei [4].

The necessity of using more rigorous, but inescapably more complicated than the Fermi-gas, models for analysis and description of the nuclear level densities seems almost obvious today. The

complications of the analysis are justified by the consistency of resulting parameters characterizing the diverse experimental information on the statistical properties of nuclei. We hope that the above suggested approach can be fruitful for the practical calculations of the level densities in a wide range of excitation energies and mass numbers.

References

1. Malyshev A.V. Level density and structure of atomic nuclei (Russian). M., Atomizdat, 1969.
2. Dilg W. et al. - Nucl.Phys., 1973, v. A217, p.265.
3. Vdovin A.I. et al. - Phys. elem. part. and nucl., 1976, v.7, p.952.
4. Ignatyuk A.V. Statistical Properties of Excited Atomic Nuclei (Russian). M., Energoatomizdat, 1983.
5. Ignatyuk A.V. et al. - Sov.Nucl.Phys., 1978, v.29, p.875.
6. Ignatyuk A.V., Shubin Yu.N. - Izv. Acad.Sci.,USSR, ser. phys., 1973, v.37, p.1947.
7. Myers W.D. Droplet Model of Atomic nuclei. IFP/Plenum, 1977.
8. Ramamurthy V.S. et al. - In: IAEA Meeting on Basic and Applied Problems of Nuclear Level Density. N.Y.: INDC-092/L, 1983, p.187.
9. Bohr A., Mottelson B. Nuclear Structure, N.Y., Benjamin, 1975, v.2.
10. Landau L.D. - Sov JETP, 1957, v.32, p.59.
11. Lederer C.M., Shirley Y.S. Tables of Isotopes N.Y.: 7 th.ed., 1979.
12. Belanova T.S. et al. Radiative Capture of Neutrons (Russian) M., Energoatomizdat, 1986.

EFFECTS OF REALISTIC PARTIAL STATE
DENSITIES ON PREEQUILIBRIUM DECAY

M. Blann

E-Division, Physics Department
Lawrence Livermore National Laboratory
Livermore, California 94550

G. Reffo

ENEA
Bologna, Italy

1. INTRODUCTION

We reported earlier on the inclusion in code ALICE of a subroutine which calculates partial state densities for preequilibrium decay using realistic single particle levels.¹ In this work, we present results using single particle levels due to Seegar-Howard² and Seegar-Perisho.³ Since the earlier work, we have modified the intranuclear transition rates for nucleon scattering based on the final density of three exciton states available. We summarize the changes made in the hybrid subroutine of ALICE in Section 2, and present our results in Section 3.

2. METHOD OF CALCULATION

The partial state densities for proton particles (p^1), proton holes (p^{-1}), neutron particles (n^1) and neutron holes (n^{-1}) are calculated as described, using the method of Williams et al.⁴ We refer to earlier references for details. We use realistic partial state densities only for the first term in the series (three exciton) and use Ericson densities for higher order terms.

In this work, we will consider proton induced reactions, (p,n) reactions on $^{90,91,92,94}\text{Zr}$. In the entrance channel, the incident proton may populate pnn^{-1} and ppp^{-1} configurations. Only the pnn^{-1} may decay by neutron emission, leaving a final state pn^{-1} . Since the pn free scattering cross section is $\sim 3X$ the pp cross section, we assume that 0.75 of the three exciton state is pnn^{-1} . We therefore calculate the number of neutron excitons emitted leaving a pn^{-1} final state at excitation U (from

This work was performed under the auspices of the U.S. Department of Energy by the Lawrence Livermore National Laboratory under contract number W-7405-ENG-48.

a composite excitation E) as:

$$N(\epsilon, U) = 2 \cdot 0.75 \left(\frac{\rho_{pn}^{-1}(U)}{\rho_{pnn}^{-1}(E)} \right) \left(\frac{\lambda_c(\epsilon)}{\lambda_c(\epsilon) + \lambda+(\epsilon) \cdot R(\epsilon)} \right) \quad (1)$$

The factor 2 in Eq. 1 comes from a factor of (n-1) missing from the expression we use for the three quasiparticle density. The factor R(ε) correct the nucleon-nucleon scattering rate calculated for a Fermi gas according to the ratio of three quasiparticle states available following N-N scattering using realistic single particle levels to those calculated for a Fermi gas,

$$R(\epsilon) = \frac{\rho_{nnp}^{-1}(\epsilon) + \rho_{npp}^{-1}(\epsilon)}{\rho_3(\epsilon)} \quad (2)$$

$$= \frac{2 \times 4 (\rho_{nnp}^{-1}(\epsilon) + \rho_{npp}^{-1}(\epsilon))}{g^3 \epsilon^2}$$

For the proton emission channel,

$$N(\epsilon, U) = 2 \cdot \left(\frac{0.75 \rho_{nn}^{-1}(U)}{\rho_{pnn}^{-1}(E)} + \frac{0.5 \rho_{pp}^{-1}(U)}{\rho_{ppp}^{-1}} \right) \cdot \left(\frac{\lambda_c(\epsilon)}{\lambda_c(\epsilon) + R(\epsilon) \cdot \lambda+(\epsilon)} \right) \quad (3)$$

where

$$R(\epsilon) = \frac{2 \times 4 (\rho_{ppp}^{-1}(\epsilon) + \rho_{pnn}^{-1}(\epsilon))}{g^3 \epsilon^2} \quad (4)$$

3. RESULTS AND DISCUSSION

In Fig. 1, we present results of the experimental⁵ and calculated neutron spectra from the ^{90,91,92,94}Zr(p,n) reaction for 25 MeV incident protons. Calculated results are shown using the geometry dependent hybrid model (GDH), and using the hybrid model with realistic two and three quasiparticle densities, as described in the preceding subsection. For the latter, we use the single particle sets of Seegar-Howard (S-H) and of Seegar-Perisho (S-P). The deformation parameter δ was taken to be -0.05 for all results shown.

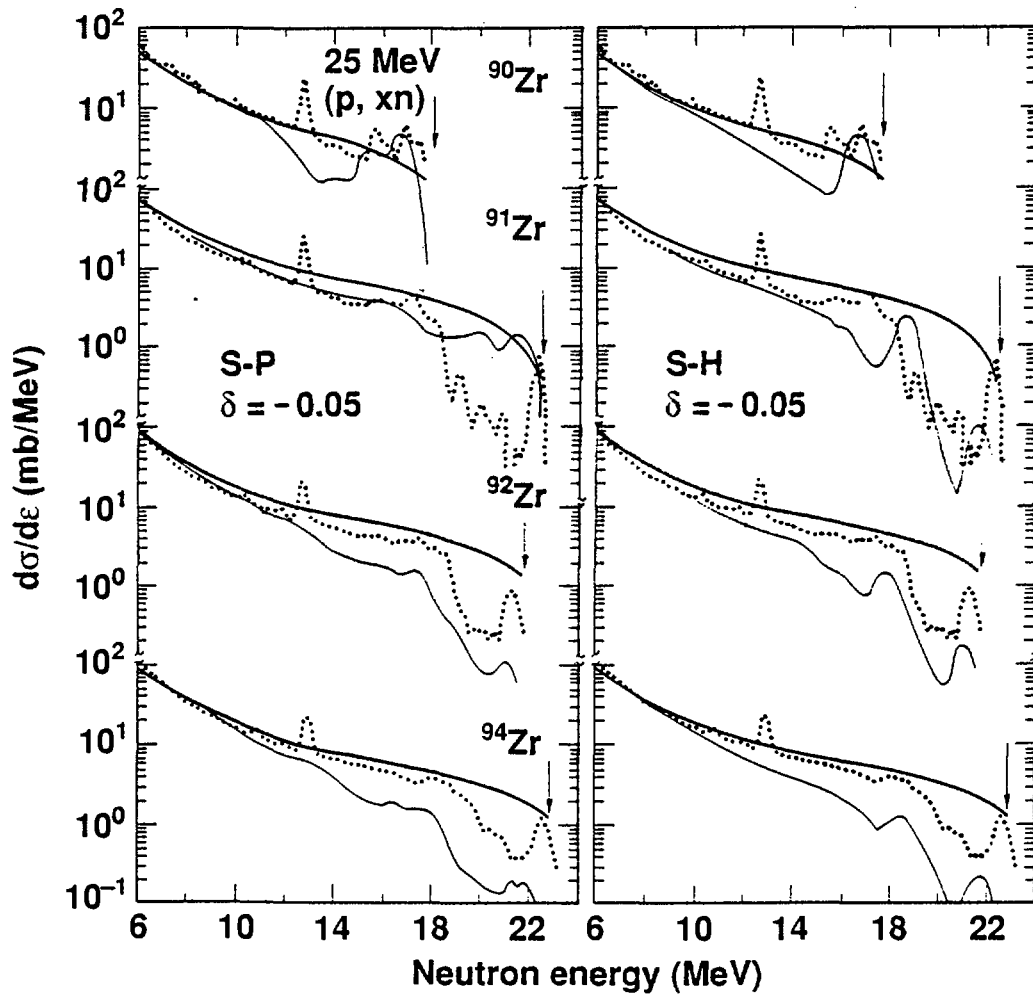


Figure 1 Calculated and experimental neutron spectra for the (p,n) reaction on $^{90,91,92,94}\text{Zr}$. Experimental results of Ref. 5 are given by the dots connected by a thin line. The thin smooth solid line is the result of the GDH model. The heavy lines with structure are the results of the hybrid model using realistic single particle levels, as described in this report.

These results give some encouragement in the use of realistic single particle levels for PE calculations. They also leave much to be desired. Some improvement may result from adding the capability of doing a geometry dependent calculation. More important will be a search for a better set of single particle levels. This remains to be done in the future.

References

1. M. Blann et al., Lawrence Livermore National Laboratory Report UCRL-95397 (1986) unpublished.
2. P. A. Seegar and W. M. Howard, Nucl. Phys. **A238**, 491 (1975).

3. P. A. Seegar and R. C. Perisho, Los Alamos National Laboratory Report No. LA3751 (1967) unpublished.
4. F. C. Williams, Jr., A. Mignerey and M. Blann, Nucl. Phys. A207, 619 (1973); K. Albrecht and M. Blann, Phys. Rev. C8, 1481 (1973).
5. W. Scobel et al., Phys. Rev. C30, 1480 (1984).

THE MSC CALCULATIONS WITH USE OF EMPIRE

A. Marcinkowski
Institute for Nuclear Studies
Warsaw, Poland

The theory of Feshbach, Kerman and Koonin¹⁾ has been applied for calculation of that component of the preequilibrium emission, which demonstrates itself in symmetric angular distributions, namely the multi-step compound emission. The theory considers for this type of reaction the flow of the flux through a series of doorway states of increasing complexity, each of them containing only bound nucleon orbitals. The works at relatively low incident energies about 14 MeV have shown that MSC is able to reproduce data by itself. Indeed, empirical evaluation of direct or multi-step direct MSD components at these energies by extraction of the anisotropic part of the angular distributions leads to the conclusion that such component is of the order of 10% of the total cross section²⁾. This assumption may appear to be not generally valid as follows from the present discussion but it formed a convenient starting point for the implementation of the quantum-mechanical formalism in practical calculations because it avoids the necessity of combining the two completely different types of reaction codes, namely the Hauser-Feshbach statistical theory codes and the DWBA ones. All the MSC calculations have been programmed into the EMPIRE code, which routinely used to evaluate the preequilibrium cross sections according to an angular momentum and geometry dependent version of the HYBRID model³⁾. The formulation of the FKK theory has been based on the analytical expression for the bound particle-hole state densities derived by Stankiewicz et al.⁴⁾ and has been extended to include the full angular momentum coupling scheme for one-half spin particles^{5,6)}. The details of the theoretical formulation will be described in the two following chapters. Next the reader will find the description of changes in input data for the MSC option of EMPIRE code and the comparison of calculations with experiment will be discussed at the end.

1. The Densities of States Accessible in MSC Transition Modes.

The MSC interaction chain involves doorway-states containing merely bound particle orbitals. Early calculations made use of the well known Erison formula, which accounts also for the unbound configurations. Such approximation breaks however at energies exceeding the nucleon binding energy. The bound-particle-hole state densities reported in ref.⁴⁾ have been used to derive the densities of states accessible in the possible transition modes contributing to the preequilibrium emission. The theory assumes three types of transitions, which create, conserve or annihilate a particle-hole pair, respectively. The corresponding densities of accessible states the so called Y-functions Y_n^{n+1} , Y_n^{n-1} , Y_n^n are following:

$$Y_n^{n+1} = \frac{1}{2} g h (h+1) \frac{\omega_{p,h+2}(U)}{\omega_{p,h}(E)} \quad , \quad (1)$$

$$Y_m^n = B g^2 h \frac{\omega_{p-1,h}(U)}{\omega_{p,h}(E)} + \frac{1}{2} \alpha (h+1)(h+2) \frac{g}{\omega_{p,h}(E)} \left[\frac{U-E+2B}{h+2} g \omega_{p-2,h+2}(U) + \beta \omega_{p-2,h+2}(E-2B) - \omega_{p-2,h+2}(U) \right] \quad , \quad (2)$$

$$Y_m^{n-1} = \frac{\omega_{2,1}(E-U) \omega_{p-2,h-1}(U)}{\omega_{p,h}(E)} \quad , \quad (3)$$

with $\alpha = 1$ for $E \leq 2B + U$, $\beta = 1$ for $E > 2B$ and both equal to 0 elsewhere. In these formulas ω are the state densities characterized by the number of excited particles p and holes h (with $p + h = 2n + 1$), g is the equidistant Fermi gas level density, B is the nucleon binding energy, E the total energy of the system, U the excitation energy after particle emission. Subsequently the state density accessible for a damping transition is

$$Y_m^{n+1} \downarrow = g \frac{(h+1)(h+2)}{\omega_{p,h}(E)} \left\{ \frac{1}{2} h \omega_{p,h+2}(E) - \frac{1}{2} \alpha h \omega_{p,h+2}(E-B) + (h+3) \omega_{p-1,h+3}(E) - \alpha \left[(h+3) \omega_{p-1,h+3}(E-B) + \frac{B g^2}{2(h+2)} \omega_{p-1,h+2}(E-B) + B g \omega_{p-2,h+2}(E-B) \right] \right\} \quad (4)$$

with α equal 1 for $E > B$ and 0 for $E \leq B$.

In the above derivations the Pauli principle has been ignored as well as the effect of the finite potential well on the scattering of holes.

2. Angular Momentum Structure of the Transition Widths.

Following the original paper of Feshbach, Kerman and Koonin early calculations were restricted to spinless particles only. This simplification has been removed by generalizing the matrix element of the two-body σ -interaction for one-half spins. This angular momentum structure embodied in the σ force and the assumed spin distributions of the single-particle levels allow a subsequent derivation of the angular momentum dependence of the transition and damping widths in form of the so called X - functions^{1,5,6}).

The matrix element for a two-particle residual interaction of the form $V_0 \left(\frac{4}{3}\pi r_0^3\right) \delta(\vec{r}_1 - \vec{r}_2)$ reads

$$(-1)^{j_1 + l_1 + Q} \frac{I_{l_1 l_2 l_3 l}}{I_{l_1 l_2 l_3 l}} \sum_{j_1 j_2 j_3 j_4} \left\{ \begin{matrix} j_3 j_4 Q \\ j_1 j_2 s \end{matrix} \right\} \begin{pmatrix} j_1 j_2 Q \\ \frac{1}{2} -\frac{1}{2} 0 \end{pmatrix} \begin{pmatrix} j_3 j_4 Q \\ \frac{1}{2} -\frac{1}{2} 0 \end{pmatrix}, \quad (5)$$

for $l_1 + l_3 + Q$ and $l_1 + l_2 + Q$ even and 0 otherwise. Here $j_1, l_1, j_2, l_2, j_3, l_3, j_4, l_4$ and the spins and orbital angular momentum of the four single-particle orbitals involved in the two-body interaction, j_1, l_1 being an orbital in the continuum and j_4, l_4 is the spin of the noninteracting core nucleons, \hat{j} stands for $(2j + 1)^{\frac{1}{2}}$ and I is the overlap radial-integral of wave functions U for the orbitals in question.

$$I_{l_1 l_2 l_3 l} = \frac{V_0}{4\pi} \left(\frac{4}{3}\pi r_0^3\right) \int_0^\infty U_{l_1} U_{l_2} U_{l_3} U_{l_4} \frac{dr}{r^2} \quad (6)$$

The remaining symbols in (5) denote angular momenta composed of the ones described.

Assuming the Bethe's spin distribution R_N of nuclear states, with a spin cut-off factor depending on the number of excitons $N = (p + h)$ one obtains, following the prescription of FKK, the X_n^{n+1} , X_n^n and X_n^{n-1} functions for the possible transition modes leading to particle emission as well as $X_n^{n+1} \downarrow$ for the damping transition denoting no emission into the continuum:

$$X_m^{n+1} = 2\pi \frac{(2l+1)(2s+1)}{R_N(J)} I^2 \sum_{Q j_3 j_4} (2Q+1) R_1(Q) (2j_3+1) F(j_3) R_{N-1}(j_4) \begin{pmatrix} l & Q & j_3 \\ \frac{1}{2} & \frac{1}{2} & 0 \end{pmatrix}^2 \begin{pmatrix} l & j_3 & Q \\ j_4 & j_3 & s \end{pmatrix}^2, \quad (7)$$

$$X_m^n = 2\pi \frac{(2l+1)(2s+1)}{R_N(J)} I^2 \sum_{Q j_3 j_4} (2Q+1) F(Q) (2j_3+1) R_1(j_3) R_{N-2}(j_4) \begin{pmatrix} l & j_3 & Q \\ \frac{1}{2} & -\frac{1}{2} & 0 \end{pmatrix}^2 \begin{pmatrix} l & j_3 & Q \\ j_4 & j_3 & s \end{pmatrix}^3, \quad (8)$$

$$X_m^{s+1} = 2\pi \frac{R_{N-3}(s)}{R_N(J)} I^2 \sum_{Q j_3} (2Q+1) F(Q) (2j_3+1) R_1(j_3) \begin{pmatrix} l & j_3 & Q \\ \frac{1}{2} & -\frac{1}{2} & 0 \end{pmatrix}^2 \Delta(1sJ), \quad (9)$$

where $F(Q)$ stands for the distribution of the angular momentum Q of pair states

$$F(Q) = \sum_{j_1 j_2} (2j_1+1) R_1(j_1) (2j_2+1) R_1(j_2) \begin{pmatrix} j_1 & j_2 & Q \\ \frac{1}{2} & -\frac{1}{2} & 0 \end{pmatrix}^2, \quad (10)$$

the factor $\Delta(1sJ)$ is equal 1 if $|1-s| \leq J \leq 1+s$ and 0 otherwise.

$$X_m^{n+1} \downarrow = 2\pi \frac{I_B}{R_N(J)} \sum_{j_4 Q} R_1(Q) \tilde{F}(Q) R_{N-1}(j_4), \quad (11)$$

with $\tilde{F}(Q) = \sum_{l j_3} (2j_3+1) F(j_3) (2l+1) R_1(l) \begin{pmatrix} l & j_3 & Q \\ \frac{1}{2} & 0 & -\frac{1}{2} \end{pmatrix}^2, \quad (12)$

and $F(j_3) = \sum_{j_1 j_2} (2j_1+1) R_1(j_1) (2j_2+1) R_1(j_2) \begin{pmatrix} j_1 & j_2 & j_3 \\ \frac{1}{2} & -\frac{1}{2} & 0 \end{pmatrix}^2. \quad (13)$

The radial integrals I including the continuum orbital j_{1l} and I_B containing only bound state wavefunctions are calculated according to the prescription of FKK,

$$2\pi I^2 = \frac{4 V_0^2 r_0^2 \text{kmT}_j}{3 \pi^2 A} \quad (14)$$

$$2\pi I_B^2 = \frac{2 V_0^2}{A^2} \quad (15)$$

These integrals provide the absolute scaling for all transition widths $\langle \Gamma(U) \omega(U) \rangle = X_n Y_n(U)$ and thus for the calculated cross sections. The formulae applied in EMPIRE code for calculating the cross sections are equations from (1) to (5) of ref. 7).

The numerical calculations of the angular momentum coupling coefficients entering formulae (7) to (13) are time consuming. A separate subroutine XSLJ has been programmed to conduct the calculation of the X functions. It provides the X_n^{n+1} , X_n^n , X_n^{n-1} and $X_n^{n+1} \downarrow$ factors in tabular form for the first three stages of the reaction $n = 1$ to 3, corresponding to the 2p-1h, 3p-2h and 4p-3h exciton configurations, as functions of angular momentum. These three configurations account for more than 95% of the MSC emission. The output of the XSLJ is stored in a disk-file in form ready for use by the EMPIRE code.

3. Modifications of the input and output data files for the MSC preequilibrium option.

The reader will find the full description of the card-image input for EMPIRE code in ref. 3). In the following the changes required to run an MSC preequilibrium option are listed:

Card No 1. E, A, Z, AP, ZP, SC, TL, FLUC

TL - number of partial waves accounted for in calculation must be 13.0 for MSC

Card No 2. HYBR, SGRO, GC, TORY, C, GAV, GDO, AV

HYBR - equals > 1.0 the number of stages n accounted for in MSC 3.0 recommended value

TORY - equals > 1.0 ratio $\epsilon_{n-p} / \epsilon_{n-h}$ (for more details see eq.(2) of ref. 7)), (4.0 recommended value)

C - equals the part of reaction cross section contributing to MSC, $0 < C < 1.0$ (default $C = 1.0$)

GAV - equal 1.0 denotes Y-functions based on Ericson state density, as in the original paper of FKK, and the overlap integrals according to formulae (15) and (14)
 - equal 2.0 denotes Y-functions based on Ericson state density and the overlap integrals read in from tape file in tabular form

- equal 3.0 denotes Y-functions according to eqs. (1) to (4) and overlap integrals from formulae (15) and (14)
- equal 4.0 denotes Y-functions according to eqs. 1 to 4 and tabulated numerical values of overlap integrals read in from tape file

if GAV = 3.0 or 4.0 then GDO 0. equal to the binding energy of proton or neutron in the composite nucleus

Card No 3. DE, WGL, GST, XIJ, ANN, XNI, OUT

XNI - equal to the number of excitons in the initial configuration 3.0 for MSC recommended

Card No 5. AM, UX, DEL, EO, T

- blank card required for MSC (even when GST = 1.), it means AM = A/8 but can contain the level density parameter different from that value in case AM \neq 0.

The subroutine XSLJ requires only a single input card in a format F10.3,4I10

Card No 1. MCOM, SPIN, INEX, FIN, DEFIN

MCOM - equal to the mass number of the composite nucleus

SPIN - equal 0 for integral spins of the composite nucleus
1 for half-integral spins

INEX - initial exciton number no

FIN - number of excitons for the final configuration
(7 recommended)

DEFIN- equal 2 step in exciton numbers of subsequent configurations

The output of XSLJ consists of matrixes of X_n^n , X_n^{n+1} and X_n^{n-1} followed by the $X_n^{n+1} \downarrow$ vector correspondingly for 3, 5 and 7 excitons, as a function of s, l and J.

Examples of output from the EMPIRE code are attached in ref.³). The changes in the MSC output version are following:

- distinction is made between Γ_{comp} and Γ_{abs}

$$\Gamma_{comp} = C \Gamma_{abs}$$

- a printout of the damping $\Gamma \downarrow$ and total widths $\Gamma_{tot} = \Gamma \downarrow + \Gamma \uparrow$ is added as function of parity (1 denotes positive parity and 2 denotes negative parity) and spin of the composite

nucleus ($I_{\text{comp}} + 1$) written in four columns,

$$\Gamma \downarrow, \Gamma_{\text{tot}}, \pi, (I_{\text{Comp}} + 1)$$

for twice (two parities) 13 values of I_{comp} .
- a title: 1 STEP OF MULTISTEP EMISSION opens a table of 9 x 5 cross section values corresponding to MSC neutron emission from the first doorway state into 45 outgoing energy bins of 1 MeV width. This is followed by the same for protons and all is repeated for the next stages of the MSC process but the cross section tables contain each time the contribution of the preceding stages (summed effect after each stage).

4. Calculations and Discussion

The calculations were concentrated on the disability of the model to describe properly the isotopic differences in the neutron cross sections for molybdenum isotopes. Calculations conducted for ^{92}Mo and ^{100}Mo show that the model describes fairly well the (n,2n) reaction on ^{100}Mo but fails for ^{92}Mo . The latter isotope is a magic neutron number nucleus and therefore one expects a rather low /n,2n/ cross section in this case. This expectation is confirmed by experiment but surprisingly the theory overestimates the closed shell effect providing much too low cross section as indicates the dotted curve in fig. 1. In fact the MSC calculations feel the closed shell only via the binding energies because the particle-hole state densities do not account for shell energy shifts. The compound nucleus emission feels the shell effects via the level densities of Cameron and Gilbert⁸). The problem demonstrates itself in the shape of the emitted neutron spectrum provided by the MSC model. This spectrum is too bumpy at intermediate emission energies from 4 to 10 MeV, as shown in fig. 2, by the dotted line, and too poor at low energies, which contribute to the (n,2n) reaction cross section. The hybrid model of Blann⁹) combined with the compound nucleus decay gives a much better overall agreement with experiment (see the solid lines in figs. 1, 2 and 4). It worthwhile to emphasize that the spectral shape of the emitted

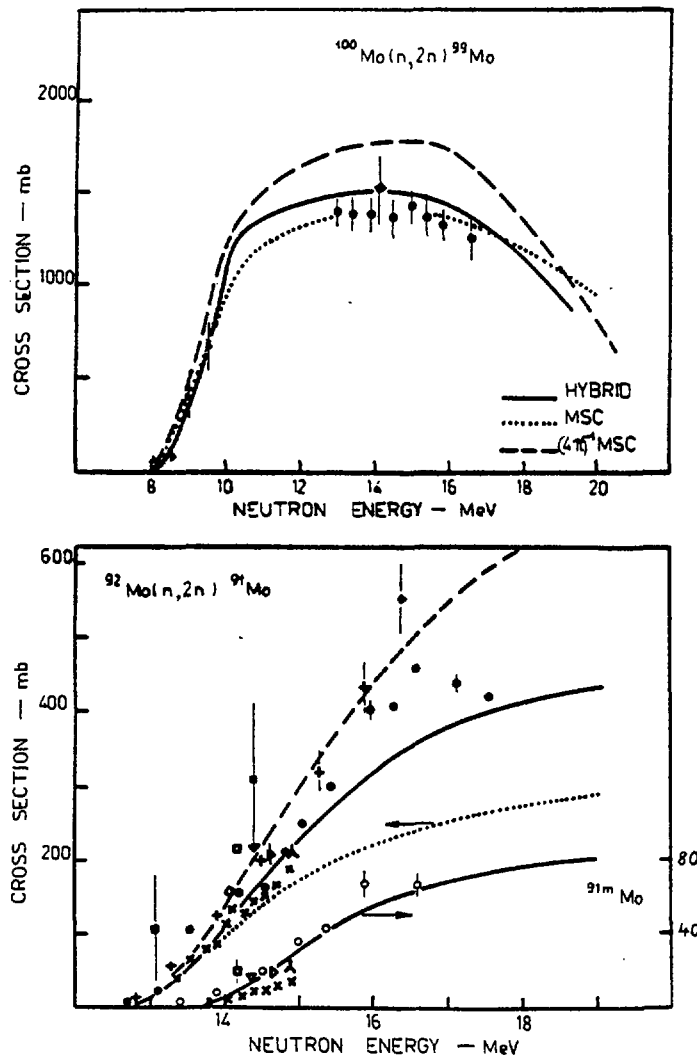


Fig. 1. The excitation curves for the $n,2n$ reaction on ^{92}Mo and ^{100}Mo . The dashed lines denote the MSC calculations normalised according to formula (16). The experimental data are from refs. ¹¹⁾ and ¹²⁾.

neutrons, as calculated from the MSC model is not satisfactory even for the case of ^{100}Mo where the $(n,2n)$ reaction cross sections fit the experimental data very well (compare the dotted lines in figs. 2 and 4).

There have been suggestions of a different absolute normalisation of the FKK cross sections ¹⁰⁾ resulting in a formula for the radial overlap integral

$$2\pi I^2 = \frac{1}{4\pi} \frac{4}{3} \frac{V_0^2 r_0^2 k m T_j}{\pi^2 A}, \quad (16)$$

which decreases the MSC component by an order of magnitude approximately and in this way influences the shape of the

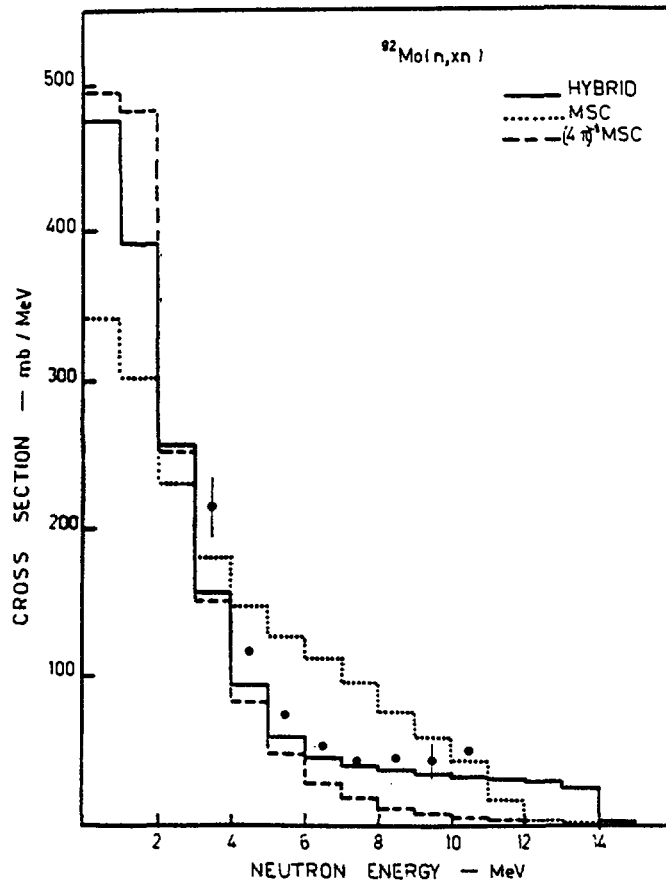


Fig. 2. The spectrum of neutrons emitted from the $^{92}\text{Mo} + n$ interaction at 14.5 MeV. Experimental points are from Takahashi et al. ¹³). Theoretical calculations do not include the n,pn contribution.

emission spectra. In this case one could argue that there is a need to call for the multi-step direct MSD contribution, in order to add the lacking cross section at the high energy end of the spectrum. Such an approach is not improving the situation however because the drastic reduction of the MSC contribution leaves too much place for evaporation, which provides now well enough yield for the (n,2n) process on ^{92}Mo but much too much for ^{100}Mo , as can be seen from the dashed lines in fig. 1. Also the relations between the different channels are getting disturbed. This can be seen from fig. 2, where the dashed line again overestimates the spectrum of protons emitted in the $^{92}\text{Mo}(n,xp)$ reaction.

By introducing the MSD component one could expect a proper reduction of the enhanced evaporational component, but rough estimates indicate that this would simply mean that at 14.5 MeV incoming neutron energy the MSD emission should overwhelm

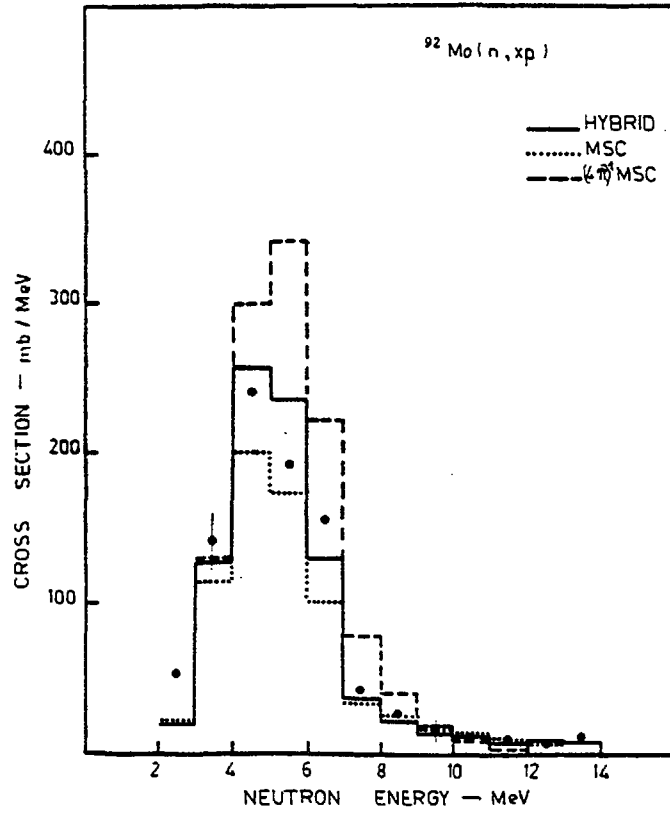


Fig. 3. The spectrum of protons emitted from the $^{92}\text{Mo} + n$ interaction at 14.5 MeV. Experimental points are from Haight et al. ¹⁴).

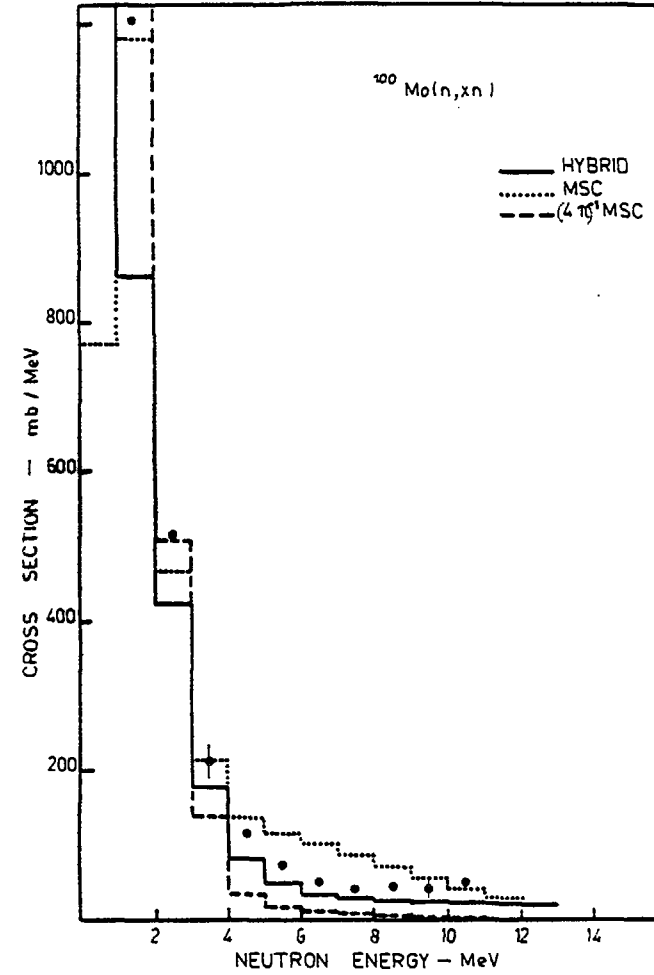


Fig. 4. The same as in fig. 2 but for $^{100}\text{Mo} + n$.

the MSC process, which is in contradiction with the conclusions of earlier studies on the application of the FKK theory conducted by Bonetti and his coworkers²). Another way of removing the difficulties is to find how to harden the MSC emission spectra dotted lines in order to get their shape closer to that predicted by the hybrid model (solid lines).

5. References

1. H. Feshbach, A. Kerman and S. Koonin, Ann. Phys. 125 (1980) 429.
2. R. Bonetti, Proceedings of Intern. Conf. on Fast Neutron Physics, Dubrovnik, May 1986, Report INDC YUG -010/G, p. 2
3. M. Herman, A. Marcinkowski and K. Stankiewicz, Comp. Phys. Comm, 33 (1984) 373
4. K. Stankiewicz, A. Marcinkowski and M. Herman, Nucl. Phys. A435 (1985) 67
5. M. Herman, A. Marcinkowski and K. Stankiewicz, Nucl. Phys. A435 (1985) 859
6. A. Marcinkowski, Contribution to the IAEA Research Coordination Meeting on Methods for Calculation of Fast Neutron Nuclear Data for Structural Materials, Bologna, October 1986
7. M. Herman, A. Marcinkowski and K. Stankiewicz, Nucl. Phys. A430 (1984) 69
8. A. G. W. Cameron and G. Gilbert, Can J. Phys. 43 (1965) 1446
9. M. Blann, Nucl. Phys. A213 (1973) 570
10. K. Stankiewicz, private communication
11. Handbook on Nuclear Activation Cross-Sections, IAEA Technical Reports Series No 156, Vienna 1974
12. A. Marcinkowski, K. Stankiewicz, U. Garuska and M. Herman Z. Phys. 323 (1986) 91
13. A. Takahashi et al., OKTAVIAN Report A-83-01, June - 1983
14. R. C. Haight, S.M. Grimes, R.G. Johanson and H.H. Barshall, Phys. Rev. C23 (1981) 700

ON THE TWO GAS APPROACH FOR EXCITON MODEL
MASTER EQUATION

G. Reffo, M. Herman[^], C. Costa^{^^}
ENEA, CRE Clementel, Bologna, Italy

Abstract.

A new version of the two component exciton model with introduction of shell model quasi-particle state densities is presented.

A transformation of the master equation is proposed to facilitate the calculations. On this basis, flux flow between different substages of the composite nucleus is analysed and large discrepancies are found in the strength of various transitions.

Introduction.

The problem of neutron-proton distinction in the equilibration of the composite nucleus was addressed already in the early stage of preequilibrium development /1/, /2/, receiving however little attention, mainly because two component calculations are much more involved and the results /3/, /4/ did not show convincing improvements.

Recently Gupta /5/ provided with a justification of one component model, by showing that the inclusion of transitions inconsistent with the assumption of the two body nature of the intranuclear interaction (as it is implicitly done in usually adopted one component models) can be compensated by changing the averaged matrix element. This holds, however, only if the state density for equivalent proton and neutron configurations are the same.

Our recent shell model calculations /6/, /7/, on the contrary, show large discrepancies both in the thresholds for the excitation of certain configuration and in the energy distribution of the states, as can be seen in fig. 1, where a comparison of neutron and proton state densities for the two- and four-exciton configurations in ^{90}Zr is presented.

Accounting for these differences is only possible if an explicit two component formulation of the exciton model is used.

[^] ENEA contract n. 6886

^{^^} ENEA contract n. 25888

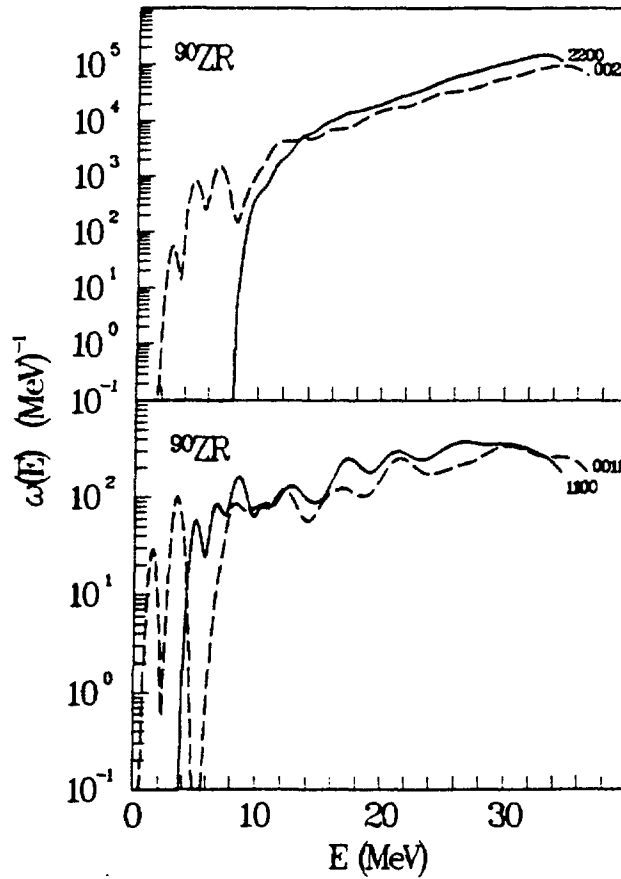


Fig. 1. Comparison of neutron and proton state densities for 2- and 4-exciton configurations in ^{90}Zr .

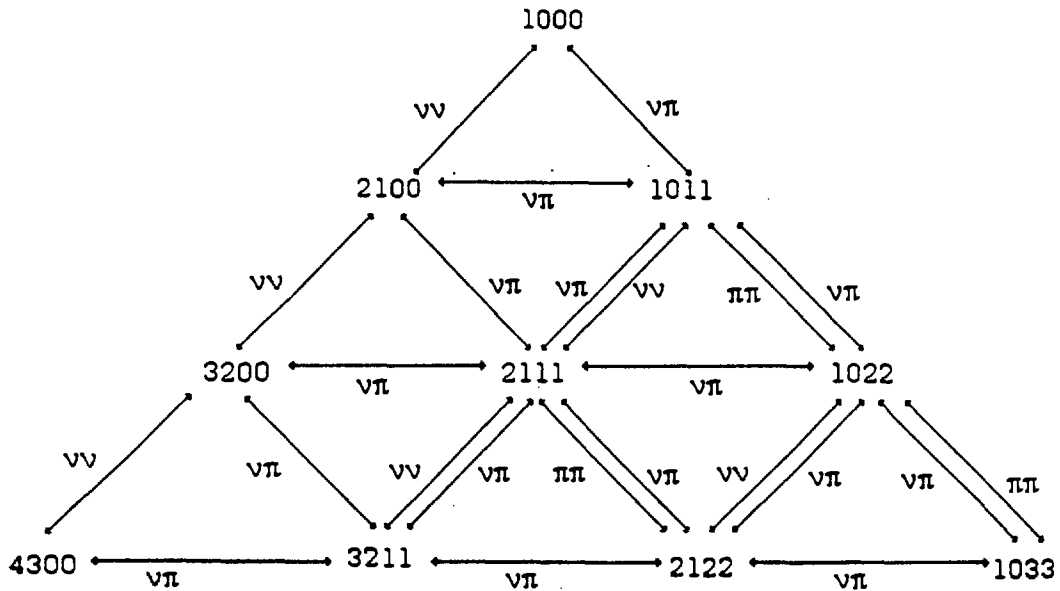


Fig. 2. Schematic diagram of the equilibration of the composite nucleus formed in the neutron induced reaction. Different substages are denoted with p_ν , h_ν , p_π , and h_π . Arrows are labelled with the type of interacting nucleons.

The model.

Following the approach of Dobes and Betak /3/, the model we report herein is based on the fundamental assumption of the one-component exciton model. The equilibration of the system is described in terms of transitions between subsequent stages, classified according to the reaction stage number N and to the proton hole number h_π .

The two body residual interaction implies that the coupling is possible only between closest stages.

The equilibration process can be illustrated on a two dimensional plot, as shown in fig. 2 in the case of a neutron projectile.

The master equation for the two component system reads:

$$\begin{aligned}
 \frac{dP(N, h_\pi, t)}{dt} = & (\lambda_{\nu\pi}^{++}(E, N-1, h_\pi-1) + \lambda_{\pi\pi}^{++}(E, N-1, h_\pi-1)) P(N-1, h_\pi-1, t) \\
 & + (\lambda_{\pi\nu}^{+0}(E, N-1, h_\pi) + \lambda_{\nu\nu}^{+0}(E, N-1, h_\pi)) P(N-1, h_\pi, t) \\
 & + (\lambda_{\nu\nu}^{-0}(E, N+1, h_\pi) + \lambda_{\pi\nu}^{-0}(E, N+1, h_\pi)) P(N+1, h_\pi, t) \\
 & + (\lambda_{\pi\pi}^{--}(E, N+1, h_\pi+1) + \lambda_{\nu\nu}^{--}(E, N+1, h_\pi+1)) P(N+1, h_\pi+1, t) \\
 & + \lambda_{\nu\pi}^{0+}(E, N, h_\pi-1) P(N, h_\pi-1, t) \\
 & + \lambda_{\pi\nu}^{0-}(E, N, h_\pi+1) P(N, h_\pi+1, t) \\
 & - (\lambda_{\nu\nu}^{+0}(E, N, h_\pi) + \lambda_{\pi\nu}^{+0}(E, N, h_\pi) + \lambda_{\nu\pi}^{++}(E, N, h_\pi) + \lambda_{\pi\pi}^{++}(E, N, h_\pi) \\
 & + \lambda_{\pi\nu}^{--}(E, N, h_\pi) + \lambda_{\pi\pi}^{--}(E, N, h_\pi) + \lambda_{\nu\pi}^{-0}(E, N, h_\pi) + \lambda_{\nu\nu}^{-0}(E, N, h_\pi) \\
 & + \lambda_{\pi\nu}^{0-}(E, N, h_\pi) + \lambda_{\nu\pi}^{0+}(E, N, h_\pi) + W(E, N, h_\pi)) P(N, h_\pi, t)
 \end{aligned} \tag{1}$$

Here $P(N, h_\pi, t)$ is the population of (N, h_π) substages at time t and $W(E, N, h_\pi)$ is the emission rate, written in analogy to the one component exciton model, where state densities were replaced by the two gas expression. The internal transition rates are denoted by λ , the superscripts indicate the change in N and h_π , while the subscripts stand for the type of interacting nucleons.

The following selection rules hold:

$$\begin{aligned}
 \Delta N = -1 ; & \quad \Delta h_\pi = -1, 0 \\
 \Delta N = 0 ; & \quad \Delta h_\pi = 1, -1 \\
 \Delta N = 1 ; & \quad \Delta h_\pi = 0, 1
 \end{aligned} \tag{2}$$

with boundary conditions $N > 0$, $0 \leq h_\pi < N$.

The two dimensional population matrix can be transformed into a vector, noting that the substages can be labelled by a running index j starting from the top of fig. 2 and enumerating along subsequent rows from the left to the right.

The new index j is related to N and h_{π} by:

$$j = N(N-1)/2 + h_{\pi} + 1 \quad (3)$$

and for each j we can obtain N and h_{π} through the expressions:

$$N = \text{Int}(0.5 + \sqrt{2j - 1.75}); \quad h_{\pi} = j - N(N-1)/2, \quad (4)$$

where Int denotes the Entier function.

Equation i is transformed, this way, into a set of linear differential equations. The selection rules (2) in j -representation are obtained noting that a given substage j is coupled to the following i substages:

$i=j-N+1$ and $i=j-N$ through $\Delta N=-1$ transitions with boundary conditions $(N-2)(N-1)/2 < i < N(N-1)/2$

$i=j+1$ and $i=j-1$ through $\Delta N=0$ transitions with boundary conditions $N(N-1)/2 < i < N(N+1)/2$

$i=j+N$ and $i=j+n+1$ through the $\Delta N=1$ transitions with no boundary conditions.

The two component master equation indexed with j nicely links to the one component version, as it is illustrated in fig. 3, where the thick horizontal and vertical lines are drawn to separate the reaction stages.

In fig. 4 we show diagrams illustrating the 18 different processes that contribute to internal transitions.

Transition rates are obtained from Fermi's Golden Rule as the product of the average squared matrix element and the density of final accessible states. The latter can be calculated by distinguishing the excitons taking part in the interaction, from the passive part that behaves like a spectator. The probability $P(\epsilon, p_v, h_v, p_{\pi}, h_{\pi})$ of finding the interacting part with energy ϵ , in the system at energy E , is given by the ratio of the state density of the passive part with energy $E-\epsilon$, to the density of states for the whole system.

The total number of interacting configurations is given by the product of the above probability and the density of initial states for the interacting part $\omega_i^{\text{int}}(\epsilon)$.

The density of accessible states $\omega_{\text{acc}}(E)$ is then obtained by multiplying the total number of interacting configurations times the density of the final states for the interacting part

N											
	j	1	2	3	4	5	6	7	8	9	10
1	1	L	λ^{-0}	λ^{--}							
	2	λ^{+0}	L	λ^{0-}	λ^{-0}	λ^{--}					
2	3	λ^{--}	λ^{0-}	L		λ^{-0}	λ^{--}				
	4		λ^{-0}		L	λ^{0-}		λ^{-0}	λ^{--}		
	5		λ^{++}	λ^{+0}	λ^{0+}	L	λ^{0-}		λ^{-0}	λ^{--}	
3	6			λ^{--}		λ^{0+}	L			λ^{-0}	λ^{--}
	7				λ^{-0}			L	λ^{0-}		
	8				λ^{--}	λ^{-0}		λ^{0-}	L	λ^{0-}	
	9					λ^{--}	λ^{-0}		λ^{0-}	L	λ^{0-}
4	10						λ^{--}			λ^{0-}	L

Fig. 3. Schematic representation of the j-indexed master equation. Thick lines separate different stages of the equilibration process. Off-diagonal elements represent the gain of the flux from other substages, while diagonal elements L are responsible for the loss of the flux due to the coupling to other substages and to the open channels.

$\omega_f^{int}(\epsilon)$, and integrating over ϵ from 0 to E.

$$\omega_{acc}(E) = \int_0^E P(\epsilon, p_v, h_v, p_\pi, h_\pi) \omega_i^{int}(\epsilon) \omega_f^{int}(\epsilon) d\epsilon \quad (5)$$

For each of the 18 processes illustrated in fig. 4 the density of accessible states is calculated according to formula (5); the transition rates are then obtained by applying the Golden Rule and summing the contributions from the appropriate processes.

To account for the most important effects of the shell structure, the expression of Williams /8/ for the two component state density can be modified as it follows:

$$\omega(E, p_v, h_v, p_\pi, h_\pi) = \frac{g_v^p \tilde{g}_v^h g_\pi^p \tilde{g}_\pi^h (E-S)^{n-1}}{p_v! h_v! p_\pi! h_\pi! (n-1)!} \Theta(E-T) \quad (6)$$

where the Heaviside function $\Theta(E-T)$ excludes states below the threshold T for a given exciton configuration; single particle state densities for particle g and for holes g are distinguished

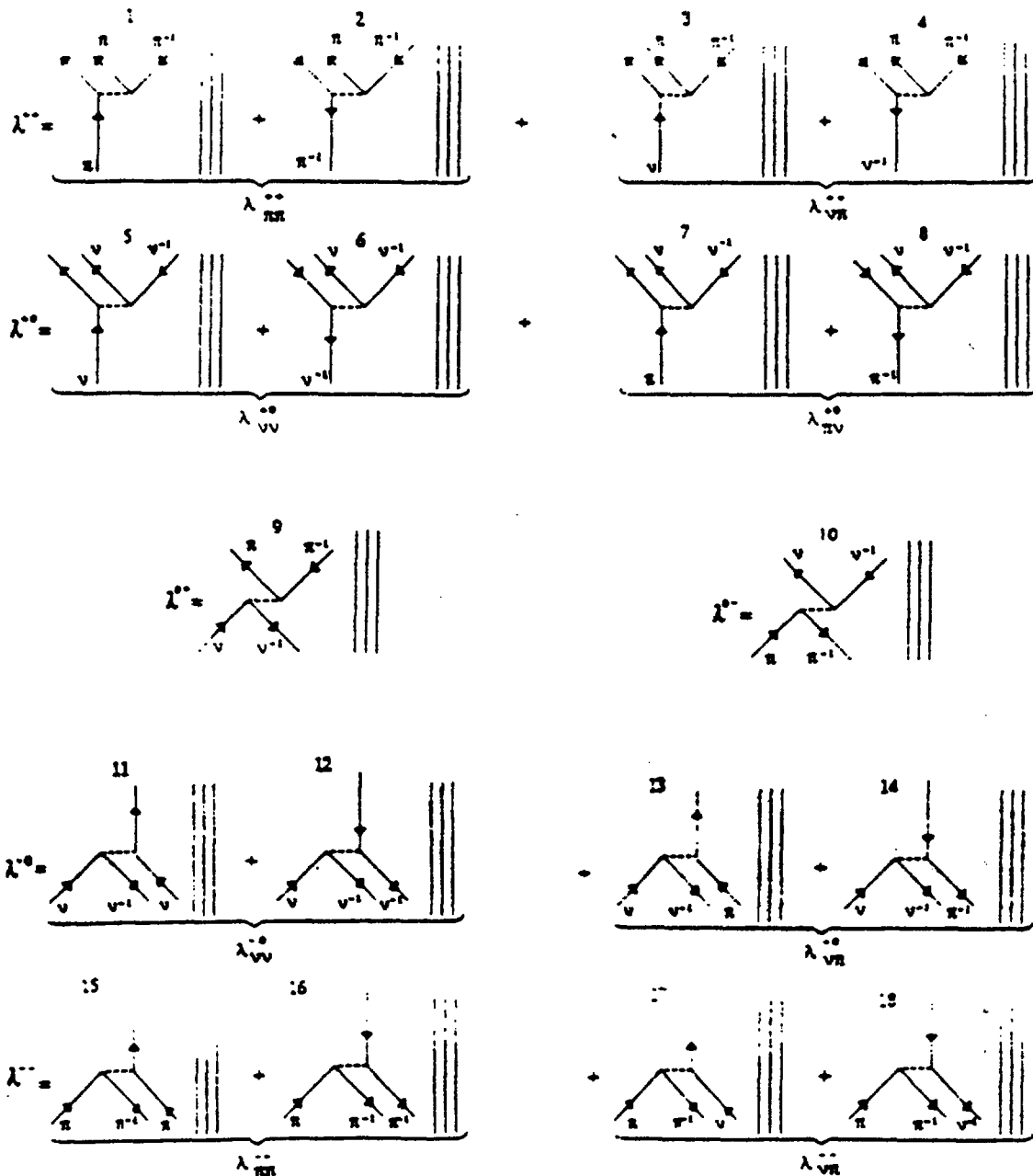


Fig. 4. Diagrams illustrating intranuclear transitions in the two component exciton model. Interacting particles (holes) are represented by upward (downward) arrows, and their nucleon type is indicated. Vertical lines stand for the passive excitons. The diagrams are enumerated to facilitate reference.

and S represents an energy shift accounting for Pauli principle correction.

A closed form can be obtained for eq. 5 adopting expression 6.

Results.

Qualitative analysis of flux flow through different substages of the composite system can be performed on the basis

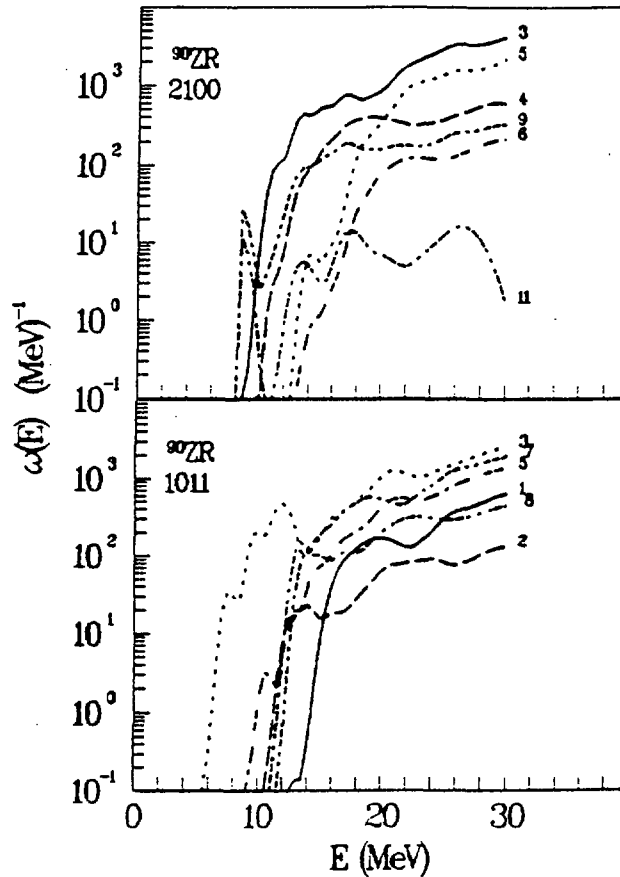


Fig. 5. Accessible state densities for the decay of (2100) and (1011) substages in ^{90}Zr as a function of excitation energy. Curve are denoted by numbers, which relate them to the appropriate diagram of fig. 4.

of the transition rates and, in particular, in terms of the accessible state densities, assuming all equal matrix elements.

We have obtained the accessible state densities performing a numerical integration of eq. 5 in which state densities calculated according to refs. 5 and 6 have been used.

We have chosen, as an example, ^{90}Zr which is a magic nucleus with respect to neutrons.

We discuss the (2100) and (1011) configurations, corresponding to the first stages of a neutron induced reaction.

In fig. 5 we present a number of accessible state densities for the decay of both configurations as a function of excitation energy; the number denoting the curves are related to the processes illustrated in fig. 4.

Strongest shell structure effect is observed at low excitation energy. Accessible state density are characterized by thresholds scattered over a wide energy range. At low energies one may thus expect strongly nonuniform flux through different substages. In general, due to Pauli's principle, accessible state density for the unlike transitions are higher than those for the like ones.

In the decay of (2100) configuration, creation of the proton particle-hole pair by a neutron particle (diagram 3 in fig. 4) is the leading process. Creation of the neutron particle-hole pair (diagram 5) becomes important only above 20 MeV excitation energy and is about a factor two less probable. Analogous transitions caused by the neutron-hole (diagram 6) is an order of magnitude weaker.

The (1011) configuration below 12 MeV decays almost exclusively via the proton pair creation induced by the neutron particle.

Therefore the main part of the flux in the equilibration process will pass through substages laying in the middle of the graph shown in fig. 2.

In the decay of this early stage configurations the leading process is the creation of an exciton pair. Intersubstage transitions (diagram, 9) and backward transition (diagram 11) are found to be respectively one and two order of magnitude lower.

Conclusions.

We have shown that use of a two component exciton model becomes necessary when shell model densities of quasi-particle states are adopted.

We have presented a transformation of the two component master equation into a form that can be easily solved by standard numerical methods.

From the study of the accessible state densities, the leading decay mode of the composite nucleus has been found to be the creation of a particle-hole pair by a particle of the opposite nucleon type.

Due to the shell structure, a non-uniform flow of the flux through different substages is expected.

References

1. E. Betak, J. Dobes, Acta Phys. Slov. 29, 76 (1979).
2. E. Betak, P. Oblozinski, I. Ribanski, Nucleonika 19, 687 (1974).
3. J. Dobes, E. Betak, Z. Phys. A310, 329 (1983).
4. C. Kalbach, Phys. Rev. C33, 813 (1986).
5. S. K. Gupta, Z. Phys. A303, 329 (1981).
6. M. Herman, G. Reffo, Phys. Rev. C36, 1546 (1987).
7. M. Herman, G. Reffo, A. Rego, Phys. Rev. C37, 184 (1988).
8. F.C. Williams Jr., Phys. Lett. 321B, 184 (1970).

ANALYSIS OF THRESHOLD REACTION CROSS-SECTIONS AND
SPECTRA OF PARTICLES EMITTED IN THEM ON IRON-GROUP
NUCLEI

V.M. Bychkov, O.T. Grudzevich, A.V. Zelenetsky,
A.B. Pashchenko, V.I. Plyaskin
Centr Po Jad. Dannym
Obninsk, Kaluga Region, USSR

1. Introduction.

The present work deals with the analysis of excitation functions and particle emission spectra in neutron reactions with an energy up to 20 MeV with nuclei in the mass range $50 < A < 70$ within the framework of theoretical models of nuclear reactions. The basic prominence has been given to consideration of the problem on the possible difference of the cross-section of particle absorption by nucleus in the ground and excited state, being under discussion in the literature for a long time [1,2].

In Refs. [3] on the basis of excitation functions analysis of (n,p) , (n,α) , $(n,2n)$ reactions according to the statistical theory it was concluded, that for experimental data description the selection of varying level density parameters in neutron and proton channels was required. A probable difference of inverse reaction cross-section from absorption cross-section calculated by an optical models was specified as one of feasible reasons of this mismatch.

In Ref. [4] on the basic of α -particle emission spectra analysis in the (n,α) reaction a conclusion was made on the essential difference of absorption cross-sections for excited and cold nuclei.

The present work applies the results of recent investigations obtained in nuclear level density description [7,8] to look into this problem in more detail.

2. Models used in the experimental data analysis .

The approach for particle emission spectra and cross-sections analysis is based on the reaction mechanism being divided into three components: direct, preequilibrium and equilibrium ones. The (V_0, V_1) reaction cross-section where the outgoing particle V_1 energy is in the range $E_{\pm} \pm E/2$ and the residual nucleus is in the state with a spin I_1 and parity π_1 is writ-

ten as follows:

$$\frac{d\sigma_{\nu_0\nu_1}}{dE_1}(E_1, I_1, \pi_1) \Delta E = q \frac{d\sigma_{\nu_0\nu_1}^{eq}}{dE_1}(E_1, I_1, \pi_1) \Delta E + \frac{d\sigma_{\nu_0\nu_1}^{pre}}{dE_1}(E_1, I_1, \pi_1) \Delta E + \sigma_{\nu_0\nu_1}^{dir}(E_1, I_1, \pi_1); \quad (1)$$

where $q = 1 - \frac{1}{\sigma_a} \left[\sum_{\nu_1} \sum_{E_1, I_1, \pi_1} \sigma_{\nu_0\nu_1}^{dir}(E_1, I_1, \pi_1) + \sum \int \frac{d\sigma_{\nu_0\nu_1}^{pre}}{dE_1}(E_1, I_1, \pi_1) dE_1 \right]$.

Here σ_a - is the particle ν_0 absorption cross-section in the entrance channel; the letters: eq, pre, dir - stand for the contributions of the equilibrium, preequilibrium and direct components, respectively, to the reaction cross-section. To compare this expression with the experimental data on energy spectra it should be summed over the spin and parity of the residual nucleus.

$$\frac{d\sigma_{\nu_0\nu_1}}{dE_1}(E_1) \Delta E = \sum_{I_1, \pi_1} \frac{d\sigma_{\nu_0\nu_1}}{dE_1}(E_1, I_1, \pi_1) \Delta E; \quad (2)$$

The reaction equilibrium component is calculated within Hauser-Feshbah formalism:

$$\frac{d\sigma_{\nu_0\nu_1}^{eq}}{dE} (E_1, \tau, \pi) = \frac{\pi}{k_0^2} g_{\tau} T_{\nu_0}^{\tau\pi} \cdot W_{\nu_1}^{\tau\pi}(E_1); \quad (3)$$

$$W_{\nu_1}^{\tau\pi}(E_1) = \frac{T_{\nu_1}^{\tau\pi}(E_1) S_{\nu_1}^{\tau\pi}(u_1)}{\int_{E'} \sum_{\nu} T_{\nu}^{\tau\pi}(E') S_{\nu}^{\tau\pi}(u') dE'}$$

It is implied, that the indices ν define the particle type as well as all quantum numbers in the corresponding channel.

k_0 - is the particle ν_0 wave number in the entrance channel;

τ - is the compound nucleus spin, g_{τ} - the statistical factor;

$T_{\nu}^{\tau\pi}$ - is the transmission coefficient of nucleus for the particle ν ;

The indices $\tau\pi$ mean the condition of spin and parity conservation with the formation and decay of the given compound-nucleus state.

$S_v^{\pi\pi}$ - is the residual nucleus level density in the channel v .

The preequilibrium component is calculated within the exciton model [5].

$$\frac{d\tilde{\sigma}_{\nu_0\nu_1}^{pre}}{dE_1}(E_1) = \tilde{\sigma}_a \cdot \sum_n P_n^{\nu_1} \cdot \frac{\lambda_{em}^{\nu_1}(n, E_1)}{\sum_v \int \lambda_{em}^v(n, E_v) dE_v + \lambda_+(n, E_c)} \quad (4)$$

where P_n^v is a relative probability of v -type particle occurrence in the n -quasi-particle state;

$\lambda_{em}(n, E)$ - is the probability of v -particle emission, with an energy E from the n -quasi-particle state;

$\lambda_+(n, E_c)$ - is the rate of transition from the n -exciton state with the energy $E_c = E_{\nu_0} + B_{\nu_0}$, where B_{ν_0} is the ν_0 -particle binding energy.

The preequilibrium emission exciton model version employed here is based on fairly simple representations and does not claim the detailed description of spectra taking into account the states specific by spin and parity, nevertheless it adequately predicts energy-averaged contribution to the hard part of the emission spectrum.

The component $\tilde{\sigma}_{\nu_0\nu_1}^{dir}(E, I, \pi_1)$ is calculated for direct transitions to discrete levels of the residual nucleus with the known quantummechanical characteristics within frameworks of the couple channel method or the distorted waves method.

The particle ν_2 emission spectrum in the second cascade of the reaction is defined via the spectrum of single-emission cascade (1), as:

$$\begin{aligned} \frac{d\tilde{\sigma}_{\nu_0\nu_1\nu_2}}{dE_2}(E_2, I_2, \pi_2) \Delta E_2 &= \sum_{I_1, \pi_1} \int_{E_1} \frac{d\tilde{\sigma}_{\nu_0\nu_1}}{dE_1}(E_1, I_1, \pi_1) dE_1 \cdot \\ &\times \frac{T_{\nu_2}^{I_1, \pi_1}(E_2) S_{\nu_2}^{I_1, \pi_1}(u_2)}{\int_{E'} \sum_v T_v^{I_1, \pi_1}(E') S_v^{I_1, \pi_1}(u') dE'} \cdot \Delta E_2; \end{aligned} \quad (5)$$

Contributions of the above-mentioned mechanisms vary depending on individual properties of nuclei, interaction energy and reaction type. For the reaction (n, p) and (n, α) on the nuclei considered in this work and in the energy range up to 20 MeV the

main contribution to the total reaction cross-section is made by the equilibrium component, whereas the contributions of the preequilibrium and direct mechanisms are insignificant. The contribution of the preequilibrium and direct components for the (n,n') reaction on the same nuclei at the energy $E_n \gtrsim 10$ MeV is already essential and it should be taken into account not only for the adequate description of cross-sections and spectra in a neutron channel, but also for the proper normalization (factor q in formula (1)) of cross-sections and spectra in other reaction channels.

The main factors affecting the absolute value and the particle emission spectrum shape in different reaction channel are residual nuclei levels density and transmission coefficients of particles in exit channels.

3. Nuclear level density.

The relations of Fermi-gas model [1] are most frequently used in the calculations of level density, where the energy dependence of level density is determined by the parameter "a" and the correction for even-odd differences " δ ". Wide-spread occurrence was obtained for the systematics of Dilg et al. level density [6], where the parameters "a" and " δ " were selected under the conditions of level density energy dependence description by two experimental points: a low-lying levels of the excited nucleus and neutron resonance density at neutron binding energy. In this systematics the parameters " δ " for odd-odd nuclei have negative values, that is the reason of this approach acquiring the name of the "Back-shift" Fermi-gas model.

In contrast to other systematics, employing the Fermi-gas model, it yields the level densities more close to the observed values depending on the excitation energy. Extended systematics of this model parameters on the basis of current experimental data was performed in Ref. [7].

The Fermi-gas model, however, ignores a number of essential properties in nuclear excited state spectra such as shell structure of a single-particle spectrum, correlation effects of superfluid nature and coherent collective effects. These effects can be taken into account most consistently in the microscopic approach within the generalized superfluid model (GSN) of nucleus [1].

Ref. [8] put forward a phenomenological version of GSN taking into account collective, superfluid and shell effects in

level density and quotes the systematics of GSN parameters for nuclei in the mass range $40 \leq A \leq 150$ obtained from the analysis of experimental data on neutronresonance density and on low-lying nuclear levels.

The calculations of level density on the basis of suggested approach agree with the results of the microscopic level density calculations. The analysis of (p,n) reaction particle emission spectra indicates the requirement of employing only the generalized superfluid model for the consistent description of level density in a wide energy range.

4. Particle absorption cross-sections in optical model of nuclear reactions.

The relations of both statistical and preequilibrium models incorporate inverse reaction cross-sections or cross-sections of particle absorption by residual nuclei built-up in exit channels of reactions. A significant factor is the need to know the cross-sections of particle absorption by excited nuclei. The optical model calculation results for a nucleus-target in the ground state are adopted as such data, the dependence of absorption cross-section on nuclear excitation energy commonly being unknown. The "global" parameters of optical potential determined from the condition of the description of experimental data on elastic and inelastic scattering of nucleons and compound particles in a wide energy range and for a great number of nuclei were adopted in practical calculations, or the "individual" parameters obtained at potential parameters adjustment by the experimental data for specific nuclei were adopted.

A brief qualification of the most common "global" potential for neutrons, protons and alphaparticles is given below.

1. The potentials by Wilmore-Hodgson [9], Becchetti-Greenleess [10], Rapaport [11] assigned to nuclear masses $A \geq 40$ and neutron energies from 10 to 40 MeV are frequently used for neutrons. These potentials provide not quite satisfactory description of the data at low neutron energies ($0 < E_n \leq 7$ MeV), that is why the potential [12] has been employed, which was determined by way of individual adjustment of the data for nuclei of Cr-Fe-Ni group in the neutron energy range 1-15 MeV.
2. The use of Perey's potential [13], recommended for the nuclear range $30 < A < 100$ and proton energies $E_p < 20$ MeV, is common for protons, and Becchetti-Greenleess potential [10] - for proton energies from 10 to 50 MeV and nuclear masses $A > 40$.

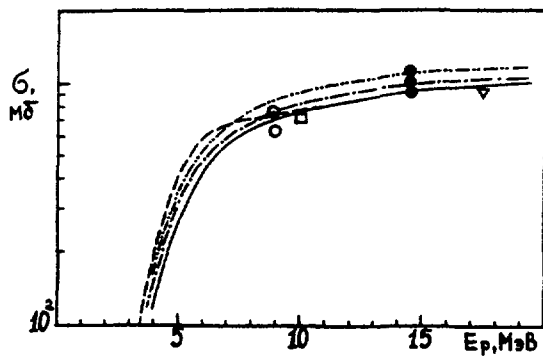


Fig.1. Comparison of experimental and calculated data on the cross-section of proton absorption by Ni nucleus:
 — potential [12];
 - - - potential [12] with enhancement α_R ;
 - · - · - Perey's potential [13];
 - - - Becchetti-Greenless potential [10];
 Experimental data from compilation [10].

Fig.1 represents the comparison of experimental data on a proton absorption cross-section for Ni nucleus with the calculation results by the optical model with varying potentials.

The comparison illustrates that somewhat better description of data within the low proton energy range provides potential [12] obtained for Cr-Fe-Ni nuclei through individual adjustment of neutron data. This potential was adopted in inverse reaction cross-section calculations in the present work.

3. The potentials by Mc.Fadden and Satchler [14], Trombik [15] and Huizenga and Igo [16] are known for alpha-particles. These potentials were obtained from the experimental data analysis in the energy range of alpha-particles $\sim 20 - 30$ MeV.

Fig.2 shows the comparison of calculation results for these three potentials with the available experimental data on the alpha-particle absorption cross-section by Co^{59} nucleus.

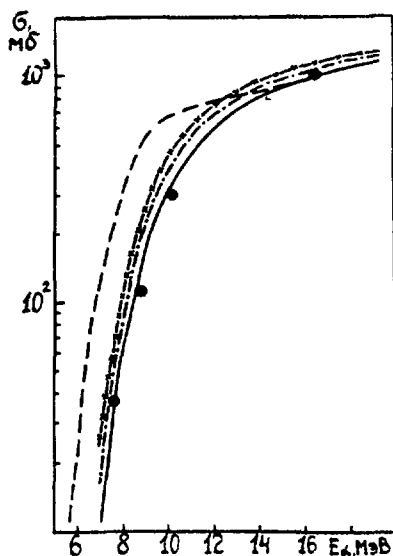


Fig.2. Comparison of experimental and calculated data on the cross-sections of α -particle absorption by Co^{59} nucleus:
 — Mc.Fadden-Satchler's potential [14];
 - - - potential [14] with enhancement α_R ;
 - · - · - Trombik's potential [15];
 - · - · - Huizenga-Igo's potential [16];
 Experimental data from Ref. [18].

As one can see in the fig. 2 Mc.Fadden's potential, selected for the work, provides somewhat better description of the experimental results.

5. Calculation results.

Figs. 3-5 show the calculation results of proton and α -particle emission spectra at neutron interaction with the energy about 15 MeV with nuclei Cr^{52} , Fe^{56} and Ni^{60} . The solid curves correspond to the calculations with the parameters of optical potentials selected in the previous section and with the density of residual nuclear levels calculated within frameworks of GSM.

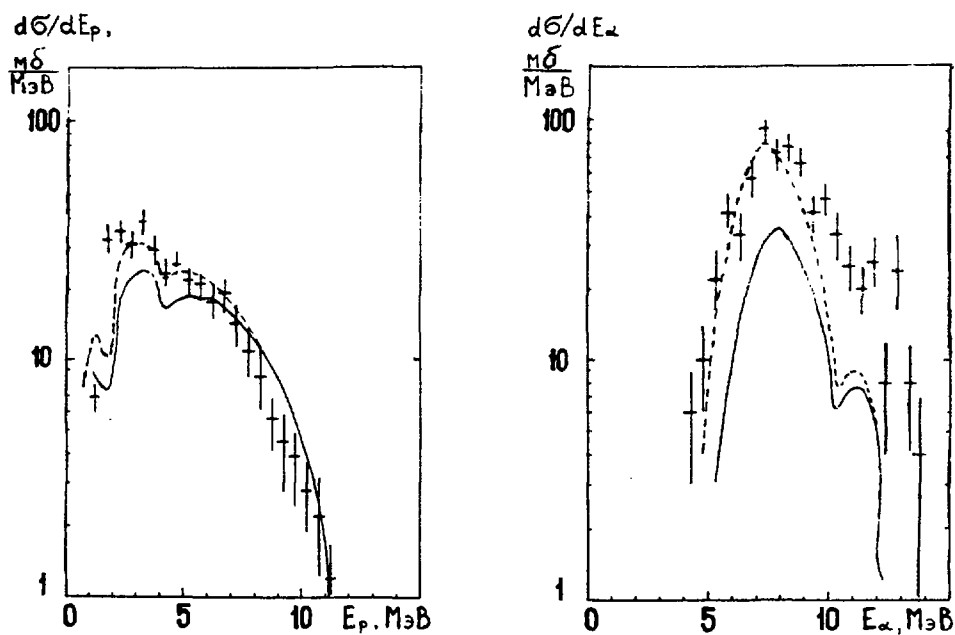


Fig.3. ^{52}Cr proton and α -particle emission spectra. Solid curves - calculation with initial transmission coefficients. Dashed curves - calculation with modified ones.

For alpha-particle emission spectra a systematical effect is observed: a displacement of the theoretical curve to the right about the experiment in the low alpha-particle energy range. This displacement can be eliminated with none of reasonable variations of level density parameters either in GSM or in the "Back-shift" Fermi-gas model.

Therefore, this effect can be rationalized as a need for modification of transmission coefficients in the alpha-channel, the modification involving an effective reduction of Coulomb barrier for alpha-particles.

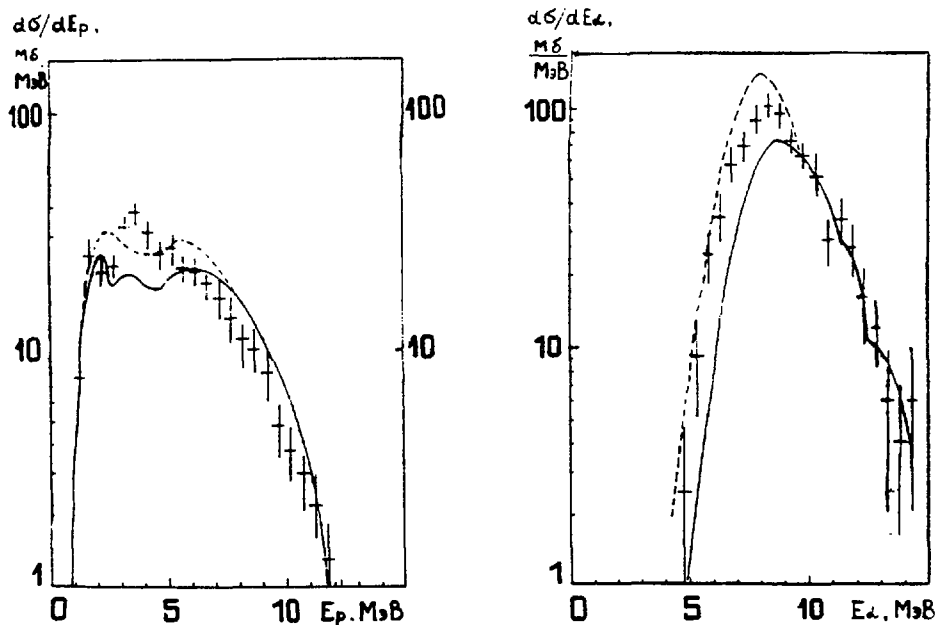


Fig.4. As in fig.3, but for Fe^{56} nucleus.

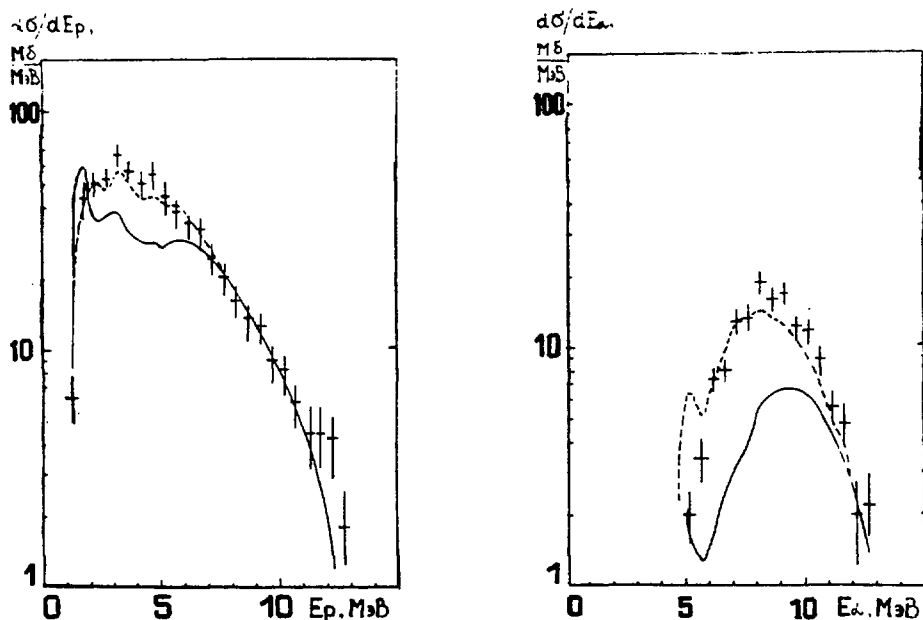


Fig.5. As in fig.3, but for Ni^{60} nucleus.

This correction for alpha-particle transmission coefficients was performed by way of increasing the real potential diffuseness parameter Q_R by 20-25%. A dashed line in fig.2 shows a cross-section of alpha-particles absorption by ^{59}Co nucleus obtained in this way. The calculations of alpha-particle emission spectra corresponding to these modified transmission coefficients are shown in fig 3-5 by dashed lines. The experimental data description in this case essentially improves. This very effect is de-

monstrated by the calculation of (n, α) excitation function on ^{54}Fe nucleus taken as an example (Fig.6).

As one can see in fig.2 the absorption cross-section modified is displaced by energy to the left about the experimental data. Apparently it points to an essential difference in the absorption cross-section for cold and excited nuclei. This effect can be followed well on the alpha-particle emission spectra (fig.3-5), due to the $(n, n\alpha)$ reaction contribution, which takes effect in the soft part of α -particle spectra, being negligible with the neutron energy under consideration. In the case of proton emission spectra the (n, np) reaction contribution is already significant,

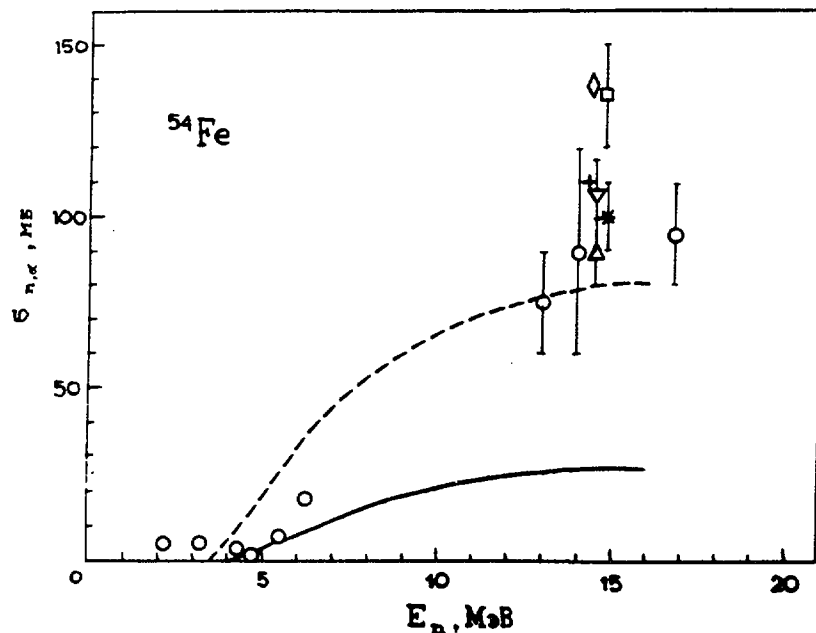


Fig.6. $^{54}\text{Fe} (n, \alpha) ^{51}\text{Cr}$ reaction excitation function.

that is why the analysis of a soft part of proton spectrum from the reaction (n, p) is more intricate. However, in fig.3-5 the effect of transmission coefficient differences for the excited and cold nuclei is also noticeable. The dashed line shows the calculations with the transmission coefficients obtained with the real potential Q_R diffuseness increase by 20 - 25 %.

It is noteworthy, that from the condition of spectrum shape description it follows, that the similar variation of transmission coefficients is required only at the proton and α -particle energies below the corresponding Coulomb barrier. The technique of the corresponding modification of transmission coefficients involves a smooth agreement of the increased and initial diffuseness of the real potential in the region of Coulomb barrier.

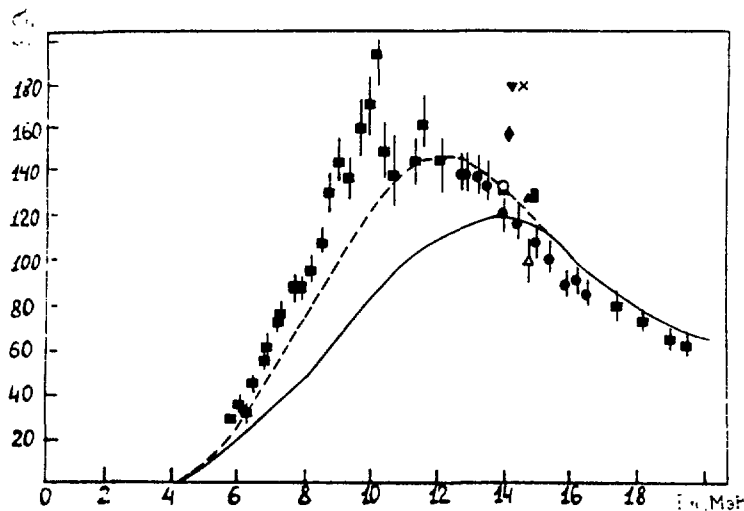


Fig.7. ^{60}Ni (n,p) ^{60}Co reaction excitation function.

Fig.7 demonstrates the effect of these variations of optical transmission coefficients for protons with the calculation of ^{60}Ni (np) reaction cross-sections taken as an example.

Hence, the question about a difference of charged particle absorption cross-sections for the excited and ground states of the atomic nucleus may well be posed with fair validity. This statement is useful for the solution of an old problem of nuclear level density analysis in various reactions. Thus, the level density parameters displaced about the values known from the neutron data can be obtained at the analysis of charged particles emission spectra. This problem is removed with transmission coefficient modification performed in this work.

The similar conclusion on the difference of the cross-section of α -particle and proton absorption by a nucleus in the ground and excited states was made in the work by Mc.Mahan and Alexander [18] at the analysis of these particle emission spectra in the reaction $^{12}\text{C} + ^{122}\text{W}$.

An indirect evidence for the validity of the suggested explanation of the observed differences in the calculated spectra of charged particles emission from the experimental data may be the Rumanian group's results [19] on the description of (n,p) reaction excitation functions on titanium isotopes. In Ref. [19] it was actually shown, that for the description of ^{45}Sc (p,n) ^{45}Ti and ^{46}Ti (n,p) ^{46}Sc reaction cross-sections the different parameters of optical potential are required, an imaginary part of the potential for the second case needing significant increase (i.e. proton absorption increase).

There seems to be sufficient data in favour of such an assertion. However, it should be noted, that the proton absorption cross-sections and particularly those for alpha-particles were poorly investigated experimentally. The optical model parameters for the particles with energies below the Coulomb barrier are also investigated poorly. That is why it seems to be premature to make conclusions about the absolute value of the effect and its theoretical interpretation. To solve this problem it is essential to analyze a wide range of nuclei and excitation energies and probably a wider class of reactions.

References

1. Ignatyuk A.V. Statistical properties of excited atomic nuclei. M.: Energoizdat, 1983.
2. Rao G.R., Colen B.L., Degan J.H., Chan K.C. Phys. Rev.C., 1973, v. 7, p.733.
3. Bychkov V.M., Plyaskin V.I. In book: Neutron Physics: (Proceedings of the 4th All-Union Conference on Neutron Physics, Kiev, 1977), M., 1977, v.2, p.84-88.
Bychkov V.M., Pashchenko A.B., Plyaskin V.I. Voprosy Atomnoi Nauki i Techniki, Ser. Yadernye Konstanty, M.:TsNIIATOMINFORM, 1983, v.3(52), p.3.
4. Bychkov V.M., Zelenetsky A.V., Pashchenko A.B. International Conference on Neutron Physics, Kiev, Septemder 1987.
5. Cline C.K., Blann M. Nucl.Phys., 1977, v.A172, p,225.
6. Dilg W., Schantl W., Vonach H., Uhl M. Nucl.Phys., 1973, v.A217, p,269.
7. Bychkov V.M., Grudzevich O.T., Plyaskin V.I. Voprosy Atomnoi Nauki i Techniki, Ser. Yadernye Konstanty, M.:TsNIIATOMINFORM, 1987, v.3, p.14.
8. Grudzevich O.T., Ignatyuk A.V., Plyaskin V.I. International Conference on Neutron Physics, Kiev, September 1987.
9. Wilmore D. and Hodgson P.E. Nucl.Phys., 1964, v.55, p.673.
10. Becchetti F.D., Jr., Greenleess G.W. Phys.Rev., 1969, v. 182, p. 1190.
11. Rapaport I., Kulkarni V. and Finlay R.W. Nucl.Phys., 1979, v.A330, p.15.
12. Bychkov V.M., Manokhin V.N., Pronyaev V.G., et al. Neutron Physics, v.I, M.: TsNIIATOMINFORM; 1976, p.160.
13. Perey F.G. Phys.Rev., 1963, v.131, p.745.
14. Mc.Fadden L. and Satchler G.R. Nucl.Phys., 1966, v.84. p.177.
15. Trombik W. et al. Phys.Rev., 1974, v.C9, p.5.

16. Huizenga I.R. and Igo G. Nucl.Phys., 1962, v.29, p.462.
17. Grimes S.M. et al. Phys.Rev., 1979, v.C19, p.2127.
18. Mc.Mahan M. and Alexander J. Phys.Rev., 1980, v.C21, p.1261.
19. Avrigeanu M., Avrigeanu V. and Ivascu M. Report NEANDC-222"U", Paris, 1986, p.279.

INVESTIGATION OF THE ANGULAR DISTRIBUTION OF SECONDARY
ENERGY DEPENDENT INELASTIC NEUTRON CROSS SECTIONS IN
STRUCTURAL MATERIALS USING BLANN'S GEOMETRY DEPENDENT
HYBRID MODEL

E. Bahm and H. Jahn
Kernforschungszentrum Karlsruhe
Institut für Neutronenphysik und Reaktortechnik
Karlsruhe, Federal Republic of Germany

Abstract

The measured results for the 14,6 MeV inelastic neutron cross-sections show considerable experimental errors in particular in forward direction. Also remarkable discrepancies between these measured results of the different experimental groups are to be observed. Consequently it is not possible to draw definitive conclusions concerning the validity of the various concepts of nuclear reaction mechanisms from these inaccurate measured results. In this paper we show that the situation is considerably improved if we add information from the results of measurements of the inelastic proton scattering cross-sections. With this additional information we obtain a sufficient starting point to calculate rather accurate and unique results for the double differential cross-sections of inelastic neutron scattering at the high energy tail of the secondary energy. This is demonstrated by a few examples of ^{56}Fe . Moreover by applying certain averages to the angle integrated inelastic cross-sections the results of the geometry dependent hybrid model are obtained. Consequently this might be a hint to a more rigorous derivation of this model.

Discrepancies and errors of the measured fast (n,n')-cross sections

The investigations of this paper start from the fact that the measured results of the different experimental groups for the 14.6 MEV neutron cross sections show not only considerable experimental errors in particular in forward direction but also remarkable discrepancies between them must be noted. This is demonstrated rather clearly by figures 1a and b showing

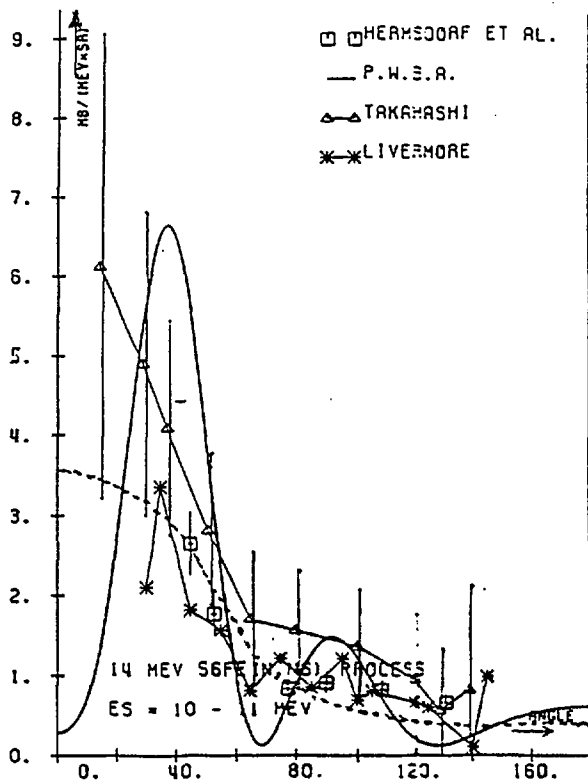
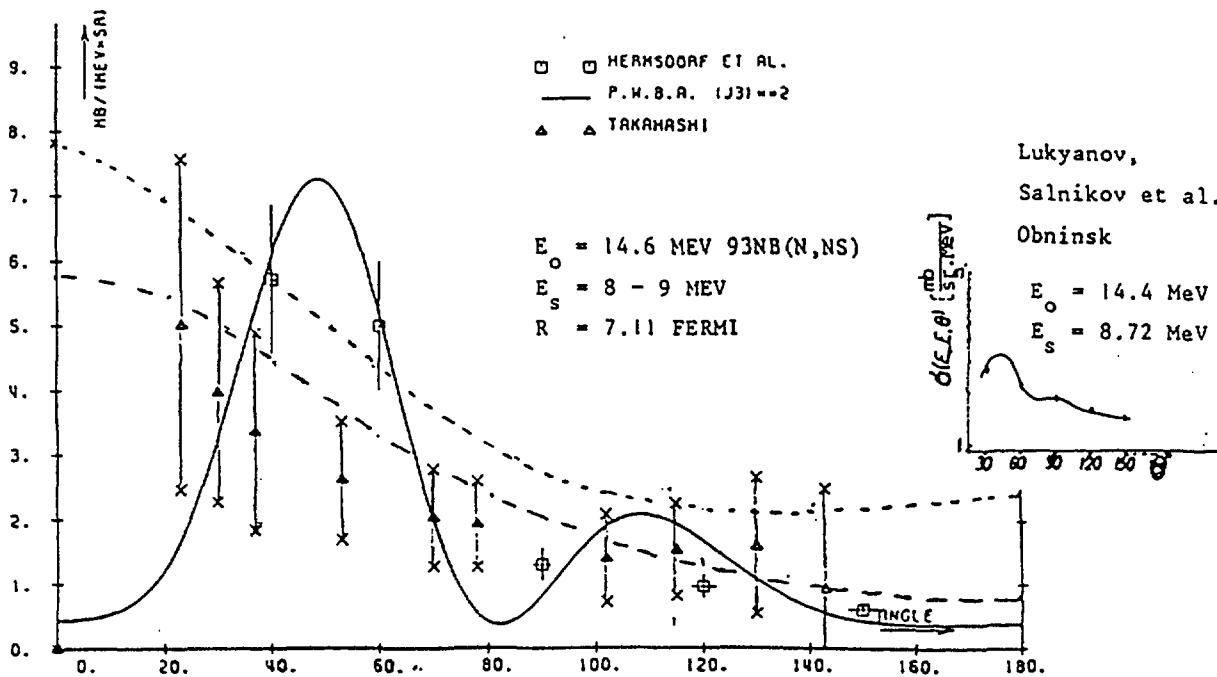


Fig. 1a:
Angular distribution of inelastically scattered neutrons for ^{56}Fe .



Intercomparison by E. Bahm and H. Jahn.

Fig. 1b: Angular distribution of inelastically scattered neutrons for ^{93}Nb .

Fig. 1a and Fig. 1b give a demonstration of consistency of different concepts of angular distributions of inelastically scattered 14,6 MeV neutrons with the respective measured cross section results because of their genuine inaccuracy.

Points with error bars: Average of the measured results from the Dresden /7/ and Osaka /8/ groups. ...
 Straight line: SECDIST results (KfK), /5/, /6/.
 Dotted line: PRANG results (ECN) at 8 MeV secondary energy /1/.
 Dashed line: GNASH results (LAS) at 8 MeV secondary energy /9/.

INELASTIC SCATTERING OF 17.5 MEV PROTONS

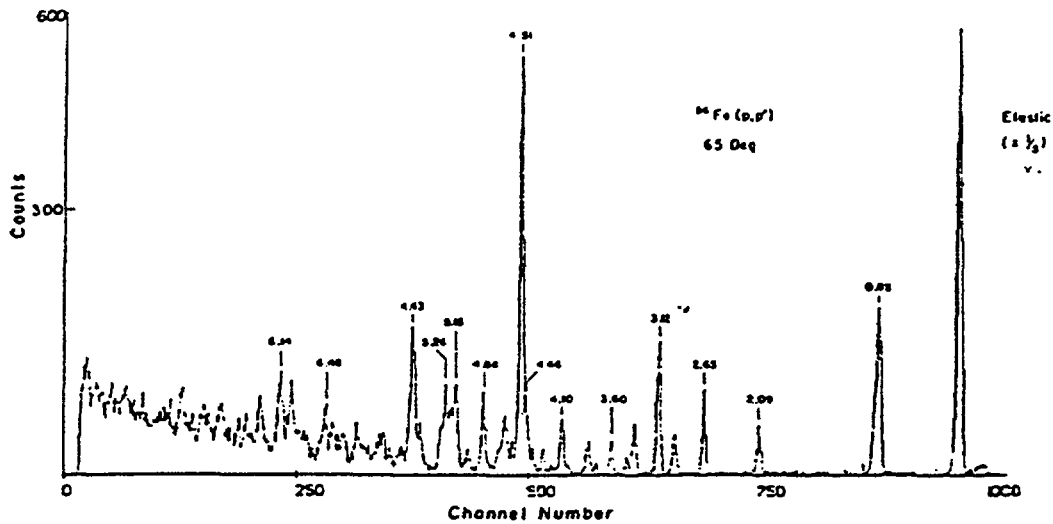


Fig. 1c: A representative measured spectrum of the protons scattered inelastically from a ^{56}Fe target at a scattering angle of 65 Deg. taken from the work of Peterson /10/.

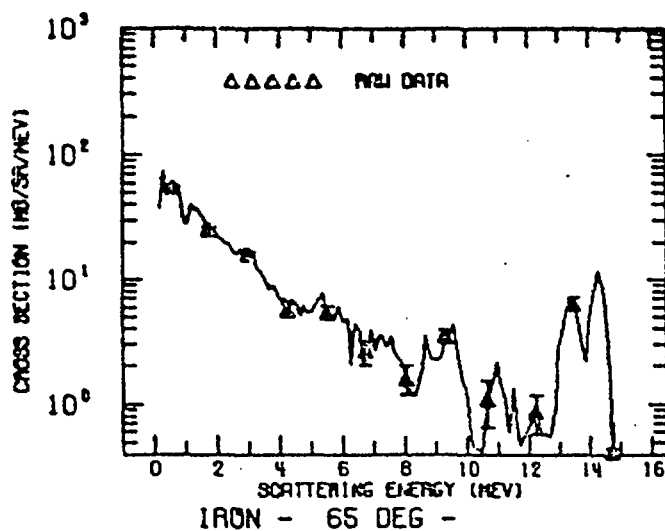


Fig. 1d: A representative measured spectrum of the 14,6 MeV neutrons scattered inelastically from a ^{56}Fe target at a scattering angle of 65 Deg. taken from the thesis of Kammerdiener /11/.

(cont. page 114)

In Fig. 1c and Fig. 1d an intercomparison is given between the measured highly energy resolved 17,5 MeV proton cross sections and the measured 14,6 MeV neutron cross sections with its genuine low energy resolution for inelastic scattering from a ^{56}Fe target at a scattering angle of 65 Deg.

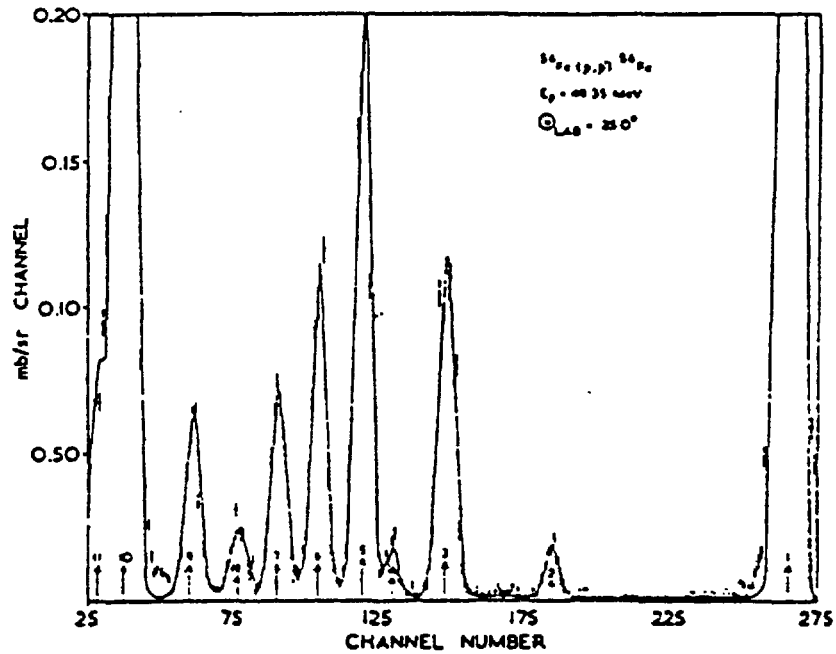
measured and calculated angular distributions of 14.6 MEV (n,n')-cross sections of ^{93}Nb and ^{56}Fe where the dotted, dashed and straight lines in Figures 1a and b represent different concepts for the models of the related nuclear reaction mechanism.

Decision between the different reaction models not possible on the basis of these inaccurate measured fast (n,n')-cross sections.

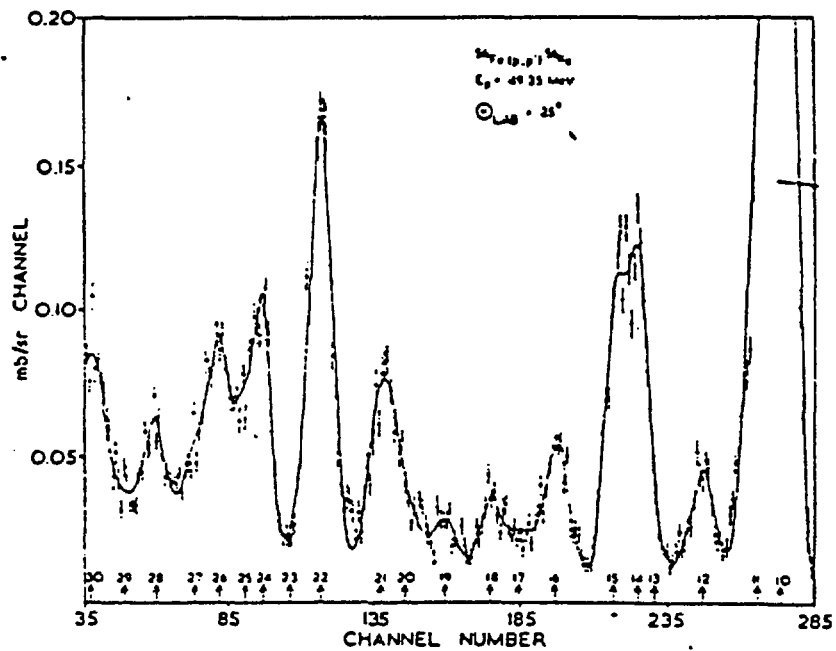
In the Figures 1a and b the dotted lines result from the approach of Costa, Gruppelaar and Akkermans /1/ which is constructed by using the model of Mantzouranis, Weidenmüller und Agassi /2/, the dashed line is obtained from the GNASH code of Young and Arthur /3/ based on the so called Kalbach-Mann systematics /4/ and the straight lines represent the results from a combination of Blann's geometry-dependent hybrid model with a simplified description of the direct reaction mechanism /5/, /6/. It now can be seen very clearly from the Figures 1a and b that the measured results are not accurate enough to enable a decision concerning the validity of the different concepts. Such a decision never can be met on the basis of these measured fast neutron cross-sections because at the energies of the considered order of magnitude the energy resolution of the neutron energy measurements cannot be much less than ca. 1 MeV.

Resort to charged particle results

One way out of this situation can be to resort to the results of measured fast charged particle cross-sections as for instance the cross-section of inelastic scattering of fast protons. Fig. 1c shows the very high resolution obtainable in the proton-channel



A typical time spectrum from the spark chamber for levels to 4.7 MeV excitation. The solid line is the fit to the spectra using the NSPEC programme.



A typical time spectrum from the spark chamber for levels from 4.5 MeV to 8.0 MeV. The solid line is the fit to the spectra using the NSPEC programme.

Fig. 2: Measured spectrum of inelastically scattered 49,35 MeV protons at a scattering angle of 25 Deg. taken from the work of Mani /12/.

presented by the measured results of the inelastic 17,5 MeV proton-cross-section at a scattering angle of 65° from the work of Peterson /10/. This might be compared to the much lower energy resolution of the measured results of the inelastic 14,6 MeV neutron-cross-section at a scattering angle of 65° taken from

⁵⁶Fe STATES

TABLE 1

Energy levels (MeV) and spin values obtained in Ref. /12/ and Ref. /10/

Peak no v	Ref. /12/				Ref. /10/			
	ϵ_v	β_v	β^2_v	l_v	ϵ_v	β_v	β^2_v	l_v
1	0.849	0.2	0.040	2 ⁺	0.85	0.29	0.0841	2 ⁺
2	2.118			(4 ⁺)	2.08			
3	2.695	0.06	0.036	2 ⁺	2.65	0.107	0.0115	2 ⁺
	2.968			(0 ⁺)	2.94			
4	2.968	0.02	0.0004	(2 ⁺)	2.96	0.044	0.0019	2 ⁺
5	3.159	0.087	0.0077	4 ⁺	3.12	0.124	0.0154	4 ⁺
6	3.411	0.06	0.0036	2 ⁺	3.37	0.043	0.0011	2 ⁺
	3.411			(6 ⁺)	3.39	0.03	0.0009	6 ⁺
7	3.635	0.05	0.0025	2 ⁺	3.60	0.053	0.0028	2 ⁺
7a					3.75	0.082	0.0067	2 ⁺
8	3.850	0.03	0.0009	2 ⁺	3.83	0.069	0.0048	2 ⁺
					4.04			
9	4.124	0.045	0.0020	4 ⁺	4.10	0.095	0.0090	4 ⁺
					4.40	0.053	0.0028	(4 ⁺)
					4.46	0.074	0.0055	4 ⁺
10	4.512	0.154	0.0237	3 ⁻	4.51	0.198	0.0392	3 ⁻
11	4.660	0.071	0.0050	4 ⁺	4.61	0.055	0.0030	4 ⁺
11a					4.69	0.064	0.0041	4 ⁺
11b					4.73	0.050	0.0025	2 ⁺
12	4.860	0.039	0.0015	4 ⁺	4.88	0.100	0.0100	4 ⁺
13	5.106	0.041	0.0017	5 ⁻	5.15	0.097	0.0094	(4 ⁺)
14	5.195	0.046	0.0022	(4 ⁻)	5.20	0.078	0.0061	(3 ⁻)
15	5.266	0.050	0.0025	4 ⁺	5.26			
16	5.535	0.050	0.0025	2 ⁺	5.51			
					5.58			
					5.69			
17	5.763	0.03	0.0009	(5 ⁺)	5.73			
18	5.880	0.039	0.0015	4 ⁺	5.90			
19	6.067	0.037	0.0014	4 ⁺	6.00			
20	6.273	0.053	0.0028	4 ⁺	6.30			
21	6.410			(3,4)				
					6.48			2(+)
22	6.635	0.084	0.0071	(3,4)				
23	6.870							
24	6.966	0.05	0.0025	3				
25	7.080	0.046	0.0021	(3,4)				
26	7.189	0.046	0.0021	(3,4)				
27	7.312	0.038	0.0014	(3,4)				
28	7.475	0.051	0.0026	(3 ⁻)				

the thesis of Kammerdiener /11/ and shown in Fig. 1d on which the ENDF/BIV data are based. Fig. 2 shows the very high energy resolution of the 49,35 MeV (p,p')-cross-section for a scattering angle of 25°. The peaks correspond to the energy levels of the 26 lowest excited states of ⁵⁶Fe. As results of a DWBA-analysis of Mani /12/ the excitation energies and spins of these states are listed in Tab. 1 and in addition in Tab. 1 for the same quantities the results of the DWBA-analysis of Peterson /10/ of 17,5 MeV (p,p')-cross-sections are shown. Fig. 3 shows examples of Peterson DWBA-angular distributions belonging to the excitations of the 4 lowest 2⁺-states of ⁵⁶Fe.

The straight lines through the experimental points in Fig. 3 are obtained from the DWBA-calculation according to the formulae

$$(1) \quad \frac{d\sigma_{i,f}^{(x)}(\epsilon_i, \epsilon_{f_v}, \theta)}{d\Omega_{f_v}} = \beta_v^2 \sigma_v^{(x)}(\epsilon_i, \epsilon_{f_v}, \theta)$$

with

$$(1a) \quad \sigma_v^{(x)}(\epsilon_i, \epsilon_{f_v}, \theta) = \frac{k_{f_v}}{k_i} \left(\frac{m}{2\pi\hbar^2} \right) \frac{R_0^2}{2l_v+1}$$

$$\left| \int X^{-(x)}(\underline{k}_{f_v}, \underline{r}) \left(\frac{\partial U(\underline{r})}{\partial r} \right) Y_{l_v}(\vartheta) X^{+(x)}(\underline{k}_i, \underline{r}) d^3r \right|^2$$

and

$$(1b) \quad R_0 = r_0 A^{1/3}; \quad r_0 = 1.25 \cdot 10^{-13} \text{ fm}; \quad U_{(\underline{r})}^{(x)} = \text{optical potential}$$

θ = scattering angle

Ω = space angle of scattering

ϑ = projectile coordinate angle

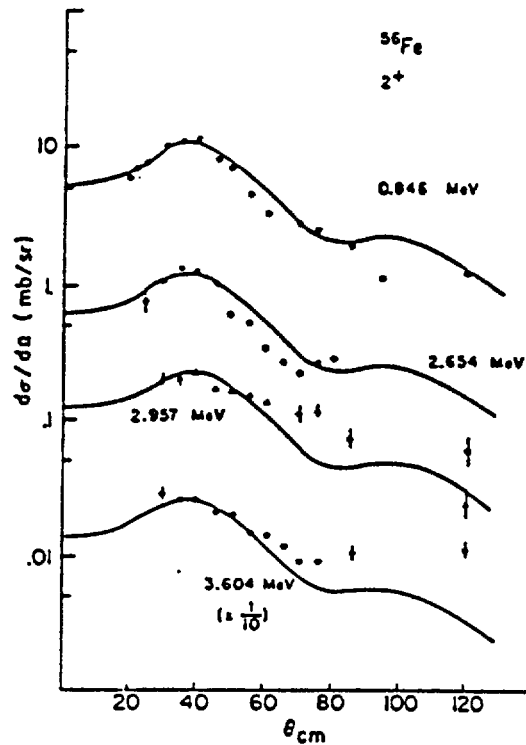
k_i, k_{f_v} = initial and final projectile wave vectors belonging to the incident and final energies ϵ and ϵ_v with the target excitation energy ϵ_v

$X_{\pm}^{(x)}$ = optical model scattering states of projectile (x) indicating proton (p) or neutron (n)

$Y_{l_v}(\vartheta)$ = spherical harmonics

m = nucleon mass

l_v = transferred angular momentum belonging to level v



The data for populating four known 2^+ states of ^{56}Fe are compared to the DWBA predictions.

Fig. 3: Selected angular distributed differential inelastically 17,5 MeV proton cross-section of Peterson /10/ corresponding to the spectrum of Fig. 1c.

(1)-(1b) represent the DWBA-formulae based on the collective vibrational model. But beyond of this (1)-(1b) have been used by Peterson /10/, Mani /12/ and Ignatyuk /13/ also for the phenomenological analysis of any excitation by direct inelastic proton scattering. Then β_v is a parameter to be chosen to fit the experimental angular distribution. As above the index (x) denotes the type of nucleon (eg. proton or neutron). No index (x) is attached to β_v because the dependence of β_v on the type of nucleon can be neglected. But β_v depends on the target nucleus. Thus β_v can be obtained by fitting the experimental data for one type of nucleon and can then be used to calculate the angular distribution for the other type of nucleon, for the same target nucleus. For instance in the proton-channel experimental data also could be obtained for the small angle region from 52° down to less than 20° (see Peterson /10/, Mani /12/ where no sufficiently accurate experimental data are available for the neutron channel, for which the influence of the incident beam can neither be suppressed nor estimated sufficiently accurate (see experimental points of Fig. 1a/b and Fig.3). Thus once we have obtained β_v experimentally from the proton-channel we are able to calculate the scattering for the neutron-channel, in particular for small angles.

This is important since the neutron channel is much less qualified for the determination of the β_v than the proton channel because of the much lower energy resolution of the fast-neutron cross section measurements as compared to the proton cross section measurements in the same energy region. This is demonstrated by the comparison presented in Fig. 1c/d.

3. Neutron Cross Section Calculations

To obtain the appropriate angular distributions of the inelastic neutron cross sections we insert the β_v -values from the proton channel analysis of Peterson /10/ and Mani /12/ shown in Tab. 1 into the expressions of the equations (1)-(1b) together with the scattering states $x^{\pm(n)}$, calculated from the optical model of the neutron channel instead of the scattering states $x^{\pm(p)}$ from the optical model of the proton channel analysis of Peterson and Mani /10/, /12/. Calculations of this type for the neutron channel have been carried out by Kinney and Perey /14/, by Penny and Kinney /15/ and by Fu /16/. Scattering angle dependent neutron cross sections corresponding to the proton cross sections of Fig. 3 have been obtained by these authors and can be found on the ENDFB/IV files of the US neutron cross section library.

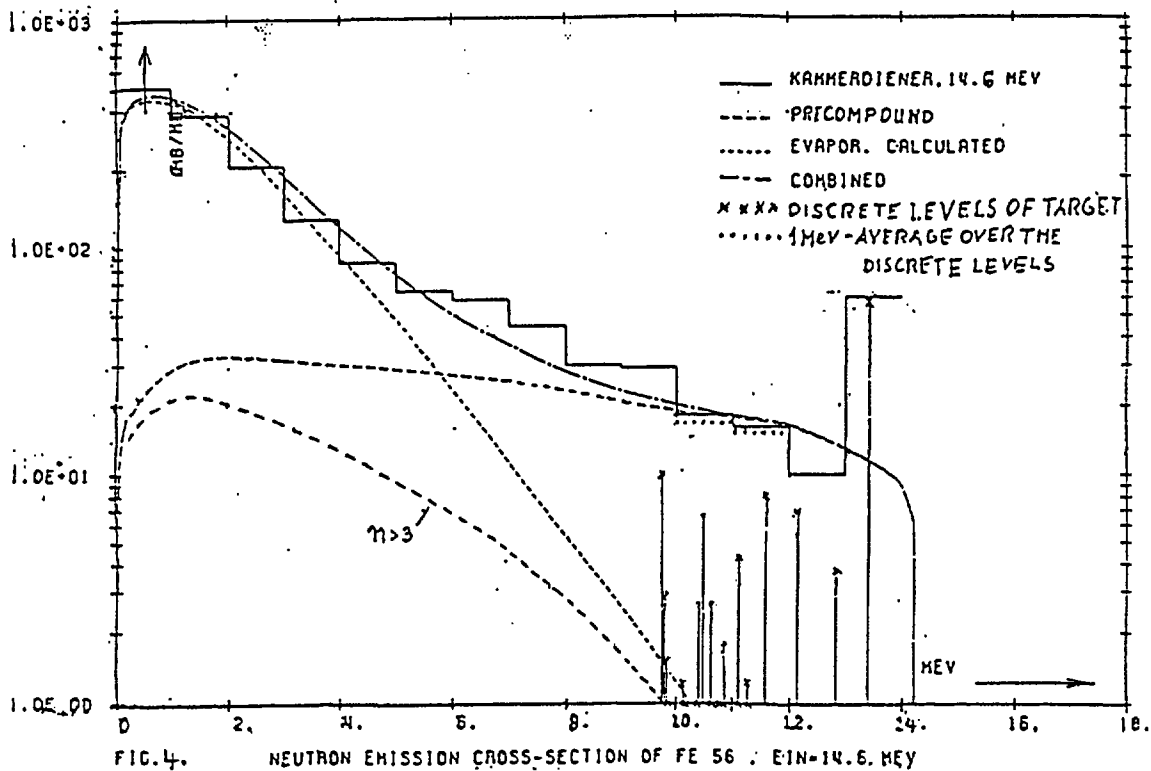
The angle-dependent inelastic neutron cross sections thus obtained belong to the discrete excited states with the sharp energies ϵ_v listed in Tab. 1. To obtain measurable angle- and energy-dependent inelastic neutron cross sections the finite widths of the measured energy distributions in the neutron channel have to be considered. These widths are much wider than those in the proton channel shown in the Figures 1c and 2 as mentioned above. Fig. 1c and Fig. 2 show that in the proton channel the level widths are small enough compared to the distances of the neighbouring levels for about the first 20 levels to enable the investigations for the single levels leading to the results of Tab. 1. In contrast to this behaviour in the proton channel it is shown by Fig. 1d, that the widths of the measured secondary energy distribution of the inelastic fast-neutron cross sections are comparable or even wider than the distances of the neighbouring energy levels. Consequently, the measured secondary energy- and angular distributions of the fast-neutron inelastic scattering cross sections are much influenced by the short-comings of the experimental set up for that neutron cross section measurements in particular at the high-energy tail. Therefore it is interesting to look whether certain averages of the secondary

energy-dependent inelastic fast-neutron scattering cross sections can be found which have a direct physical meaning in particular at the high-energy tail and which can directly be obtained by measurement.

4. Comparison of DWBA- and GDH Average Cross Section Results

As a first step to answer this question Fig. 4 may be considered. Fig. 4 shows experimental and theoretical results for the angle-integrated 14,6 MeV inelastic neutron cross section. The step curve of Fig. 4 with 1 MeV interval of the steps is obtained by Hansen et al. /17/ from measurements of the neutron leakage spectrum from an assembly of iron. This experimental step curve is in particular at the high-energy tail quite well reproduced by the smooth straight line which is obtained from calculated results /6/ of Blann's geometry-dependent hybrid model with optical model option. This approach has no fit-parameters other than those of the usual optical model. This is a remarkable improvement compared to the exciton master equation approach where the internal transition rate between the excitation steps has to be adjusted as an extra fit parameter if the high-energy tail of the secondary energy-dependent inelastic nucleon cross section should be taken into account /6/.

On the other hand it can be shown that the experimental step curve of Fig. 4 can quite well be reproduced by average results



of the neutron-channel-DWBA-calculations outlined above with ρ_v taken from the proton-channel as shown in Tab.1. inserted into the equations (1) - (1b) used to calculate the inelastic neutron cross section. By angle-integrating the results obtained from the equations (1) - (1b) by these equations according to

$$(2) \quad \int d\Omega_{f_v} \left(\frac{d\sigma_{if_v}^{(n)}(\epsilon_i, \epsilon_{f_v}, \theta)}{d\Omega_{f_v}} \right)_{DWBA} = \left(\sigma_{if_v}^{(n)}(\epsilon_i, \epsilon_{f_v}) \right)_{DWBA}$$

we obtain on the right hand side of equation (2) cross section results for the single levels which are shown in Fig. 4. by the discrete endpoints of the vertical lines for the first 13 levels.

We now turn to reproduce the experimental step curve of Fig. 4. by averaging the measurable angle-integrated secondary energy-dependent inelastic neutron cross section over intervals I being equal to the widths of the steps. Then we obtain

$$(3) \quad \overline{\left(\sigma_i^{(n)}(\epsilon_i, \epsilon) \right)} = \frac{1}{I} \int_{\epsilon-I/2}^{\epsilon+I/2} \left(\frac{d\sigma_i^{(n)}(\epsilon_i, \epsilon')}{d\epsilon'} \right)_{DWBA} d\epsilon' =$$

$$= \frac{1}{I} \int_{\epsilon-I/2}^{\epsilon+I/2} \sum_v \rho_v(\epsilon', \epsilon_{f_v}) \sigma_{if_v}^{(n)}(\epsilon_i, \epsilon')_{DWBA} d\epsilon' = \frac{1}{I} \sum_{v \in I} \left(\sigma_{if_v}^{(n)}(\epsilon_i, \epsilon_{f_v}) \right)_{DWBA}$$

where the $\rho_v(\epsilon', \epsilon_{f_v})$ are the normalized energy distributions around the excitation energies of the single levels and where the single terms in the sum at the most right hand side of eq.(3) and in the integrand of the expression before it are given by the right hand side of eq. (2). Equation (3) expresses that the average angle-integrated inelastic fast-neutron cross section is at the high-energy tail of the secondary energy equal to the sum of the discrete cross section values of Fig. 4 within each averaging interval I.

The results of this summing up for the two intervals 10-11 MeV and 11-12 MeV are represented in Fig. 4 as horizontal dotted lines which are seen to coincide quite well with the experimental step curve as well as with the $n_0=3$ contribution of the geometry dependent hybrid model. Since the latter is the only calculated contribution of this model to the angle integrated secondary energy dependent neutron cross section at this high energy tail of secondary

energy it can be presumed that the $n_0=3$ component of the geometry dependent hybrid model represents a certain average over the direct component of the inelastic nucleon cross section. With the definitions and the results of equations (2) and (3) we therefore conclude

$$(4) \quad \frac{1}{I} \int_{\epsilon_{f_v} = \epsilon_j - I/2}^{\epsilon_j + I/2} \left(\frac{d\sigma_{if_v}^{(n)}(\epsilon_i, \epsilon_{f_v})}{d\epsilon'} \right)_{DWBA} = \frac{1}{I} \int_{\epsilon_j - I/2}^{\epsilon_j + I/2} \left(\frac{d\sigma_{if_v}^{(n)}(\epsilon_i, \epsilon')}{d\epsilon'} \right)_{n=n_0=3}^{GDH} d\epsilon'$$

The averaging intervals I in equations (3) and (4) do not include very many levels. For instance the interval 10-11 MeV includes 6 levels and the interval 11-12 MeV includes 5 levels according to Tab.1. Such a small number of levels is obviously already enough to obtain for the inelastic nucleon cross section at the high-energy tail of the secondary energy an average with a physical meaning in the sense that it can be calculated by a physical model like in this case by Blann's geometry dependent hybrid model. Because of the small number of included levels we conclude that it may not be a statistical average we have to do with in this case. Instead we may have to do here with a summing up in the sense of the well known sum rules of Satchler /15/ and Lane /20/ (see also Lewis /21/).

If we consider the derivation from equations (1) to (4) then we arrive at the conclusion that it should make sense to introduce the averaged measured angle-dependent differential inelastic fast-neutron cross section at the high-secondary energy tail according to

$$(5) \quad \left(\frac{d^2\sigma_{ij}^{(n)}(\epsilon_i, \epsilon_j, \theta_j)}{d\epsilon_j d\Omega_j} \right)_{dir} = \frac{1}{I} \int_{\epsilon_j - I/2}^{\epsilon_j + I/2} \left(\frac{d^2\sigma_{ij}^{(n)}(\epsilon_i, \epsilon', \theta_j)}{d\epsilon' d\Omega_j} \right)_{dir} d\epsilon'$$

Corresponding to equation (3) we then obtain

$$(6) \quad \left(\frac{d^2\sigma_{ij}^{(n)}(\epsilon_i, \epsilon_j, \theta_j)}{d\epsilon_j d\Omega_j} \right)_{dir} = \frac{1}{I} \int_{\epsilon_j - I/2}^{\epsilon_j + I/2} \sum_{\nu} p_{\nu}(\epsilon', \epsilon_{f_{\nu}}) \left(\frac{d\sigma_{if_{\nu}}^{(n)}(\epsilon_i, \epsilon', \theta_{f_{\nu}})}{d\Omega_{f_{\nu}}} \right)_{DWBA} d\epsilon' =$$

$$= \frac{1}{I} \int_{\epsilon_{f_{\nu}} = \epsilon_j - I/2}^{\epsilon_j + I/2} \left(\frac{d\sigma_{if_{\nu}}^{(n)}(\epsilon_i, \epsilon_{f_{\nu}}, \theta_{f_{\nu}})}{d\Omega_{f_{\nu}}} \right)_{DWBA} d\epsilon_{f_{\nu}}$$

If now the validity of equation (4) with eq. (2) is taken into account then it can be concluded that at the high secondary energy tail the following relation holds

$$(7) \quad \int \left(\frac{d^2 \sigma_{ij}^{(n)}(\epsilon_i, \epsilon_j, \theta_j)}{d\epsilon_j d\Omega_j} \right)_{\text{dir}} d\Omega_j = \frac{1}{j} \int_j^{\epsilon_i + 1/2} \left(\frac{d\sigma_j^{(n)}(\epsilon_i, \epsilon')}{d\epsilon'} \right)_{n=n_0=3}^{\text{GDH}} d\epsilon'$$

By equation (7) it is expressed that the result of angle integration of the averaged measured angle-dependent differential inelastic fast-neutron cross section at the high secondary energy tail comes out as the corresponding average over the $n=n_0=3$ - component of the GDH contribution.

By a look at Tab. 1 it is suggested that there may be intervals including enough successive levels with the same l to fulfill equations (4) or (7) for this respective l . In particular it is shown by Tab. 1 that at the low end of the target spectrum most levels have $l = 2$.

From Fig. 3 it can be seen that any level shows a DWBA angular distribution of the inelastically scattered protons in the considered region of secondary energy. According to the explanations given above the same should be true for the inelastically scattered neutrons with equation (7) being valid for the neutrons as well as for the protons. Thus if we use as a first approach the approximate DWBA of McCarthy and Pursey /21/ according to (8) then (8) has to

$$(8) \quad \left(\frac{d^2 \sigma_{ij}(\epsilon_i, \epsilon_j, \theta_j)}{d\epsilon_j d\Omega_j} \right)_{\text{dir}} = F(\epsilon_i, \epsilon_j) \sqrt{\frac{\epsilon_j}{\epsilon_i}} \times j_1^2 \text{ (QR)}$$

$$Q = |\vec{p}_i - \vec{p}_j + i\frac{\gamma}{R} \left(\frac{\vec{p}_i}{p_i} - \frac{\vec{p}_j}{p_j} \right)|; \quad R = 1,07 \text{ fm } A^{1/3} + 2,4 \text{ fm}$$

(Radius-law of GDH)

fulfill (7) and the at first unknown factor $F(\epsilon_i, \epsilon_i')$ in (8) can be determined this way. Fig. 5 shows angular distributions of inelastically scattered neutrons calculated this way from equation (8) for the intervals 10,6-11,1 MeV and 11,6-13,6 MeV of the secondary energy of inelastically scattered 14,6 MeV neutrons. In the interval 10,6-11,1 MeV only $l = 2$ levels are contained according to Tab. 1 while in the interval 11,6-13,6 MeV the levels with $l = 2$ are predominant. We therefore took the choice $l = 2$ for the calculations according equation (8) with $\gamma = 1,1$ leading to the results of Fig. 5 which agree quite well with the averaged measured points of the Dresden

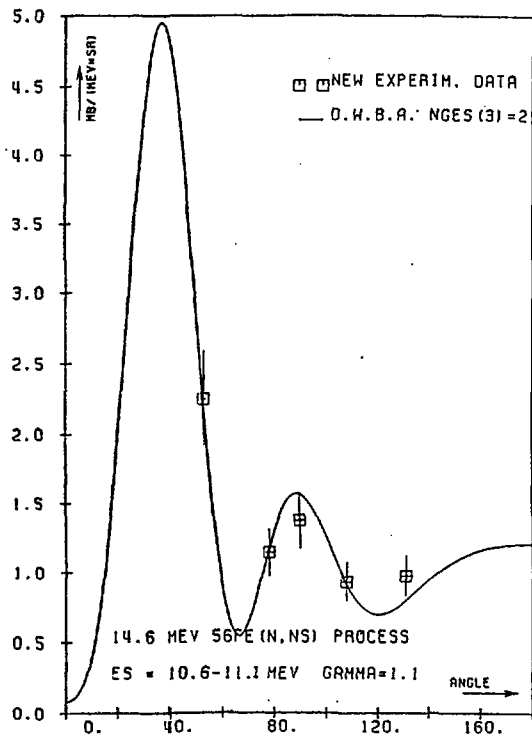


FIG. 5A ANGULAR DISTRIBUTION OF INELASTICALLY SCATTERED NEUTRONS.

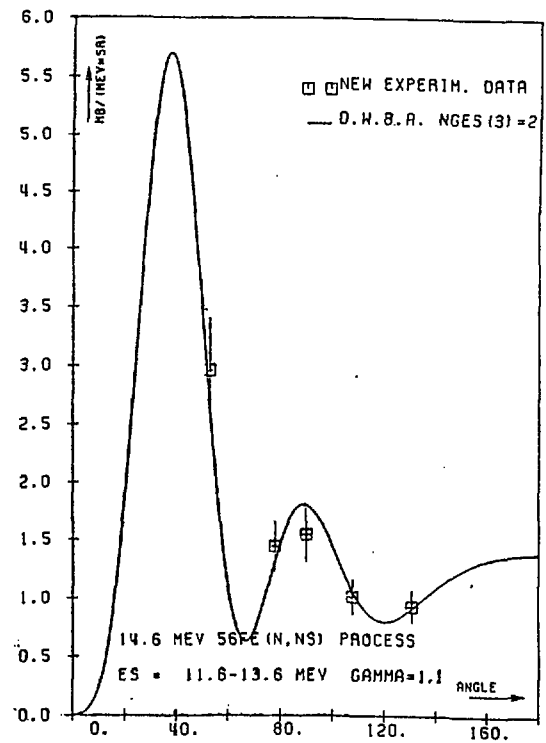


FIG. 5B ANGULAR DISTRIBUTION OF INELASTICALLY SCATTERED NEUTRONS.

group. The value $\gamma = 1,1$ is also in reasonable agreement with the value which can be derived from the approach of McCarthy and Pursey /21/ for the usual optical model. But this approach is less reliable for the small angle region. Work is going on to improve it in this respect.

References

- /1/ Gruppelaar, H. and Akkermann, I.M., ECN-84, June 1980.
- /2/ Mantzouranis, G., Weidenmüller, H.A., Agassi, B., Z. Physik A276, 145 (1976).
- /3/ Young, P.G. and Arthur, E.D.: GNASH: A Preequilibrium Statistical Nuclear Model Code for Calculations of Cross-Sections and Emission Spectra, Los Alamos report, LA-6947 (1977), about the many applications, Knoxville Conference 1979, Antwerp Conference 1982, Phys. Rev. C16 (1977), 1792.
- /4/ Kalbach, C. PRECO-D2: Program for calculating pre-equilibrium and direct reaction double differential cross sections, Los Alamos National Laboratory Report LA-10248-MS.
- /5/ Broeders, I., Fischer, U., Jahn, H., Wiegner, E., Contribution to the "International Nuclear Model and Code Comparison on Pre-Equilibrium Effects", organized by the NEA DATA BANK 1983/84, Gif-sur-Yvette, France, NEANDC-204 "U", INDC(NEA)6, NEWS LETTER No. 32.

- /6/ Jahn, H., Critical Review of precompound models with consideration of the contribution to the "International Nuclear Model and Code Comparison on Pre-equilibrium Effects", organised by the NEA Data Bank 1983/84, KfK-3646, August 1984.
- /7/ Hermsdorf, D., Meister, A., Sassonov, S., Seeliger, D., Seidel, V. and Shahin, F., Kernenergie 17, 259 (1974) ZfK-277 U.
- /8/ Takahashi, A. et al., Double differential neutron emission cross sections, Numerical tables and figures (1983), A-83-01, Oktavian report. Osaka University, Japan.
- /9/ Sal'nikov, O.A., Inelastic scattering of neutrons, translated by IAEA, INDC(CCP)-233/L, June 1984.
- /10/ Peterson, R.J., An. of Phys. 53, 40 (1969).
- /11/ Kammerdiener, J.L. Report UCRL-51232 (1972).
- /12/ Mani, G.S., Nucl. Phys. A165, 225 (1971).
- /13/ Blokhin, A.I., Ignatyuk, A.V., Lunev, V.P., Pronyaev, V.G., in Materials of the Fourth Kiev Conf. on Neutron Physics, Part II, p. 131, 1977
 Blokhin, A.I., Pronyaev, V.G., Yad. Fiz. 30, 1258-1269 (November 1976)
 Sov. J. Nucl. Phys. 30 (5), Nov. 1979, Izv. A. N. SSR seriya fiz. 39, 2144 (1975).
- /14/ Kinney, W.E., and Perey, F.G., ORNL-4515 (1970).
- /15/ Penny, S.K. and Kinney, W.E., ORNL-4617 (1971), (ENDF-139).
- /16/ Fu, C.Y., Proceedings of the Conference on Nuclear Cross Sections and Technology, Washington, D.C., March 3-7, 1975, 328.
- /17/ Hansen, I.F., Anderson, I.D., Brown, P.S., Howerton, R.I., Kammerdiener, I.L., Logan, C.M., Plechaty, E.F. and Wong, C., Nucl. Sci. Eng. 51, 278 (1973).
- /18/ Satchler, G.R., Nucl. Phys. 55, 1, (1964).
- /19/ Lane, A.M., "Nuclear Theory", W.A. Benjamin Inc. 1964, New York-Amsterdam.
- /20/ Lewis, M.B., Phys. Rev. C9 (1974), 1978.
- /21/ McCarthy, I.E. and Pursey, D.L., "Introduction to Nuclear Theory", John Wiley & Sons, Inc. 1968, New York-Amsterdam.